Simulation of auto-pulses in channel flows between active elastic walls

A Thesis submitted by

Fatima Zain Alabdeen Ahmed AHMED

For the award of

Doctor of Philosophy

2019

Abstract

The present research is concerned with the model of self-propagating fluid pulses (auto-pulses) through the channel simulating an artificial artery. The key mechanism behind the model is the active motion of the walls similarly to the earlier model of Roberts (1994). While he considered the case of wide channels, where inertia prevails over viscosity, we considered the case of narrow channels, where viscosity prevails over inertia. The model is autonomous, nonlinear and has the form of the partial differential equation describing the displacement of the wall in time and along the channel (Strunin, 2009*a*).

In this thesis, the One-dimensional Integrated Radial Basis Function Network (1D-IRBFN) method is used for solving the equation. The method was previously tested by other authors on a variety of problems such as viscous and viscoelastic flows, structural analysis and turbulent flows in open channels. It was demonstrated that the 1D-IRBFN method has advantages over other numerical methods, for example finite difference and finite element methods, in terms of accuracy, faster approach and efficiency (Mai-Duy and Tran-Cong, 2001*a*).

In this thesis the following main results are obtained. We demonstrated that different initial conditions always lead to the settling of pulse trains where an individual pulse has certain speed and amplitude controlled by the governing equation. A variety of pulse solutions is obtained using homogeneous and periodic boundary conditions. The dynamics of one, two and three pulses per period are explored.

The fluid mass flux due to the pulses is calculated using theoretical and numer-

ical analysis. Based on the numerical results, we evaluated magnitudes of the phenomenological coefficients of the model equation responsible for the active motion of the walls.

Further, we presented numerical solutions for the channel branching into two thinner channels to simulate branching of the artificial artery. Using homogeneous boundary conditions on the edges of space domain and continuity conditions at the branching point, we obtained and analysed the pulses penetrating from the thick channel into the thin channels.

We also derived and analysed the model for cylindrical geometry, that is the flow in a tube with active elastic walls.

Lastly, we analysed the auto-pulses in the channel with pre-existent non-constant width, namely the channel with global and local (partly blockading) narrowing.

The obtained results can be used in other areas of applicability of the nonlinear high-order partial differential equation considered in this thesis, such as reaction fronts and reaction-diffusion systems.

Certification of Thesis

This Thesis is entirely the work of **Fatima Zain Alabdeen Ahmed AHMED** except where otherwise acknowledged. The work is original and has not previously been submitted for any other award, except where acknowledged.

Student and supervisors signatures of endorsement are held at the University.

Principal Supervisor: Assoc. Prof. Dmitry Strunin.....Date.....

Associate Supervisor: Dr. Duc Ngo-Cong.....Date.....

Dedication

I dedicate this thesis to God Almighty, my creator and my master.
I also dedicate this work to the soul of my parents and aunt, who taught me the meaning of life and they are the origin of my success. I will always miss them, and they are never out off my mind and heart.
And then to my family; especially to my wonderful children Yousif, Zainab and Mustafa (little man) who have been affected in every way possible by this quest. I love you more than anything. God bless you.

Acknowledgments

It is a great pleasure to acknowledge the support of many kind people who have in one way or another contributed to the successful completion of this thesis.

First and foremost, I would like to thank God Almighty for giving me the strength, knowledge, ability and opportunity to complete this thesis satisfactorily. Without his blessings, this thesis would not have been completed.

The success of this thesis is attributed to the extensive support and assistance from my supervisor, Associate Professor Dmitry Strunin. I would like to express my grateful gratitude and sincere appreciation to him for his excellent scientific guidance, valuable advise, supervision and encouragement me during the whole period of my PhD study. Under his guidance I successfully overcame many difficulties and learned a lot. I hope that one day I would become as good an advisor to my students as Dr. Dmitry has been to me. I shall eternally be grateful to him for his assistance.

I would also like to express my gratitude to my co-supervisor Dr. Duc Ngo-Cong, who taught me how to approach numerical problems effectively. His profound experience lead this work to right direction. I enjoyed working together with him not only because of his experience and encouraging support, but also because of his patience and good sense of humor. Thanks to him for giving me his valuable feedback, and pushing me to better my work.

I owe a special thanks to my dear husband, Adham, who supported and encouraged me to pursue my dreams and finish my dissertation.

Very special thanks to my lovely children, Yousif, Zainab and Mustafa who are

the pride and joy of my life. Thank you for bearing with me and my mood swings and being my greatest supporters.

My heartfelt thanks go to my brothers and sisters. Because of their unconditional encouragement and prayers, I have the chance to finish my PhD Study.

I should not forget to acknowledge my friend, Mela, for providing support and friendship that I needed. Your friendly advice and big heart encouraged me to continue with my work.

I would like to thank the administrative staff at University of Southern Queensland (USQ) especially Mrs. Juanita Ryan, and Mrs. Rebecca Darr for their various forms of support during my PhD study.

Finally, great acknowledgements go to my Iraqi government for giving me the opportunity to complete the PhD Study.

Again, I would like to thank everyone who have supported and helped me directly or indirectly in the successful completion of my thesis.

Fatima Zain Alabdeen Ahmed AHMED

University of Southern Queensland

August 2019

Associated Publications

The following publications were produced during the period of candidature:

1. Ahmed, F. Z., Strunin, D. V., Mohammed, M. G. and Bhanot, R. P. (2016), 'Numerical solution for the fluid flow between active elastic walls', *Australian and New Zealand Industrial and Applied Mathematics (ANZIAM) Journal* [Oxford University Press] **57**, C221–C234.

2. Strunin, D. V. and Ahmed, F. Z., 'Parameters and branching auto-pulses in a fluid channel with active walls', The 29th International Symposium on Transport Phenomena (ISTP29), 30 October-2 November, 2018, Honolulu, USA [The Japan Society of Mechanical Engineers], paper ISTP29-059, presented, proceedings are not published; also in: *Fluids* [MDPI AG, Basel, Switzerland] **4**(3), p.160.

3. Ahmed, F. Z., Mohammed, M. G., Strunin, D. V. and Ngo-Cong, D. (2018), 'Simulations of autonomous fluid pulses between active elastic walls using the 1D-IRBFN method', *Mathematical Modelling of Natural Phenomena* [EDP science] **13**(5), p.47.

Contents

Acronyms & Abbreviations

NEP	Nonlinearly Excited Phase
CGLE	Complex Ginzburg-Landau Equation
KS	Kuramoto-Sivashinsky
1D-IRBFN	One-dimensional Integrated Radial Basis Function Network
PI	Picard Iteration
PI1	One-step Picard Iteration
PDE	Partial Differential Equation
ODE	Ordinary Differential Equation
FDM	Finite Difference Method
FEM	Finite Element Method
FVM	Finite Volume Method
RBF	Radial Basis Function
MQ	Multiquadric
DRBFN	Direct Radial Basis Function Network
IRBFN	Indirect/Integrated Radial Basis Function Network
RBF	Radial Basis Function
RBFN	Radial Basis Function Network
RHS	Right Hand Side

List of Figures

List of Tables

Keywords

Fluid, active elastic boundaries, branching channel flow, pulse, artificial artery, active dissipative systems, nonlinear partial differential equation, nonlinear excitation, One-dimensional Integrated Radial Basis Function Network (1D-IRBFN) method.

Chapter 1

Introduction

This chapter reviews basic notions of the dynamical systems including its definition and some of its important classes such as continuous and discrete systems, autonomous and non-autonomous systems, conservative and dissipative systems. Furthermore, the chapter displays the basic concepts of the lubrication theory. Finally, the objectives and the outline of the dissertation are introduced.

1.1 Overview of dynamical systems concepts

1.1.1 Dynamical system

Dynamical systems (DS) are mathematical objects that describe the temporal evolution of a state of a system according to some certain rules governing their evolution. A system of equations (differential, difference, integral, etc.), allowing the existence of a unique solution for each initial condition over an infinite period of time is used to describe a dynamical system. A state of a dynamical system is described fully by a set of phase variables. The set of all possible states of a dynamical system forms a phase space. A point in the phase space represents a state of the system while tem-

poral evolution of the dynamical system is depicted by trajectories moving among these points in the phase space. Thus, a trajectory is a geometrical representation of a solution to the system. A phase portrait or phase diagram is the collection of all possible trajectories of the system. Based on the state of time in which the system evolves, dynamical systems can be classified as a discrete dynamical system, arising in discrete time (maps) or as a continuous dynamical system, arising in continuous time (flow) (Rabinovich et al., 2000). A continuous dynamical system is usually described by a differential equation

$$\frac{dx}{dt} = f(x,t)\,; \quad x \in U \subseteq R^n,\, t \in R \tag{1.1}$$

possessing a unique solution $x(t,t_0) = x(t)$ satisfying the condition $x(t_0) = x_0$. Such systems, in turn, can be classified as autonomous and non-autonomous. We will give general definitions of autonomous and non-autonomous systems in Section 1.1.2. On the other hand, a discrete dynamical system is described by difference equations of the form $x_{t+1} = f(x_t, x_{t-1}, ..., x_{t-n}); \quad t \in Z$ or N or a logistic map, $x(t+1) = ax(t)(1-x(t))$, where $a \in [0,4]$ and $x \in [0,1]$ (Mukherjee and Poria, 2012). The dimension of the dynamical system is defined as the number of variables which are necessary to completely describe the system, and to account for all of its governing factors.

Dynamical systems can be further classified according to the equations used to describe the evolution of their state: linear and nonlinear. Most real-world problems are governed by nonlinear equations. It is well known that the nonlinear problems are generally more difficult to solve than the linear problems. As a result, frequently researchers resort to qualitative and numerical methods to obtain insight into the dynamical behaviour of such systems. General qualitative methods in the theory of nonlinear dynamics involve the classification and determination of equilibrium points, study of their stability, appearance and disappearance of these equilibria, and the transitions between them when the system parameter is changed. General reviews on dynamical systems can be found in (Alligood et al., 1997; Katok and Hasselblatt,

1997; Ott, 2002; Lakshmanan and Rajaseekar, 2012; Strogatz, 2014).

1.1.2 Autonomous and non-autonomous systems

As already mentioned, a continuous dynamical system can be classified as an autonomous and non-autonomous system. An autonomous equation does not explicitly depend on the independent variables (Beek et al., 1992),

$$dx/dt = f_t(x)\,, \quad x(t_0) = x_0\,.$$

Generally, the trajectories of such a system do not change in time. By contrast, a non-autonomous equation does involve time explicitly,

$$dx/dt = f_t(x,t)\,, \quad x(t_0) = x_0\,.$$

An example of an autonomous system is a damped linear harmonic oscillator equation

$$d^2x/dt^2 + b(dx/dt) + cx = 0, \quad b, c > 0\,,$$

in which the parameters b and c refer to the damping force and the restoring force, respectively. A linear oscillator with external time-dependent force is a non-autonomous dynamical system,

$$d^2x/dt^2 + b(dx/dt) + cx = A\cos(\varphi t)\,,$$

in which A and φ are, respectively, the amplitude and frequency of the driving force. This system is controlled by the time-dependent forcing function $A\cos(\varphi t)$, which is independent of the system's state (Layek, 2015). Due to the explicit dependence of the right hand-side term on t, the system is not self-governed. In the autonomous case, the initial time may always be taken as $t_0 = 0$, which is not permitted in the non-autonomous case.

It is important that the model (2.29) is autonomous, that is it contains no prescribed functions of time. As a result, all dynamic regimes generated by the equation represent self-behaviour of the system, not a passive response to an external influence.

1.1.3 Conservative and dissipative systems

As was mentioned at the beginning of this Chapter, two kinds of dynamical system are distinguished, namely, conservative and dissipative ones. For a conservative system, the volume in phase space is preserved during the time evolution while for a dissipative system, the volume is usually contracted due to energy dissipation. Also, the conservative and dissipative systems are defined with respect to the divergence of the corresponding vector field as follows: consider a system of N nonlinear first-order ordinary differential equations,

$$\frac{dx_n}{dt} = f_n(x_1, x_2, ..., x_N)\,, \quad n = 1, ..., N\,, \tag{1.2}$$

with $x \in R^N$, $t \in R^1$, $f : R^N \to R^N$; where t is time and f_n is a vector field. The divergence of the vector field $\mathrm{div} f_n = \sum_{n=1}^{N} \partial f_n / \partial x_n$, indicates the change of a given volume of initial conditions in the phase space. If the divergence is zero, the volume remains constant, and the system is said to be conservative. If the divergence is negative, the volume shrinks with time, and the system is dissipative. The volume in a dissipative system eventually goes to zero (Layek, 2015).

Conservative dynamical systems often arise in mechanics because of the Newtons laws, which can be represented in terms of Hamiltons equation as

$$\frac{\partial p_i}{\partial t} = \frac{\partial H}{\partial q_i}\,; \quad \frac{\partial q_i}{\partial t} = \frac{\partial H}{\partial P_i}\,, \tag{1.3}$$

where p_i and q_i are canonically conjugate state space variables and $H(p, q)$ is the Hamiltonian, which is related to energy. This relation between partial derivatives of conjugate variables is referred to as symplectic. Liouville's theorem guarantees that the phase space volumes are invariant under time evolution of the Hamiltonian system. Furthermore, energy conservation constrains the trajectories of the Hamiltonian system to lie on a hypersurface of constant energy. Though these may seem like strong constraints, they do not prevent complicated trajectories from appearing in low-dimensional Hamiltonian dynamics (Lam, 2003).

Dissipative systems are very important and the most abundant class of dynamical systems. Diffusion of heat, chemical reactions, heating of an electrical resistor are examples of dissipative phenomena. In general, dissipative systems arise in physical contexts related to dissipation, friction, viscosity, etc. (Strogatz, 2014). For example, mechanical systems without friction, which allow the description by Lagrange or Hamilton formalism relate to the class of conservative systems (Arnol'd, 2013; Abraham and Marsden, 2008). In the presence of friction, they become dissipative (Abraham and Marsden, 2008). Dissipative systems are subdivided into passive and active ones. The systems are said to be passive if they do not have any energy sources. Owing to dissipation the total energy of such systems decreases. On the other hand, the systems are said to be active if they have constant or time- dependent energy source. Active systems, in their turn, can be sub-classified into so called amplifiers and generators or self-oscillatory systems. The self-oscillatory systems are defined as those active systems in which undamped oscillations can occur without any external influence. In such systems, in contrast to the amplifier systems, the evolution of the dynamical variables is completely determined by the external force. An amplifier is a necessary but insufficient component of any self-oscillations system. To become a generator, an amplifier must be included in a feedback loop, so that a portion of the signal from the amplifier output is supplied to its input. Thus, a feedback loop must be an integral part of any self-oscillatory system (Landa, 2013). The main features of self-oscillations are as follows (Balanov et al., 2008),

- They are undamped, that is, the repetitive motion of the system does not stop and show the tendency to stop with the course of time.
- The system oscillates by themselves depending on the coordinates of the system only, not because of external influence.
- The shape, amplitude and time scale of these oscillations are defined by the properties of the system which cannot be easily changed by the outside influ-

ence, for example by setting different initial conditions.

Self-oscillations can take place in an autonomous system. It is important to note that the model (2.29) can be classified as an active dissipative system: its dissipative nature is due to the viscosity, and the active nature is due to the walls helping the pulse to propagate by exerting extra pressure and extra shear stress at any location along the channel at the time when the pulse arrives at that location. Consequently, the model yields pulse-shaped auto-wave solutions propagating with unique speed and amplitude.

1.2 Lubrication theory

This section introduces the basic concepts of the lubrication theory followed by a short introduction to the Reynolds equation. The equations that describe lubrication with continuous fluid films are derived from the basic equations of fluid dynamics through specialization to the particular geometry of the typical lubricant film. Lubricant films are distinguished by their small thickness relative to their lateral extent. If L_y and L_{xz} denote the characteristic dimensions across the film thickness and the plane of the film, respectively, as indicated in Fig. 1.1, then typical industrial bearings are characterized by $(L_y/L_{xz}) = O\,(10^{-3})$. This fact alone, and the assumption of laminar flow, allows us to combine the equations of motion and continuity into a single equation in lubricant pressure, the so-called Reynolds equation.

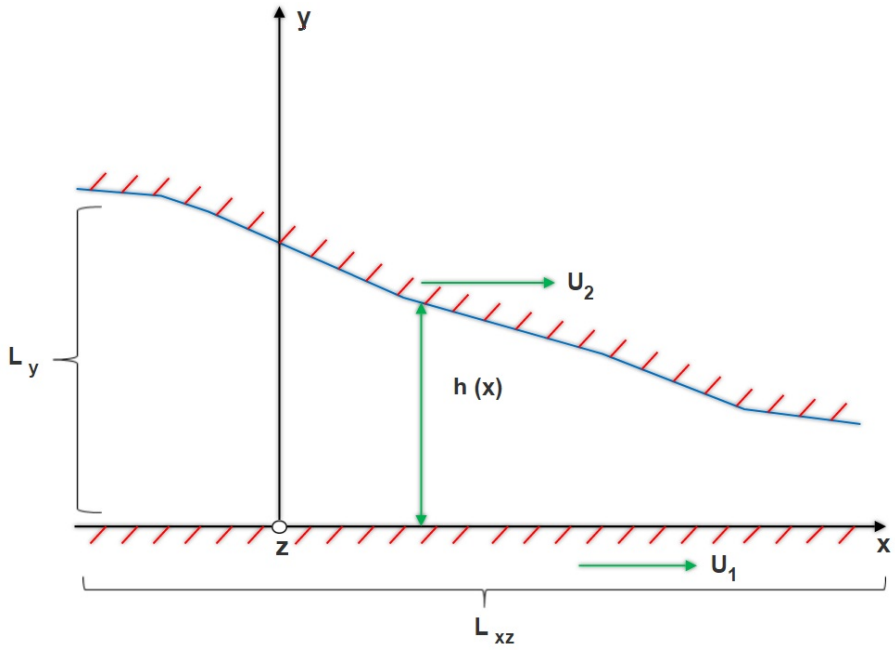

Figure 1.1: Schematic of lubricant film.

1.2.1 Basic Equations

As we mentioned earlier, the incompressible viscous fluid flow is governed by the equations of motion (the Navier-Stokes equations),

$$\rho\left[\frac{\partial \mathbf{u}}{\partial t} + (\mathbf{u}\cdot\nabla\mathbf{u})\right] = -\nabla p + \mu\nabla^2\mathbf{u} + \rho\,\mathbf{f} \tag{1.4}$$

and the continuity equation,

$$\nabla\cdot\mathbf{u} = 0\,. \tag{1.5}$$

To non-dimensionalize these equations, we normalize the orthogonal Cartesian coordinates (x, y, z) with the corresponding length scales

$$x = L_{xz}x_1\,, \quad y = L_y y_1\,, \quad z = L_{xz}z_1 \tag{1.6}$$

and the velocities with the velocity scale, U, in the $(x-z)$ plane and V perpendicular to it,

$$u = Uu_1\,, \quad v = Vv_1\,, \quad w = Uw_1\,. \tag{1.7}$$

The terms in the equation of continuity should be balanced, so the characteristic velocity V and U should depend on each other. Substitution Eq. (1.6) and Eq. (1.7) into Eq. (1.5) gives

$$\frac{\partial u_1}{\partial x_1} + \frac{VL_{xz}}{UL_y}\frac{\partial v_1}{\partial y_1} + \frac{\partial w_1}{\partial z_1} = 0\,. \tag{1.8}$$

The balance of the terms of the continuity equations is achieved provided that

$$\frac{VL_{xz}}{UL_y} = O(1)\,, \quad \text{or} \quad V = \left(\frac{L_y}{L_{xz}}\right)U\,. \tag{1.9}$$

Finally, the non-dimensional quantities for the pressure and time are defined as follows,

$$p_1 = r_e\frac{p}{\rho\, U^2}\,, \quad t_1 = \Omega t\,. \tag{1.10}$$

The reduced Reynolds number, r_e, and the nondimensional frequency, Ω, have the definition

$$r_e = \left(\frac{L_y}{L_{xz}}\right)\frac{L_y U}{v} \quad \text{and} \quad \Omega_1 = \left(\frac{L_y}{L_{xz}}\right)\frac{L_y\,(L_{xz}\Omega)}{v}\,,$$

where Ω is defined as the characteristic frequency of the system. For journal bearings, the characteristic frequency depends on the rotational velocity of the journal. By taking the shaft surface speed as the characteristic velocity, $U = R\,\omega$, and the journal radius as the characteristic length in the plane of the bearing, $L_{xz} = R$, we have $r_e \approx \Omega_1$. Based on this approximation, the equations of motion and continuity can be recast in terms of the dimensionless quantities as

$$\begin{aligned}
&r_e\left(\frac{\partial u_1}{\partial t_1} + u_1\frac{\partial u_1}{\partial x_1} + v_1\frac{\partial u_1}{\partial y_1} + w_1\frac{\partial u_1}{\partial z_1}\right) = -\frac{\partial p_1}{\partial x_1} + \frac{\partial^2 u_1}{\partial y_1^2} + \left(\frac{L_y}{L_{xz}}\right)^2\left(\frac{\partial^2 u_1}{\partial x_1^2} + \frac{\partial^2 u_1}{\partial z_1^2}\right)\,,\\
&\left(\frac{L_y}{L_{xz}}\right)^2\left[r_e\left(\frac{\partial v_1}{\partial t_1} + u_1\frac{\partial v_1}{\partial x_1} + v_1\frac{\partial v_1}{\partial y_1} + w_1\frac{\partial v_1}{\partial z_1}\right) - \frac{\partial^2 v_1}{\partial y_1^2} - \left(\frac{L_y}{L_{xz}}\right)^2\left(\frac{\partial^2 v_1}{\partial x_1^2} + \frac{\partial^2 v_1}{\partial z_1^2}\right)\right] = -\frac{\partial p_1}{\partial y_1}\,,\\
&r_e\left(\frac{\partial w_1}{\partial t_1} + u_1\frac{\partial w_1}{\partial x_1} + v_1\frac{\partial w_1}{\partial y_1} + w_1\frac{\partial w_1}{\partial z_1}\right) = -\frac{\partial p_1}{\partial z_1} + \frac{\partial^2 w_1}{\partial y_1^2} + \left(\frac{L_y}{L_{xz}}\right)^2\left(\frac{\partial^2 w_1}{\partial x_1^2} + \frac{\partial^2 w_1}{\partial z_1^2}\right)\,,
\end{aligned} \tag{1.11}$$

and

$$\frac{\partial u_1}{\partial x_1} + \frac{\partial v_1}{\partial y_1} + \frac{\partial w_1}{\partial z_1} = 0\,. \tag{1.12}$$

1.2.2 Lubrication Approximation

Resulting from the normalization in Eqs. (1.6), (1.7) and (1.10), we anticipate that each of the variable terms in Eqs. (1.11) and (1.12) are of the same order which is $O(1)$. But then the relative importance of the variable terms is decided only by the magnitude of the dimensionless parameters (L_y/L_{xz}) and r_e that multiply them.

Under normal conditions lubricant films are thin relative to their lateral extent. For liquid lubricated bearings $(L_y/L_{xz}) = O(10^{-3})$. The lubrication approximation of Reynolds is developed under the assumptions that $(L_y/L_{xz}) \to 0$ and $r_e \to 0$. Under these conditions Eq. (1.11) indicates that

$$\frac{\partial p_1}{\partial y_1} = O(10^{-6})\,, \quad \text{while} \quad \frac{\partial p_1}{\partial x_1} \approx \frac{\partial p_1}{\partial z_1} = O(1) \tag{1.13}$$

and Eqs. (1.11) and (1.12) reduce to

$$\frac{\partial p}{\partial x} = \mu \frac{\partial^2 u}{\partial y^2}\,, \quad \frac{\partial p}{\partial y} = 0\,, \quad \frac{\partial p}{\partial z} = \mu \frac{\partial^2 w}{\partial y^2}\,, \tag{1.14}$$

$$\frac{\partial u}{\partial x} + \frac{\partial v}{\partial y} + \frac{\partial w}{\partial z} = 0\,. \tag{1.15}$$

1.2.3 The Reynolds Equation

The second part of Eq. (1.14) confirms that the pressure does not vary across the film. But by integrating the first and last parts of Eq. (1.14) over y and applying the boundary conditions

$$\begin{aligned} u &= U_1\,, \quad w = 0 \quad \text{at} \quad y = 0 \\ u &= U_2\,, \quad w = 0 \quad \text{at} \quad y = h \end{aligned} \tag{1.16}$$

we obtain the velocity profiles

$$\begin{aligned} u &= \frac{1}{2\mu}\frac{\partial p}{\partial x}\left(y^2 - yh\right) + \left(1 - \frac{y}{h}\right)U_1 + \frac{y}{h}U_2\,, \\ w &= \frac{1}{2\mu}\frac{\partial p}{\partial z}\left(y^2 - yh\right)\,. \end{aligned} \tag{1.17}$$

The pressure distribution appearing in Eq. (1.17) and the velocity component v in Eq. (1.15) are yet unknown but we must satisfy the continuity equation. We substitute Eq. (1.17) into the averaged (across the film) continuity equation, which, upon interchanging the indicated differentiation and integration, gives

$$[v]_0^{h(x,t)} = -\frac{\partial}{\partial x}\left[\frac{1}{2\mu}\frac{\partial p}{\partial x}\int_0^{h(x,t)}\left(y^2 - yh\right)dy\right] - \frac{\partial}{\partial z}\left[\frac{1}{2\mu}\frac{\partial p}{\partial z}\int_0^{h(x,t)}\left(y^2 - yh\right)dy\right] - \frac{\partial}{\partial x}\int_0^{h(x,t)}\left[\left(1 - \frac{y}{h}\right)U_1 + \frac{y}{h}U_2\right]dy + U_2\frac{\partial h}{\partial x}\,. \tag{1.18}$$

The averaged velocity across the film is defined as

$$[v]_{y=0}^{h(x,t)} = -\left(V_1 - V_2\right) = \frac{dh}{dt}\,, \tag{1.19}$$

where V_1, V_2 are the normal velocities of the bearing surfaces. Finally, after some simplification, we get the generalized Reynolds equation that governs the pressure distribution in the lubricant film (Szeri, 2010),

$$\frac{\partial}{\partial x}\left(\frac{h^3}{\mu}\frac{\partial p}{\partial x}\right) + \frac{\partial}{\partial z}\left(\frac{h^3}{\mu}\frac{\partial p}{\partial z}\right) = 6\left(U_1 - U_2\right)\frac{\partial h}{\partial x} + 6h\frac{\partial\left(U_1 + U_2\right)}{\partial x} + 12\left(V_2 - V_1\right)\,. \tag{1.20}$$

For more details about the lubrication theory and the Reynolds equation we refer to (Nakayama, 2018; Bhushan, 2000).

1.3 Objectives of the present research

The objectives of the research can be stated as

- Develop numerical code based on the one-dimensional integrated radial basis networks (1D-IRBFN) method in order to solve the equation (Strunin, 2009*a*) of self-propagating fluid pulses (auto-pulses) through the channel simulating an artificial artery.

- Use the numerical code developed in item (1) to obtain a range of numerical solutions under different initial and boundary conditions and also study nonlinear interaction of pulses during their propagation.
- Evaluate the empirical coefficients of the model responsible for the active motion of the walls.
- Calculate the fluid mass flux due to the pulses.
- Using the model of Strunin as the base, construct and explore a model for branching channel.
- Derive and analyze the model for the flow between active elastic walls when the cross-sectional area of the flow is circular.
- Analyze the auto-pulses for the flow with non-constant cross-section.

1.4 Outline of the Thesis

This thesis consists of nine chapters which are organised as follows:

Chapter 1 introduces a brief review of dynamical systems including some of its important classes such as continuous-time and discrete-time systems, conservative and dissipative systems, autonomous and non-autonomous systems. This is then followed by a review of the basic concepts of the lubrication theory. Finally, the chapter outlines the main objectives of the present research.

Chapter 2 presents the literature review and motivation of the present study. Here, we give the overall review of the semi-empirical model of self-propagating fluid pulses (auto-pulses) through the channel. Then, we discuss the works which have been done previously for linearly and nonlinearly excited phase equations, which constitute mathematical foundation of the current model.

Chapter 3 presents the numerical 1D-IRBFN method which is used in our research

project. Some examples are used to assess its performance and accuracy.

Chapter 4 presents and discusses numerical solutions of the autonomous model of auto pulses in the plane channel using homogeneous and periodic boundary conditions.

Chapter 5 gives the calculation of the fluid mass flux carried out by the pulse. Using the values of mechanical parameters from literature, we evaluate the empirical coefficients of the model responsible for the active motion of the walls.

Chapter 6 presents and discusses numerical solutions of the model adapted for a branching channel, using homogeneous boundary conditions at the edges and continuity conditions at the branching (contact) point.

Chapter 7 presents the derivation of the autonomous model of fluid pulses between hypothetically active elastic walls when the channel has circular cross-section.

Chapter 8 presents the numerical solutions for the channel with pre-existent non-constant width.

Chapter 9 describes significance of the thesis and gives concluding remarks.

1.5 Concluding Remarks

The fundamental concepts of dynamical systems such as continuous and discrete systems, autonomous and non-autonomous systems, conservative and dissipative systems are briefly reviewed. This is then followed by a review of the basic concepts of the lubrication theory.

Chapter 2

Literature Review

2.1 Introduction

This chapter starts with the motivation for the present research. Then it presents the overall review of the semi-empirical model of self-propagating fluid pulses (auto-pulses) through the single channel. The key mechanism behind the model is the active motion of the walls similarly to the earlier model of Roberts. With these comprehensive explanations, the chapter also presents general review of the phase equations with both linear and nonlinear excitation.

2.2 Motivation

The following equation, which is the focus of this study, is an example of an autonomous system formulated by Strunin (2009*a*) to model pulses in a hypothetical artificial artery,

$$\frac{\partial w}{\partial t} = \frac{D}{3\eta}\frac{\partial}{\partial x}\left[H^3\frac{\partial^5 w}{\partial x^5}\right] - \frac{\alpha}{3\eta}\frac{\partial}{\partial x}\left[H^3\frac{\partial}{\partial x}\left(w^4\right)\right] + \beta\frac{\partial}{\partial x}\left(H^3 w^5\right) . \qquad (2.1)$$

Dynamically the term $\partial_x \left[H^3 \partial_x^5 w\right]$ is dissipative, the nonlinear term $-\partial_x \left[H^3 \partial_x \left(w^4\right)\right]$ represents excitation, and the nonlinear term $\partial_x (H^3 w^5)$ transfers the energy from the excitation to dissipation. In this model the pulse occurs due to the active motion of the walls. The proposed research will be a significant step forward relative to the research published so far, because it offers theoretical principles on which the design of artificial arteries may be based, and also because the model (2.1) has other applications that go beyond the phenomenon of fluid pulses in channels as discussed below. Of course we acknowledge that the half-empirical model has limitations in describing the very complex bio-physical process. In its simplest configuration the model is based on plane-parallel geometry. Then it is modified to describe the case of cylindrical channel. We anticipate that information obtained as a result of this project may have practical importance in terms of understanding general qualitative properties of the propagating pulses, for example the effects of branching flows and pulse interactions.

Structurally the model (2.1) is similar to the nonlinearly excited phase (NEP) equation derived for the spinning combustion fronts (Strunin, 1999) and non-local reaction-diffusion systems (Strunin, 2009*b*; Strunin and Mohammed, 2015). Note that the combustion systems are active and dissipative: their active character is due to heat generation in a chemical reaction, and their dissipative character is due to heat conductivity. The combustion fronts and fluid pulses described by (2.1) have similar underlying dynamic features which place them into the same category of active dissipative systems. The analogy with the combustion front equations indicates that the model (2.1) should be capable of generating auto-wave solutions in the form of pulses. Our plan in this dissertation is to show this by solving the equation (2.1) numerically, analyse the solutions including single and multiple-pulse solutions, evaluate the empirical parameters α and β and evaluate the fluid flux carried out by the pulses.

2.3 Modelling blood flow in real arteries

The arteries perform a regular beating, called the pulse, which follows the heart beat and propagates in the form of pulse waves (Alastruey et al., 2012). Generally speaking, blood exhibits non-Newtonian fluid behaviour. Its viscosity is dependent on the flow at all flow velocities (Ku, 1997). However, in the large arteries, blood can be assumed to be a homogenous and Newtonian fluid (Vlachopoulos et al., 2011).

Arterial blood flows are usually modelled by the classical Navier-Stokes equations. However, under certain conditions, non-Newtonian models are also used (Robertson et al., 2008, 2009; Bessonov et al., 2016).

When modelling the blood motion in an artery, some researchers suppose that the arterial wall is rigid (Quarteroni et al., 2002) while others assume it to be elastic (Alastruey Arimon, 2006). Roberts (1994) presented a simple argument why the elasticity of an artery is important: if arteries were not elastic then each pump of the heart would cause an immediate rise in blood pressure throughout the body. The arterial wall is easily extensible and is more analogous to substances such as rubber, that are often classified as elastomers and undergo large deformations. The main elastic components of the arterial wall are collagen and elastin, which are fibrous in nature. They have different elastic modulus and different attachment to smooth muscles, therefore, generally speaking the arterial wall is not homogeneous (Vlachopoulos et al., 2011). Due to their elastic properties, the arterial walls easily interact with the blood flow. The muscular walls of the artery help the heart pump the blood. Majority of mathematical models treat arteries as passive material (Sherwin et al., 2003; Kleinstreuer, 2006). A popular approximation of the flow-artery interaction is the proportionality between the increments in the artery's cross-sectional area and the flow pressure (Olufsen et al., 2000),

$$p - p_0 \sim \sqrt{A} - \sqrt{A_0}\,,$$

where p_0 and A_0 are the reference pressure and cross-sectional area respectively. Studies of the mechanics of pulse propagation through an artery typically focus on passive response to the time-pulsating boundary condition imposed at the artery's inlet (Matthys et al., 2007). However, the arteries contain muscles which help to push the blood. Haff and Triplett (2015) noted that "... arteries have strong, muscular walls. Small branches of arteries called arterioles act as control vessels through which blood enters the capillaries. .... Arterioles have strong, muscular walls that are capable of closing to a great degree and thereby act as a reservoir for blood, either in small or in large amounts...". For narrow arteries the two principal factors influencing the blood flow are pressure gradient and viscous resistance from the walls.

2.4 Modelling blood flow in artificial arteries

In this research, we focus on a mathematical model to simulate an artificial artery with *actively* moving walls. Putting aside the technological challenges of construction of such a sophisticated device, we aim to establish theoretical principles of how the artificial walls need to move in order to facilitate a uni-directional fluid flow. Note that the recent years saw a remarkable progress in design and fabrication of artificial muscles. For example, the recent paper (Li et al., 2017) describes the fluid-driven and origami-inspired artificial muscles which can be programmed to achieve not only contraction, bat also bending and torsion at multiple scales.

Our analysis is based on the model (Strunin, 2009*a*), which further developed the ideas of Roberts (1994) of channels with active walls. While Roberts considered the case of negligible viscous forces compared to inertia, which is relevant to wider channels (this will be discussed in Section 2.4.1), we will consider the case when inertia is negligible compared to viscous forces, which is relevant to narrow channels (Section 2.4.2).

2.4.1 Non-autonomous model in the case of inertia prevailing over viscosity

Roberts considered a long cylindrical channel with cross-sectional area $A(x,t)$. With the x-axis directed along the channel, the mass continuity equation is written as

$$\frac{\partial A}{\partial t} + \frac{\partial (Av)}{\partial x} = 0\,,$$

where $v(t)$ is the velocity of the fluid flow. Substituting the circular cross section, $A = \pi R^2$, where $R(x,t)$ is the radius of the channel, we get

$$\frac{\partial R}{\partial t} + v\frac{\partial R}{\partial x} + \frac{1}{2}R\frac{\partial v}{\partial x} = 0\,. \tag{2.2}$$

Because the wall's material is elastic, an increase in the local pressure leads to an increase in the radius,

$$p - p_* = \alpha(R - R_*)\,, \tag{2.3}$$

where p_* and R_* are the neutral pressure and radius of the channel respectively and $\alpha > 0$ is a constant which depends on mechanical characteristics of the wall. The momentum equation without viscous friction has the form

$$\frac{\partial v}{\partial t} + v\frac{\partial v}{\partial x} = -\frac{1}{\rho}\frac{\partial p}{\partial x}\,, \tag{2.4}$$

where ρ is the fluid density. Substituting (2.3) into (2.4), we get

$$\frac{\partial v}{\partial t} + v\frac{\partial v}{\partial x} = -\frac{\alpha}{\rho}\frac{\partial R}{\partial x}\,. \tag{2.5}$$

Equations (2.2), (2.5) form a system of two equations with respect to the two unknown functions $R(x,t)$ and $v(x,t)$. Assuming they experience only small departures, $\hat{R}$ (from R_*), and $\hat{v}$ (from 0), using (2.2)-(2.4) we obtain the wave equation

$$\frac{\partial^2 \hat{v}}{\partial t^2} = c_*^2 \frac{\partial^2 \hat{v}}{\partial x^2}\,,$$

where $c_* = [\alpha R_*/(2\rho)]^{1/2}$. Its D'Alembert's solution

$$\hat{v} = f(x - c_* t) + g(x + c_* t)$$

describes waves travelling in an unchanging form with the speed c_*.

Roberts postulated that the wall, when it contracts, produces an extra pressure term in the $p - R$ relationship,

$$p = p_* + \alpha(R - R_*) + P(x,t)\,, \tag{2.6}$$

where $P(x,t)$ is a prescribed function of x and t. Substituting (2.6) into the continuity and momentum equations (2.2), (2.4) and linearizing we get the forced linear wave equation

$$\frac{\partial^2 \hat{v}}{\partial t^2} = c_*^2 \frac{\partial^2 \hat{v}}{\partial x^2} - \frac{1}{\rho}\frac{\partial^2 P}{\partial x \partial t}\,, \tag{2.7}$$

where the last term is responsible for the active action of the wall. The active pressure is assumed to have the form of a wave,

$$P(x,t) = P_0(t - x/c_0)\,,$$

where P_0 has the shape of a twitch (pulse). It describes a squeezing motion which travels down the artery with the speed c_0. The general solution of equation (2.7) is

$$\widehat{v} = \frac{c_0}{\rho\,(c_0^2 - c_*^2)} P_0\,(t - x/c_0) + f(x - c_* t) + g(x + c_* t)\,, \tag{2.8}$$

which describes the forced flow due to the action of the wall and also the free, elastic wave propagating along the channel. Observe the difference $c_0^2 - c_*^2$ in the denominator in (2.8). Roberts pointed out that, if the speed of the forced wave is sufficiently close to the speed of the free elastic wave, the forced wave becomes very large. We add that this is a resonant-type phenomenon where the external force is synchronized with the self-oscillation of the system. Loosely the dynamic is as follows. The force kick-starts a wave which propagates to the neighbouring region with the speed c_*. Simultaneously the force itself, represented by P_0, moves to that region and kicks again (of course, this is not a discrete but a smooth process). Since the speed of the force, c_0, is close to c_*, the force is effectively synchronized with the pulse. The product $c_0/(c_0^2 - c_*^2) \cdot P_0$ represents a non-decaying pulse caused by the active motion of the wall.

The fact that P_0 explicitly depends on t and x suggests that the resulting pulse-shaped solution (2.8) is dictated by the force and has a prescribed shape (Roberts suggested that P_0 should be linked to the action of the heart). From mathematical viewpoint, this renders the model non-autonomous.

2.4.2 Autonomous model in the case of viscosity prevailing over inertia

Strunin (2009*a*) formulated an autonomous model of pulse propagation in a hypothetical artificial channel. For simplicity he considered a theoretical configuration of the flow contained between unbounded active elastic walls shaped (in the rest state) as planes. The model was partly derived from physical principles, namely the classical lubrication theory for the flow coupled with the theory of elasticity for the wall, and partly using phenomenological arguments.

In line with the model of Roberts (1994), Strunin assumed that synchronization takes place, however in a different form to (Roberts, 1994). He supposed that the walls help the pulse to propagate by exerting extra pressure and extra shear stress at a location along the channel at the time when the pulse arrives at that location. But unlike the model (Roberts, 1994) he considered the case when viscous friction dominates over inertia. This is done via the lubrication theory based on the balance between the pressure gradient and viscous friction. The phenomenology of the model transpires through specific form of additional terms representing active components of the pressure and shear stress produced by the walls. Using the dynamical system terminology, the model can be classified as active-dissipative and the pulses as auto-waves, that is self-supported dissipative structures. Unlike conservative waves, for example surface waves in fluids, the auto-waves have unique values of the velocity, width and amplitude.

The model had to meet the following requirements: (1) it should yield pulse-

shaped auto-wave solutions; (2) these solutions should be "basic" that is an arbitrary initial condition would always break down into more or less identical pulses, their shape and speed being determined by the system's dynamical laws and not the initial conditions; (3) the motion of the wall should be cyclic, that is every small piece of the wall should return to its initial position after each pulse; this would ensure that the wall remains undisplaced on average; (4) the pulses propagate in one direction only; (5) the pulses transport fluid mass in that direction; (6) the model should include viscous effects. The model (Strunin, 2009*a*) satisfies requirements (1)–(6); it has the form

$$\frac{\partial w}{\partial t} = \frac{D}{3\eta}\frac{\partial}{\partial x}\left[H^3\frac{\partial^5 w}{\partial x^5}\right] - \frac{Eh}{6\eta(1-\nu^2)}\frac{\partial}{\partial x}\left[H^3\frac{\partial^2}{\partial x^2}\left(\frac{\partial w}{\partial x}\right)^3\right] - \frac{\alpha}{3\eta}\frac{\partial}{\partial x}\left[H^3\frac{\partial}{\partial x}\left(w^4\right)\right] + \beta\frac{\partial}{\partial x}\left(H^3 w^5\right) , \tag{2.9}$$

where w is the deflection of the wall from the neutral position H_0, so that $H(x,t) = H_0 + w(x,t)$, with H being counted from the middle of the channel (see Fig. 2.1), the coordinate x is directed along the flow, D is the flexural rigidity of the wall, E is the Young's modulus, h is the thickness of the wall, ν is Poisson's ratio, and η is the viscosity.

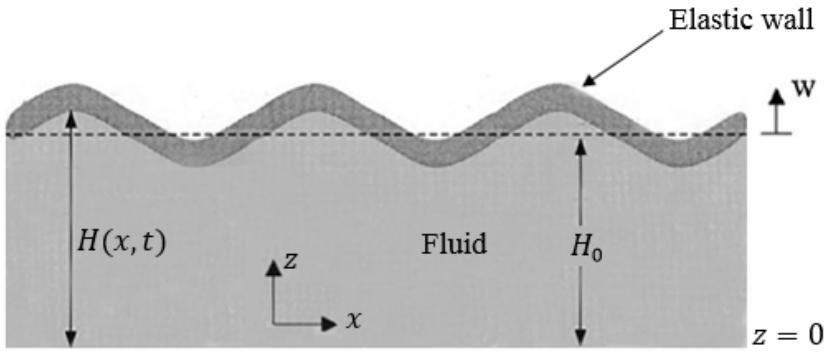

Figure 2.1: The fluid flow between elastic walls (half of the channel is shown).

2.5 Derivation of the autonomous viscous model

In this section, for convenience, we present the derivation of the model (Strunin, 2009*a*). The condition of zero average horizontal displacement of the wall has been modified compared to the original version.

Consider the flow between infinite elastic walls, assuming symmetry with respect to the middle plane, $z = 0$; hence it will suffice to analyse only half of the flow, $0 < z < H(x,t)$. All unknown functions are uniform in the y-direction. Assuming that fluid inertia is small compared to viscous friction, we apply the lubrication theory (Huang and Suo, 2002), which equates the pressure gradient to the viscous force,

$$\frac{\partial^2 v}{\partial z^2} = \frac{1}{\eta}\frac{\partial p}{\partial x}\,, \tag{2.10}$$

where x and z are the coordinates along and across the flow respectively, $v(x,z,t)$ the flow velocity in the x direction, $p(x,t)$ is the pressure, and η the viscosity. The pressure is assumed z-independent, so that integrating (2.10) on z gives

$$v = \frac{1}{2\eta}\frac{\partial p}{\partial x}\left(z^2 - H^2\right) + v(x,H,t)\,. \tag{2.11}$$

The mass flux is

$$Q = \int_0^H v\,dz = -\frac{H^3}{3\eta}\frac{\partial p}{\partial x} + v(x,H,t)\,H\,. \tag{2.12}$$

We define the displacement, $w(x,t)$, of the wall in the z-direction from the neutral position, $H = H_0$, by

$$H = H_0 + w\,. \tag{2.13}$$

Then the continuity equation becomes

$$\frac{\partial w}{\partial t} + \frac{\partial Q}{\partial x} = 0\,. \tag{2.14}$$

Substituting (2.12) into (2.14) gives

$$\frac{\partial w}{\partial t} = \frac{\partial}{\partial x}\left[\frac{H^3}{3\eta}\frac{\partial p}{\partial x} - v(x,H,t)\,H\right]\,. \tag{2.15}$$

Equation (2.15) links the displacement of the flow boundary, coinciding with the wall position, to the flow pressure. The elasticity theory (Landau and Lifshitz, 1959; Timoshenko and Woinowsky-Krieger, 1987) provides the reverse link from the pressure to the displacement

$$p = D\frac{\partial^4 w}{\partial x^4} - \frac{\partial}{\partial x}\left(N\frac{\partial w}{\partial x}\right), \tag{2.16}$$

where

$$N = \frac{Eh}{1-\nu^2}\left[\frac{\partial u}{\partial x} + \frac{1}{2}\left(\frac{\partial w}{\partial x}\right)^2\right]. \tag{2.17}$$

In (2.16) and (2.17) $u(x,t)$ is the wall's displacement along the flow, D is the flexural rigidity of the wall, E is Young's modulus, h is the thickness of the wall, ν is Poisson's ratio, and N the force caused by the displacements. Substituting (2.17) and (2.16) into (2.15), and using the no-slip boundary condition,

$$v(x,H,t) = \frac{\partial u}{\partial t},$$

we obtain

$$\begin{aligned}\frac{\partial w}{\partial t} = {} & \frac{D}{3\eta}\frac{\partial}{\partial x}\left(H^3\frac{\partial^5 w}{\partial x^5}\right) - \frac{Eh}{6\eta(1-\nu^2)}\frac{\partial}{\partial x}\left[H^3\frac{\partial^2}{\partial x^2}\left(\frac{\partial w}{\partial x}\right)^3\right] \\ & -\frac{Eh}{3\eta(1-\nu^2)}\frac{\partial}{\partial x}\left[H^3\frac{\partial^2}{\partial x^2}\left(\frac{\partial u}{\partial x}\frac{\partial w}{\partial x}\right)\right] - \frac{\partial}{\partial x}\left(\frac{\partial u}{\partial t}H\right).\end{aligned} \tag{2.18}$$

The shear stress in the fluid is represented as usual by $T = \eta\,\partial v/\partial z$, therefore on the boundary, $z = H$, using (2.11),

$$T = \frac{\partial p}{\partial x}H. \tag{2.19}$$

This shear stress must be equal to the shear stress produced by the wall,

$$T = \frac{\partial N}{\partial x}. \tag{2.20}$$

Equating (2.19) and (2.20) with the use of (2.17), we have

$$\frac{E}{1-\nu^2}\left[\frac{\partial^2 u}{\partial x^2} + \frac{1}{2}\frac{\partial}{\partial x}\left(\frac{\partial w}{\partial x}\right)^2\right] = \frac{\partial p}{\partial x}H. \tag{2.21}$$

The three equations (2.18), (2.21) and (2.16) form a closed system with respect to the three functions of interest $w(x,t)$, $u(x,t)$ and $p(x,t)$. Now suppose that, when deflecting from the neutral position, the elastic walls exert extra pressure relative to (2.16),

$$p = D\frac{\partial^4 w}{\partial x^4} - \frac{\partial}{\partial x}\left(N\frac{\partial w}{\partial x}\right) + p_0 + p_1\,, \tag{2.22}$$

where p_0 is a constant (reference pressure) and p_1 depends on w. We postulate that p_1 is proportional to the 4^{th} power of the vertical displacement,

$$p_1 = -\alpha w^4\,, \quad \alpha > 0\,. \tag{2.23}$$

Further, we suppose that the walls actively move along the flow, thereby producing an extra shear stress relative to (2.21). We postulate that the wall's motion along the flow, represented by the displacement u and velocity $\partial u/\partial t$, is coupled with w. Specifically, the $H-$weighted velocity along the flow, $H\partial u/\partial t$, combined with the other $u-$containing term in (2.18), depends on w as

$$-\frac{Eh}{3\eta(1-\nu^2)}H^3\frac{\partial^2}{\partial x^2}\left(\frac{\partial u}{\partial x}\frac{\partial w}{\partial x}\right) - \frac{\partial u}{\partial t}H = H^3\beta w^5 - K\,, \quad \beta > 0\,, \tag{2.24}$$

where K is a constant. The value of K is an eigenvalue of the settled pulse regime; it will be appropriately selected to ensure that the horizontal displacement of the wall after each pulse is zero. This relation implies that an extra (active) shear stress is applied by the wall; we denote it T_1. The total stress satisfies the continuity condition on the boundary

$$T_1 + \frac{E}{1-\nu^2}\left[\frac{\partial^2 u}{\partial x^2} + \frac{1}{2}\frac{\partial}{\partial x}\left(\frac{\partial w}{\partial x}\right)^2\right] = \frac{\partial p}{\partial x}H\,, \tag{2.25}$$

where the pressure p is represented by (2.22). Although we are not able to justify the concrete powers of w used in (2.23) and (2.24), these relations at least state that the larger the deformation w the larger active response from the wall, which seems reasonable. Under the assumptions (2.22), (2.23) and (2.24), the equation (2.18)

governing the dynamics of the vertical displacement becomes u-independent:

$$\frac{\partial w}{\partial t} = \frac{D}{3\eta}\frac{\partial}{\partial x}\left[H^3\frac{\partial^5 w}{\partial x^5}\right] - \frac{Eh}{6\eta(1-\nu^2)}\frac{\partial}{\partial x}\left[H^3\frac{\partial^2}{\partial x^2}\left(\frac{\partial w}{\partial x}\right)^3\right] - \frac{\alpha}{3\eta}\frac{\partial}{\partial x}\left[H^3\frac{\partial}{\partial x}\left(w^4\right)\right] + \beta\frac{\partial}{\partial x}\left(H^3 w^5\right)\,. \tag{2.26}$$

It is important to require that the overall displacement of the wall over one period, T, is zero,

$$\int_T \frac{\partial u}{\partial t}\,dt = 0\,, \quad \int_T \frac{\partial w}{\partial t}\,dt = 0\,. \tag{2.27}$$

The second condition in (2.27) is guaranteed provided the boundary conditions are periodic. Indeed, each term in the equation's right-hand side is a derivative and the expression under differentiation is periodic. The first condition of (2.27) can be transformed using (2.24) to the form

$$\int_T \left[-\frac{Eh}{3\eta(1-\nu^2)}H^2\frac{\partial^2}{\partial x^2}\left(\frac{\partial u}{\partial x}\frac{\partial w}{\partial x}\right) - \beta H^2 w^5 + \frac{K}{H}\right]\,dt = 0\,, \tag{2.28}$$

which can be met by selecting K. The procedure of finding solution is as follows. The function $w(x,t)$ is obtained from (2.26) under, say, periodic boundary conditions. Then $u(x,t)$ and K are found from (2.24),(2.28) for the settled pulse regime. Lastly, the pressure is obtained from (2.22), (2.23), and the extra shear stress $T_1(x,t)$ and total stress from (2.25).

Qualitative analysis carried out in (Strunin, 2009*a*) shows that an individual pulse is the result of the dynamical balance between the three terms in the right side of equation (2.26). The term containing E is not crucial for the balance; it comes from the classical elasticity and has dissipative effect, while the crucial dissipative term is the 6th-order derivative. If E is sufficiently small, the E-containing terms can be neglected. In this case the main equation (2.26) takes the simpler form

$$\frac{\partial w}{\partial t} = \frac{D}{3\eta}\frac{\partial}{\partial x}\left[H^3\frac{\partial^5 w}{\partial x^5}\right] - \frac{\alpha}{3\eta}\frac{\partial}{\partial x}\left[H^3\frac{\partial}{\partial x}\left(w^4\right)\right] + \beta\frac{\partial}{\partial x}\left(H^3 w^5\right)\,. \tag{2.29}$$

and the condition (2.28) becomes

$$\int_T \left(-\beta H^2 w^5 + \frac{K}{H}\right)\,dt = 0\,. \tag{2.30}$$

Assuming

$$w << H_0$$

we can replace H by $H = H_0 + w \approx H_0$ in equation (2.29) to get

$$\frac{\partial w}{\partial t} = \frac{DH_0^3}{3\eta}\frac{\partial^6 w}{\partial x^6} - \frac{H_0^3\alpha}{3\eta}\frac{\partial^2}{\partial x^2}\left(w^4\right) + H_0^3\beta\frac{\partial}{\partial x}\left(w^5\right) . \tag{2.31}$$

As we mentioned earlier, structurally the model (2.31) is similar to the spinning combustion equation (Strunin, 1999) and the model of the non-local reaction-diffusion systems (Strunin, 2009*b*; Strunin and Mohammed, 2015). An individual pulse is formed by the dynamical balance between the three terms in the right-hand side of (2.31),

$$H_0^3\frac{D}{3\eta}w^{VI} \sim -H_0^3\frac{\alpha}{3\eta}(w^4)'' \sim H_0^3\beta(w^5)' . \tag{2.32}$$

This relationship determines the characteristic scales for the height, Δw, and width, Δx, of an individual pulse. They will be independent of H_0 since H_0^3 can be cancelled out in (2.32) (for the adopted versions of the active stress and pressure; note that other versions are possible, in which case w may depend on H_0).

The model Strunin (2009*a*) can be extended to cylindrical geometry using polar coordinates. This will be done in Chapter 7. In this case, the displacement w is introduced by

$$R(x,t) = R_0 + w , \tag{2.33}$$

where R_0 is the neutral radius of the cylinder.

2.6 Complex Ginzburg-Landau equation (CGLE)

Another area of application of equation of the type (2.31) is reaction diffusion systems. Therefore significance of the present dissertation extends to such systems as well. An equation similar to (2.31) describes the dynamics of the phase of oscillations of concentrations in some reaction-diffusion systems, where there is non-local

interaction between reactants. In this an following subsections we briefly outline this area of applicability of equation (2.31).

The starting point is the cubic complex Ginzburg Landau equation (CGLE); it is one of the universal equation governing the weakly nonlinear behavior of dissipative systems. It is able to describe a vast variety of nonequilibrium phenomena, such as the generation of spatiotemporal dissipative structures in lasers (Haken, 1983; Jakobsen et al., 1992; Harkness et al., 1994), binary fluid convection (Kolodner et al., 1988; Kolodner, 1991), and phase transitions (Graham and Riste, 1975). In fact, the CGL equation describes the slow modulations of oscillations near a Hopf bifurcation point in a continuous system (for example see Kuramoto, 1984*a*; Saarloos et al., 1994).

The equation has the form

$$\partial_t A = A + (1 + ib)\Delta A - (1 + ic)|A|^2 A\,, \tag{2.34}$$

where A is a complex function of (scaled) time t and space x. Under the form (2.34), the CGL equation has been reduced (without loss of generality) to simplest form, with only two real parameters, b and c which characterise linear and nonlinear dispersion respectively.

Newell and Whitehead (1969) presented the derivation of Eq. (2.34) as an amplitude modulation equation for modelling the onset of instability in fluid convection problems. In these situations, at some critical parameter value, a spatially homogeneous steady state loses stability to oscillations whose frequency and wavelength can be understood in terms of a linearised equation. Newell and Whitehead found that when nonlinear effects are included, these oscillations are modulated over long time and space scales by a quantity A satisfying (2.34) (García-Morales and Krischer, 2012). Also, it was derived in the studies of Poiseuille flow (Stewartson and Stuart, 1971), reaction-diffusion systems (Ermentrout, 1981), and chemical reactors (Kuramoto, 1984*a*). More detailed explanation to the CGL equation and its solutions can be found in (Manneville, 1990; Walgraef, 2012; Aranson and Kramer, 2002; Bowman and Newell, 1998).

2.7 Linear excitation in the phase equation

The general form of the phase equation is

$$\begin{aligned}\partial_t u =& a_1 \bigtriangledown^2 u + a_2 \left(\bigtriangledown u\right)^2 + \\ & b_1 \bigtriangledown^4 u + b_2 \bigtriangledown^3 u \bigtriangledown u + b_3 \left(\bigtriangledown^2 u\right)^2 + b_4 \bigtriangledown^2 u \left(\bigtriangledown u\right)^2 + b_5 \left(\bigtriangledown u\right)^4 + \\ & g_1 \bigtriangledown^6 u + g_2 \bigtriangledown^5 u \bigtriangledown u + g_3 \bigtriangledown^4 u \bigtriangledown^2 u + g_4 \left(\bigtriangledown^3 u\right)^2 + g_5 \bigtriangledown^4 u \left(\bigtriangledown u\right)^2 + \\ & g_6 \left(\bigtriangledown^2 u\right)^3 + g_7 \bigtriangledown^3 u \bigtriangledown^2 u \bigtriangledown u + g_8 \bigtriangledown^3 u \left(\bigtriangledown u\right)^3 + g_9 \left(\bigtriangledown^2 u\right)^2 \left(\bigtriangledown u\right)^2 + \\ & g_{10} \bigtriangledown^2 u \left(\bigtriangledown u\right)^4 + g_{11} \left(\bigtriangledown u\right)^6 + \\ & e_1 \bigtriangledown^8 u + \cdots , \end{aligned} \tag{2.35}$$

where a_n, b_n, g_n, e_n, ... are constant coefficients. The right-hand side of (2.35) can be viewed as a power series in small parameter $\bigtriangledown^2 \sim (1/L)^2$, where L is the large characteristic spatial scale of variations of u.

Eq. (2.35) can be truncated to a finite number of terms, as needed to achieve a balance. The simplest forms are the classical 2nd order (in $\bigtriangledown$) diffusion equation

$$\partial_t u = a_1 \bigtriangledown^2 u \,, \quad a_1 > 0 \,, \tag{2.36}$$

that can be transformed into the Burgers' equation by adding the quadratic nonlinear term $a_2 \left(\bigtriangledown u\right)^2$. Both equations are dissipative as they have no excitation terms. However, some systems have its own energy source. The diffusion equation transforms into anti-diffusion, when the value of the coefficient in front of $\bigtriangledown^2 u$ becomes negative. Thus, the amplitude of u will grow. One can say that the anti-diffusion brings about excitation to the system. In order to prevent a blow-up and preserve the balance, a truncation must be of higher-order in $\bigtriangledown$. This observation motivated researchers to derive higher-order equations. For example, a fourth-order phase equation, namely the Kuramoto-Sivashinsky (KS) equation, was independently derived by Kuramoto and co-authors (Kuramoto and Tsuzuki, 1976; Kuramoto, 1984*b*) in the contexts of reaction-diffusion systems and Sivashinsky (1977) in the context

of cellular flame. This equation has the form,

$$\partial_t u = a_1 \bigtriangledown^2 u + a_2 \left(\bigtriangledown u\right)^2 + b_1 \bigtriangledown^4 u \,. \tag{2.37}$$

In (2.37), dynamically the linear anti-diffusion term, $a_1 \bigtriangledown^2 u$ with $a_1 < 0$, represents excitation, $b_1 \bigtriangledown^4 u$ with $b_1 < 0$ represents dissipation and the nonlinear term $a_2 \left(\bigtriangledown u\right)^2$ transfers the energy from large to small scales. Nikolaevskiy derived a 6th-order equation for seismic waves in granular media,

$$\partial_t u = a_1 \bigtriangledown^2 u + b_1 \bigtriangledown^4 u + g_1 \bigtriangledown^6 u + a_2 \left(\bigtriangledown u\right)^2 \,. \tag{2.38}$$

Similarly to the Kuramoto-Sivashinsky (KS) equation, the Nikolaevskii equation is based on a linear excitation expressed this time by $b_1 \bigtriangledown^4 u$ with $b_1 > 0$. As the amplitude grows, the nonlinear term $a_2(\bigtriangledown u)^2$ limits the growth of the amplitude by transferring the energy to smaller spatial scales, where eventually the dissipation $g_1 \bigtriangledown^6 u$ prevails. The KS and Nikolaevskii equations have been widely studied by many authors, see for example (Kudryashov, 1990; Armaou and Christofides, 2000; Fujisaka et al., 2003; Tanaka, 2005; Hidaka et al., 2006).

2.8 Nonlinear excitation in the phase equation

Strunin (1999) showed that a truncation of the phase equation with nonlinear excitation is possible in principle. He phenomenologically constructed the nonlinearly excited phase (NEP) equation modelling two types of reaction fronts–the solid flame front and detonation wave–under the conditions close to the combustion limit (where the combustion is on the brink of decay),

$$\partial_t u = \partial_x^6 u - \partial_x \left(\partial_x u\right)^3 + \left(\partial_x u\right)^4 \,, \tag{2.39}$$

where $u(x,t)$ stands for the position of the front subject to periodic boundary conditions. The front is considered to be a surface (line in 1D case) separating cold fresh

mixture from hot reaction products. The model contains the nonlinear excitation term, $-\partial_x \left(\partial_x u\right)^3$, linear dissipation term, $\partial_x^6 u$, and non-linear term, $\left(\partial_x u\right)^4$, transferring the energy from the excitation to dissipation.

The derivative $w = \partial_x u$ apparently obeys the equation

$$\partial_t w = \partial_x^6 w - \partial_x^2 \left(w^3\right) + \partial_x \left(w^4\right). \tag{2.40}$$

See that Eq. (2.40) is a one-dimensional version of a truncation of the general Eq. (2.35) based on nonlinear excitation. The Eq. (2.39) was solved numerically, using Galerkin method, under periodic conditions in space. A settled regime was obtained, in which a kink-shaped wave moves along a spiral trajectory on the surface of the cylinder as shown in Fig. 2.2a. In terms of the derivative, w, as illustrated by Fig. 2.2b, the solution has the form of a train of pulses. They propagate with unique speed and amplitude, both controlled by the dynamic equation, and not the initial condition.

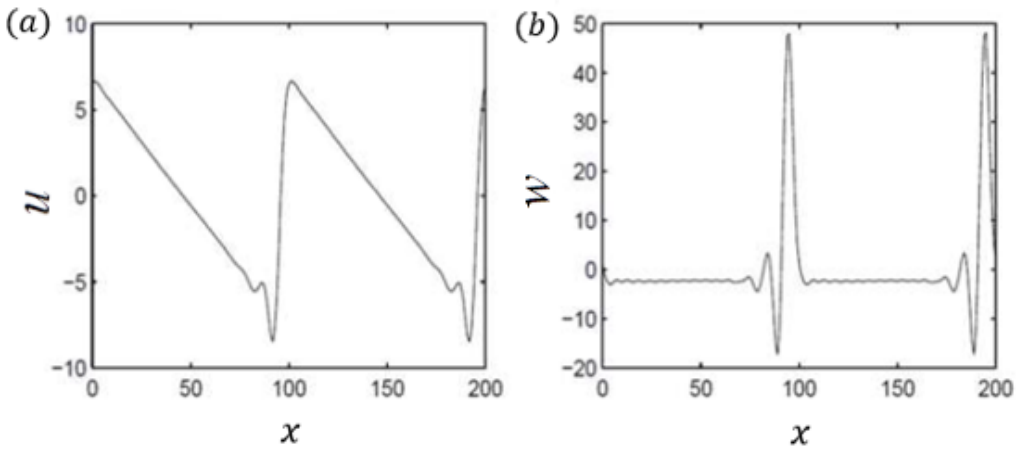

Figure 2.2: A train of kink-shaped (a), and pulse-shaped (b) auto-waves. The u-wave moves upward and to the left; the w-wave moves horizontally to the left (Strunin, 1999).

Also, other truncations of the phase equation (2.35) have been analysed by Strunin

(2003), in which the balance occurs between a nonlinear source and a higher-order nonlinear stabilizing term. More recently, Strunin (2009*b*) derived the nonlinearly excited phase equation (2.39) from the complex Ginzburg-Landau (CGL) equation with nonlocal coupling (Tanaka and Kuramoto, 2003). He also formulated (Strunin, 2009*a*) an equation structurally similar to (2.40) for the fluid flow between elastic walls simulating an artificial artery with active walls, which is the focus of this study.

2.9 Scaling for the phase equations

Table 2.1 summarises the truncations of the general phase equation (2.35) showing important signs of the coefficients and their order of smallness in small parameter ε, which ensures slow variation of u in space and time.

Table 2.1: Hierarchy of truncations of the phase equations (2.35)
(Strunin, 2009*b*)

a_1	a_2	b_1	b_2	b_3	b_4	b_5	g_1	Truncation
$+1$	1	1	1	1	1	1	1	Diffusion Eq.
excitation: $-\varepsilon$	1	-1	1	1	1	1	1	KS Eq.
$+\varepsilon^2$	1	excitation: ε	1	1	1	1	$+1$	Nikolaevskii Eq.
$\mathrm{o}(\varepsilon^6)$	$\mathrm{o}(\varepsilon^5)$	$\mathrm{o}(\varepsilon^3)$	$\mathrm{o}(\varepsilon^2)$	$\mathrm{o}(\varepsilon^2)$	excitation: $-\varepsilon$	1	$+1$	Eq. (2.35)

The characteristic scale of the phase variations are denoted by $U > 0$ and the length scale by $L > 0$. So, the balancing equation terms in absolute value can be evaluated as follows: for KS equation (2.37), the balance $\varepsilon U/L^2 \sim U^2/L^2 \sim U/L^4$ gives

$$U \sim \varepsilon, \quad L \sim \frac{1}{\sqrt{\varepsilon}}\,. \tag{2.41}$$

The time scale is determined from $U/T \sim \varepsilon U/L^2$,

$$T \sim L^2/\varepsilon \sim 1/\varepsilon^2\,. \tag{2.42}$$

Hence, from (2.41) and (2.42) the scaling relations are defined as

$$u = \varepsilon u_1(r_1, t_1)\,, \quad r_1 = \sqrt{\varepsilon} r\,, \quad t_1 = \varepsilon^2 t\,.$$

For the Nikolaevskii equation (2.38) different scaling takes place as follows: the balance $\varepsilon^2 U/L^2 \sim \varepsilon U/L^4 \sim U/L^6 \sim U^2/L^2$ gives

$$U \sim \varepsilon^2\,, \quad L \sim 1/\sqrt{\varepsilon}$$

and, from $U/T \sim \varepsilon^2 U/L^2 \sim \varepsilon^5$,

$$T \sim U/\varepsilon^5 \sim 1/\varepsilon^3\,.$$

Thus, the scaling relations are

$$u = \varepsilon^2 u_1(r_1, t_1)\,, \quad r_1 = \sqrt{\varepsilon} r\,, \quad t_1 = \varepsilon^3 t\,.$$

For the nonlinearly excited (NEP) equation (2.39),

$$\nabla^2 u(\nabla u)^2 \sim U^3/L^4\,, \quad (\nabla u)^4 \sim U^4/L^4 \quad \text{and} \quad \nabla^6 u \sim U/L^6\,.$$

The balance between the three terms of (2.39),

$$\varepsilon U^3/L^4 \sim U^4/L^4 \sim U/L^6\,,$$

gives

$$U \sim \varepsilon, \quad L \sim (1/\varepsilon)^{3/2}\,.$$

We define the time scale from $u/T \sim u^4/L^4 \sim \varepsilon^{10}$,

$$T \sim 1/\varepsilon^9\,.$$

Therefore, the scaling relations is

$$u = \varepsilon u_1(r_1, t_1)\,, \quad r_1 = \varepsilon^{3/2} r\,, \quad t_1 = \varepsilon^9 t\,.$$

2.10 Concluding Remarks

The chapter reviewed the models of fluid pulses through the channel with active elastic walls. Firstly, we reviewed the model of Roberts (1994) which is relevant to wide channels where inertia dominates over viscosity. Then we analysed the model of Strunin (2009*a*) which is designed for narrow channels where viscosity dominates over inertia. This is followed by the literature review of the phase equations in reaction diffusion systems. These equations are similar to the model of Strunin (2009*a*). Two kinds of the phase equations are considered: with linear and non-linear excitation.

Chapter 3

A proposed numerical approach based on 1D-IRBFN method and Picard iterations

3.1 Introduction

This chapter presents a brief overview of the numerical method used throughout the present study. We apply the 1D-IRBFN method in conjunction with the Picard iteration (PI) and one-step Picard iteration (PI1) schemes to solve time-dependent nonlinear partial differential equations. Firstly, we study the performance of the numerical methods through solving the one-dimensional nonlinear Burgers' equation of the form:

$$\frac{\partial u}{\partial t} + u\frac{\partial u}{\partial x} = \frac{1}{Re}\frac{\partial^2 u}{\partial x^2}\,, \quad 0 \le x \le 1\,, \quad t \ge 0\,, \tag{3.1}$$

where $Re > 0$ is the Reynolds number, x and t are space and time parameters, respectively and u is the velocity. Eq.(3.1) is subject to Dirichlet boundary conditions. This equation has been used as a test example to verify numerical methods, because the exact solution is available. The accuracy of the numerical solution is measured

by using the error norm (Ne) as defined by Eq. (3.27).

3.2 The methodology

Many scientific and engineering problems are governed by different types of partial differential equations (PDEs). In general, nonlinear PDEs are hard to be solved analytically, and hence need to be solved numerically in order to study the system's behavior. So far, many numerical methods have been developed for the solution of PDEs, such as finite element method (FEM), finite difference method (FDM), finite volume method (FVM) and others. More recently, the radial basis function (RBF) methods have proved to be a powerful numerical tool to solve PDEs (Dehghan and Shokri, 2007; Uddin et al., 2009; Haq et al., 2010, and references therein). Radial-basis-function networks (RBFNs) have been one of the most active research areas in numerical analysis. It has been proved that RBFNs have the capability of universal approximation (Haykin, 1999). The spectral convergence rate of the Multiquadric (MQ) RBF interpolation was proved by Madych and Nelson (1992).

Kansa (1990*a*,*b*) proposed a collocation scheme based on MQ-RBF for the numerical solution of PDEs. Their numerical results showed that the MQ scheme is more efficient than finite difference schemes which require many operations to achieve the same degree of accuracy. The application of MQ-RBFNs for the solution of PDEs has attracted a great deal of attention from researchers over the last decade (see for example, Fasshauer, 1997; Zerroukat et al., 1998; Mai-Duy and Tran-Cong, 2001*b*; Fedoseyev et al., 2002; Power and Barraco, 2002; Larsson and Fornberg, 2003; Šarler et al., 2004). These methods together with differential equations have been significantly succeeded in solving diverse scientific and engineering problems. It should be indicated that the RBF width strongly affects the performance of the RBF scheme. To date, there is a lack of mathematical theory for finding appropriate values of the RBF width. In practice, the RBF width is chosen either by empirical approaches or

by optimization techniques (see for example Zerroukat et al., 1998; Kansa and Hon, 2000). The latter are expensive, especially for non-linear problems. Generally, the RBF scheme is more accurate, but less stable with increasing RBF-width.

There are two basic approaches to construct the RBF approximations, namely differentiated RBFNs (DRBFNs) (Kansa, 1990*a*) and integrated RBFNs (IRBFNs) (Mai-Duy and Tran-Cong, 2001*a*, 2003). In the DRBFN method, a function is first represented by an RBFN which is then differentiated to obtain approximate expressions for its derivative functions. Although the method has the ability to describe continuous functions with a prescribed degree of accuracy, the process of differentiation magnifies any errors that might arise from approximating the original function and thus result in inaccurate derivatives. For the IRBFN method, on the other hand, the highest-order derivatives in the PDE are first decomposed into RBFs, and lower-order derivatives and the function itself are then obtained through integration. The latter was developed with the aim of avoiding the problem of reduced convergence rate caused by differentiation. Through numerical experiments (e.g. Mai-Duy and Tran-Cong, 2001*a*, 2003), it was shown that IRBFN collocation methods are more accurate than DRBFN ones for the approximation of a function and its derivatives and for the solution of PDEs. In (Mai-Duy and Tran-Cong, 2001*b*, 2003; Sarra, 2006; Ngo-Cong et al., 2012*a*; Tien et al., 2015*a*,*b*) the authors demonstrated that the IRBFN method has the ability to yield a faster converging solution, because the integration is a smoothing operation and integrated basis functions are of higher orders.

Mai-Duy and Tanner (2007) presented a one-dimensional integrated radial basis function network (1D-IRBFN) collocation method for solving PDEs (see Appendix A). Along grid lines, 1D-IRBFN are constructed to satisfy the governing DEs together with boundary conditions in an exact manner. This method is much more efficient than the original IRBFN method reported by Mai-Duy and Tran-Cong (2001*a*). The 1D-IRBFN method has been successfully used for solving a variety of problems such

as viscous and viscoelastic flows (Ho-Minh et al., 2012; Tran et al., 2012), structural analysis (Ngo-Cong et al., 2011), and turbulent flows in open channels (Mohammed et al., 2014). It was demonstrated that the 1D-IRBFN method has advantages over other numerical methods, for example finite difference and finite element methods, in terms of accuracy, faster approach and efficiency (Mai-Duy and Tran-Cong, 2001*a*).

In the present study, we develop a numerical tool based on the 1D-IRBFN method in combination with the Picard iteration schemes for solving time-dependent non-linear PDEs. Numerical experiments are conducted on a computer with an Intel i7, 3.60 GHz processor and 16 GB RAM using Matlab-R2017b software.

3.3 One-dimensional integrated radial basis function networks (1D-IRBFN)

In this section, we extend the 1D-IRBFN method presented in (Mai-Duy and Tanner, 2007; Mai-Duy and Tran-Cong, 2001*a*) to compute function derivatives up to 6th-order. Consider an x-grid line, with N grid nodes. Along this lines, the variation of the function u is represented in the IRBF form. The basic idea of the integral RBF scheme (Mai-Duy and Tran-Cong, 2003) is to decompose the highest p-th order derivative of u into RBFs; the lower-order derivatives and the original function itself

are then obtained through integration as follows

$$\frac{\partial^p u(x)}{\partial x^p} = \sum_{i=1}^{N} w_i G_i(x) = \sum_{i=1}^{N} w_i H_p^{(i)}(x)\,, \tag{3.2}$$

$$\frac{\partial^{p-1} u(x)}{\partial x^{p-1}} = \sum_{i=1}^{N} w_i H_{p-1}^{(i)}(x) + c_1\,, \tag{3.3}$$

$$\frac{\partial^{p-2} u(x)}{\partial x^{p-2}} = \sum_{i=1}^{N} w_i H_{p-2}^{(i)}(x) + c_1 x + c_2\,, \tag{3.4}$$

$\cdots\ \cdots\ \cdots$

$$\frac{\partial u(x)}{\partial x} = \sum_{i=1}^{N} w_i H_1^{(i)}(x) + c_1 \frac{x^{p-2}}{(p-2)!} + c_2 \frac{x^{p-3}}{(p-3)!} + \cdots + c_{p-2} x + c_{p-1}\,, \tag{3.5}$$

$$u(x,t) = \sum_{i=1}^{N} w_i(t) H_0^{(i)}(x) + c_1 \frac{x^{p-1}}{(p-1)!} + c_2 \frac{x^{p-2}}{(p-2)!} + \cdots + c_{p-2} \frac{x^2}{2} + c_{p-1} x + c_p\,, \tag{3.6}$$

where $\{w_i(t)\}_{i=1}^{N}$ are RBF weights to be determined; $\{G_i(x)\}_{i=1}^{N} = \{H_p^{(i)}(x)\}_{i=1}^{N}$ are known RBFs, e.g., for the case of multiquadrics (MQ)

$$G_i(x) = \sqrt{(x - c_i)^2 + {a_i}^2}\,,$$

where c_i and a_i are the centre and width of the i^{th} MQ-RBF, respectively. The set of centres is chosen to be the same as the set of collocation points, and the RBF width is determined as $a_i = bd_i$, $b > 0$ is a factor (presently $b = 1$), and d_i is the distance from the i-th centre to the nearest; $H_{p-1}^{(i)}(x) = \int H_p^{(i)}(x)dx$; $H_{p-2}^{(i)}(x) = \int H_{p-1}^{(i)}(x)dx$; $\ldots$; $H_1^{(i)}(x) = \int H_2^{(i)}(x)dx$; $H_0^{(i)}(x) = \int H_1^{(i)}(x)dx$; and $\{c_i\}_{i=1}^{p}$ the set of constants arising from the integration process.

After discretization, equations (3.2)–(3.6) can be written in a compact form as

$$\widehat{\frac{\partial^p u}{\partial x^p}} = \widehat{H_p^{(i)}}\widehat{\alpha} \tag{3.7}$$

$$\widehat{\frac{\partial^{p-1} u}{\partial x^{p-1}}} = \widehat{H_{p-1}^{(i)}}\widehat{\alpha} \tag{3.8}$$

$$\cdots\cdots\cdots$$

$$\widehat{\frac{\partial u}{\partial x}} = \widehat{H_1^{(i)}}\widehat{\alpha} \tag{3.9}$$

$$\widehat{u} = \widehat{H_0^{(i)}}\widehat{\alpha}\,, \tag{3.10}$$

where

$$\widehat{H_p^{(i)}} = \begin{bmatrix} H_p^{(1)}(x_1) & H_p^{(2)}(x_1) & \dots & H_p^{(N)}(x_1) & 0 & 0 & \dots & 0 & 0 \\ H_p^{(1)}(x_p) & H_p^{(2)}(x_2) & \dots & H_p^{(N)}(x_2) & 0 & 0 & \dots & 0 & 0 \\ \dots & \dots & \dots & \dots & \dots & \dots & \dots & \dots & \dots \\ H_p^{(1)}(x_N) & H_p^{(2)}(x_N) & \dots & H_p^{(N)}(x_N) & 0 & 0 & \dots & 0 & 0 \end{bmatrix},$$

$$\widehat{H_{p-1}^{(i)}} = \begin{bmatrix} H_{p-1}^{(1)}(x_1) & H_{p-1}^{(2)}(x_1) & \dots & H_{p-1}^{(N)}(x_1) & 1 & 0 & \dots & 0 & 0 \\ H_{p-1}^{(1)}(x_2) & H_{p-1}^{(2)}(x_2) & \dots & H_{p-1}^{(N)}(x_2) & 1 & 0 & \dots & 0 & 0 \\ \dots & \dots & \dots & \dots & \dots & \dots & \dots & \dots & \dots \\ H_{p-1}^{(1)}(x_N) & H_{p-1}^{(2)}(x_N) & \dots & H_{p-1}^{(N)}(x_N) & 1 & 0 & \dots & 0 & 0 \end{bmatrix},$$

$\vdots$

$$\widehat{H_0^{(i)}} = \begin{bmatrix} H_0^{(1)}(x_1) & H_0^{(2)}(x_1) & \dots & H_0^{(N)}(x_1) & x_1^{p-1}/(p-1)! & x_1^{p-2}/(p-2)! & \dots & x_1 & 1 \\ H_0^{(1)}(x_2) & H_0^{(2)}(x_2) & \dots & H_0^{(N)}(x_2) & x_2^{p-1}/(p-1)! & x_2^{p-2}/(p-2)! & \dots & x_2 & 1 \\ \dots & \dots & \dots & \dots & \dots & \dots & \dots & \dots & \dots \\ H_0^{(1)}(x_N) & H_0^{(2)}(x_N) & \dots & H_0^{(N)}(x_N) & x_N^{p-1}/(p-1)! & x_N^{p-2}/(p-2)! & \dots & x_N & 1 \end{bmatrix}, \tag{3.11}$$

where $\{x_i\}_{i=1}^N$ is the set of nodal points, $\widehat{u} = (u_1, u_2, u_3, ..., u_N)^T$, $\widehat{w} = (w_1, w_2, w_3, ..., w_N)^T$ and $\widehat{c} = (c_1, c_2, c_3, \dots, c_p)^T$. We denote $\widehat{\alpha} = (w_1, w_2, w_3, ..., w_N, c_1, c_2, \dots, c_p)^T$.

3.4 Time integration schemes

The one-dimensional nonlinear Burgers' equation is discretized with respect to both time and space variables. Firstly, the time interval $[0, T]$ is partitioned into N_T subintervals $[t^{(n)}, t^{(n+1)}]$ of length $\Delta t = T/N_T$ with $t^{(0)} = 1$ and $t^{(N_T+1)} = T$. The temporal discretization is then accomplished by a time-stepping scheme, followed by the spatial discretization based on the IRBFN method. Among many possible time-stepping schemes, the standard θ-scheme (Quarteroni and Valli, 2008), $0 \leq \theta \leq 1$ is used in this work.

The extreme cases $\theta = 0$ and $\theta = 1$ correspond to the well-known forward (fully explicit) and backward (fully implicit) Euler schemes, respectively. The scheme with $\theta = 1/2$ is known as the (semi-implicit) Crank-Nicolson method which is second-order accurate.

$$\frac{u^{(n+1)} - u^{(n)}}{\Delta t} = \theta U^{(n+1)} + (1-\theta) U^{(n)} \,. \tag{3.12}$$

Applying the θ- scheme with $\theta = 1/2$ to Eq. (3.1) gives

$$\frac{u^{(n+1)} - u^{(n)}}{\Delta t} = \frac{1}{2} U^{(n+1)} + \frac{1}{2} U^{(n)} \tag{3.13}$$

$$\frac{u^{(n+1)} - u^{(n)}}{\Delta t} = \frac{1}{2} \left\{ \frac{1}{Re} \frac{\partial^2 u}{\partial x^2} - u \frac{\partial u}{\partial x} \right\}^{(n+1)} + \frac{1}{2} \left\{ \frac{1}{Re} \frac{\partial^2 u}{\partial x^2} - u \frac{\partial u}{\partial x} \right\}^{(n)} \tag{3.14}$$

or

$$\frac{u^{(n+1)}}{\Delta t} - \frac{1}{2} \left\{ \frac{1}{Re} \frac{\partial^2 u}{\partial x^2} - u \frac{\partial u}{\partial x} \right\}^{(n+1)} = \frac{u^{(n)}}{\Delta t} + \frac{1}{2} \left\{ \frac{1}{Re} \frac{\partial^2 u}{\partial x^2} - u \frac{\partial u}{\partial x} \right\}^{(n)} , \tag{3.15}$$

where $\triangle t = t^{(n+1)} - t^{(n)}$ is the physical time step; and the superscripts (n) and $(n+1)$ denote the previous and current physical time levels, respectively. Note that $\left\{ \frac{1}{Re} \frac{\partial^2 u}{\partial x^2} - u \frac{\partial u}{\partial x} \right\}^{(n+1)}$ in Eq. (3.15) consists of nonlinear terms. In order to linearize these nonlinear term, we add a pseudo term into Eq. (3.15) as follows (Jameson, 1991; Ngo-Cong et al., 2012*b*)

$$\frac{\partial u}{\partial \tau} + \frac{u^{(n+1)}}{\Delta t} - \frac{1}{2} \left\{ \frac{1}{Re} \frac{\partial^2 u}{\partial x^2} - u \frac{\partial u}{\partial x} \right\}^{(n+1)} = \frac{u^{(n)}}{\Delta t} + \frac{1}{2} \left\{ \frac{1}{Re} \frac{\partial^2 u}{\partial x^2} - u \frac{\partial u}{\partial x} \right\}^{(n)} \tag{3.16}$$

where τ is the pseudo time. Linearization of Eq. (3.16) using the Picard iteration method (Islam et al., 2017; Paniconi and Putti, 1994) yields

$$\frac{u^{(n+1,m+1)}-u^{(n+1,m)}}{\Delta\tau}+\frac{u^{(n+1,m+1)}}{\Delta t}-\frac{1}{2}\left\{\frac{1}{Re}\frac{\partial^2 u^{(n+1,m+1)}}{\partial x^2}-u^{(n+1,m)}\frac{\partial u^{(n+1,m+1)}}{\partial x}\right\}$$
$$=\frac{u^{(n)}}{\Delta t}+\frac{1}{2}\left\{\frac{1}{Re}\frac{\partial^2 u^{(n)}}{\partial x^2}-u^{(n)}\frac{\partial u^{(n)}}{\partial x}\right\} \tag{3.17}$$

or,

$$\frac{u^{(n+1,m+1)}}{\Delta\tau}+\frac{u^{(n+1,m+1)}}{\Delta t}-\frac{1}{2}\left\{\frac{1}{Re}\frac{\partial^2 u^{(n+1,m+1)}}{\partial x^2}-u^{(n+1,m)}\frac{\partial u^{(n+1,m+1)}}{\partial x}\right\}$$
$$=\frac{u^{(n+1,m)}}{\Delta\tau}+\frac{u^{(n)}}{\Delta t}+\frac{1}{2}\left\{\frac{1}{Re}\frac{\partial^2 u^{(n)}}{\partial x^2}-u^{(n)}\frac{\partial u^{(n)}}{\partial x}\right\} \tag{3.18}$$

where $\triangle\tau=\tau^{(n+1)}-\tau^{(n)}$ is the pseudo time step; and the superscripts (m) and $(m+1)$ denote the previous and current pseudo time levels, respectively. Eq. (3.18) is then discretized in space using the 1D-IRBFN method. Making use of Eqs. (3.7)–(3.10), Eq. (3.18) becomes

$$\left[\frac{\widehat{H}_0}{\Delta\tau}+\frac{\widehat{H}_0}{\Delta t}-\frac{1}{2Re}\widehat{H}_2+\frac{1}{2}\widehat{H}_0\widehat{\alpha}^{(n+1,m)}\widehat{H}_1\right]\widehat{\alpha}^{(n+1,m+1)}$$
$$=\frac{\widehat{H}_0}{\Delta\tau}\widehat{\alpha}^{(n+1,m)}+\left[\frac{\widehat{H}_0}{\Delta t}+\frac{1}{2Re}\widehat{H}_2-\frac{1}{2}\widehat{H}_0\widehat{\alpha}^{(n)}\widehat{H}_1\right]\widehat{\alpha}^{(n)} \tag{3.19}$$

For simplicity, the above equation can be written as,

$$E_1\widehat{\alpha}^{(n+1,m+1)}=\mathrm{RHS}_1^{(n+1,m)} \tag{3.20}$$

and the boundary conditions as

$$E_2\widehat{\alpha}^{(n+1,m+1)}=\mathrm{RHS}_2\,. \tag{3.21}$$

The Picard iteration is performed at every physical time level $(n+1)$. A stopping criteria for the Picard iteration is as follows:

$$CM=\frac{\sqrt{\sum_{i=1}^{N}\left(u_i^{(n+1,m+1)}-u_i^{(n+1,m)}\right)^2}}{\sqrt{\sum_{i=1}^{N}\left(u_i^{(n+1,m+1)}\right)^2}}<TOL \tag{3.22}$$

where TOL is a given tolerance and presently set to be 10^{-5}; and N the number of interior points. If the stopping criteria is fulfilled, we specify $u^{(n)} = u^{(n+1,m+1)}$, then advance the physical time t. The system of equations (3.20)–(3.21) is solved simultaneously at each time step for $\widehat{\alpha}^{(n+1,m+1)}$ until the prescribed time T is reached. Instead of iterating until the stopping criteria is achieved, one may iterate a specific number of pseudo-time steps. One-step Picard iteration corresponds to using the solution at the previous time level to linearize nonlinear terms. The linearization of Eq. (3.15) using the one-step Picard iteration method yields

$$\frac{u^{(n+1)}}{\Delta t} - \frac{1}{2}\left\{\frac{1}{Re}\frac{\partial^2 u^{(n+1)}}{\partial x^2} - u^{(n)}\frac{\partial u^{(n+1)}}{\partial x}\right\} = \frac{u^{(n)}}{\Delta t} + \frac{1}{2}\left\{\frac{1}{Re}\frac{\partial^2 u^{(n)}}{\partial x^2} - u^{(n)}\frac{\partial u^{(n)}}{\partial x}\right\} \tag{3.23}$$

Then Eq. (3.23) is discretized in space based on the 1D-IRBFN method.

$$\left[\frac{\widehat{H}_0}{\Delta t} - \frac{1}{2Re}\widehat{H}_2 + \frac{1}{2}\widehat{H}_0\widehat{\alpha}^{(n)}\widehat{H}_1\right]\widehat{\alpha}^{(n+1)} = \left[\frac{\widehat{H}_0}{\Delta t} + \frac{1}{2Re}\widehat{H}_2 - \frac{1}{2}\widehat{H}_0\widehat{\alpha}^{(n)}\widehat{H}_1\right]\widehat{\alpha}^{(n)}, \tag{3.24}$$

For simplicity, the above equation can be written as,

$$E_1\widehat{\alpha}^{(n+1)} = \mathrm{RHS}_1 \tag{3.25}$$

and the boundary conditions as

$$E_2\widehat{\alpha}^{(n+1)} = \mathrm{RHS}_2\,. \tag{3.26}$$

The system of equations (3.25)–(3.26) is solved simultaneously at each physical time step for $\widehat{\alpha}^{(n+1)}$ until the prescribed time T is reached.

3.5 Numerical results and discussion

The two test problems are studied in order to demonstrate the numerical accuracy of the 1D-IRBFN method. To measure the accuracy of this method, we compute the

error between the numerical obtained solution $u(x,t)$ and the exact solution $u_e(x,t)$ under the following relative error norm:

$$N_e = \sqrt{\frac{\sum_{i=1}^{N} \left[u(x_i,t) - u_e(x_i,t)\right]^2}{\sum_{i=1}^{N} u_e^2(x_i,t)}}\,, \tag{3.27}$$

where $u(x_i,t)$ and $u_e(x_i,t)$ are the numerical and the exact solution at the i-th node, respectively; N the number of nodes over the whole domain. As it is known that the smaller the relative error, the more accurate the numerical solution will be. Another important measure is the convergence rate of the solution with respect to the refinement of spatial discretization, defined by

$$N_e(h) \approx \gamma h^{\lambda} = O(h^{\lambda})\,, \tag{3.28}$$

in which γ and λ are exponential model parameters and h is the grid spacing. We solved one simple ordinary differential equation to study the convergence behaviour of the 1D-IRBFN method and FDM with a central difference scheme (Appendix B).

3.5.1 Analytical solution 1:

The analytical solution of the Burgers equation (3.1) has the following form (Hosseini and Hashemi, 2011; Xu et al., 2011)

$$u_e(x,t) = \frac{\left[\alpha_0 + \mu_0 + (\mu_0 - \alpha_0)\, exp(\eta)\right]}{1 + exp(\eta)}\,, \quad 0 \le x \le 1\,,\, t \ge 0\,, \tag{3.29}$$

where $\eta = \alpha Re\,(x - \mu_0 t - \beta_0)\,$, $\alpha_0 = 0.4$, $\beta_0 = 0.125$, $\mu_0 = 0.6$, $Re = 100$. The wave of this solution is moving to the right with speed μ. The initial condition is found from (3.29) when $t = 0$ and the boundary conditions are given by $u(0,t) = 1, u(1,t) = 0.2$ for $t > 0$. Figs. 3.1 and 3.2 show an excellent agreement between the analytical solution and 1D-IRBFN results for both the PI and PI1 schemes at different times, using a grid of 100, $\Delta t = 10^{-3}$, $\Delta\tau = 10^{-3}$ and $TOL = 10^{-5}$.

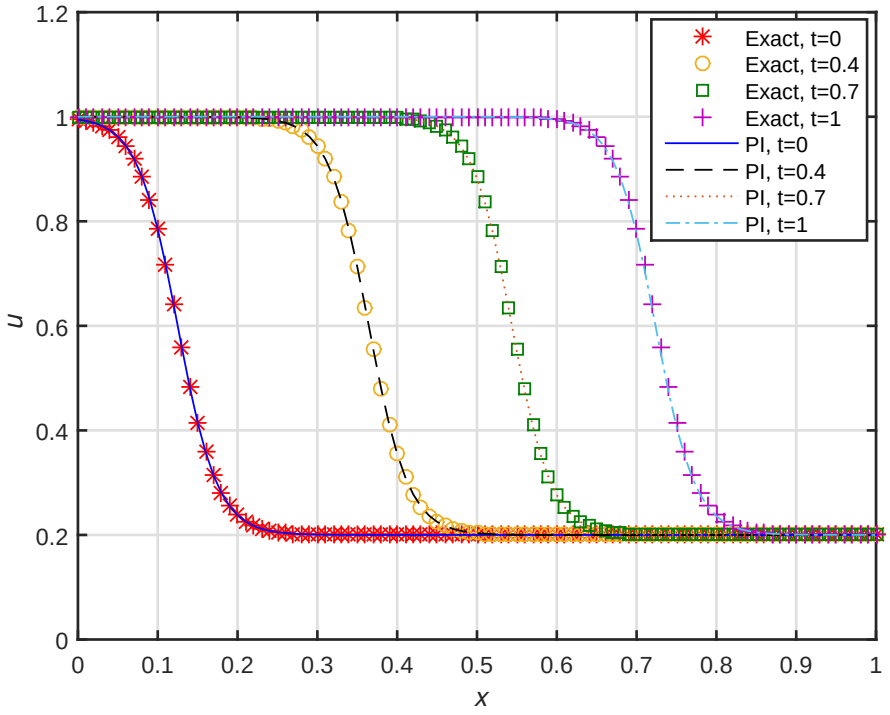

Figure 3.1: Comparison of the numerical solutions of the Burgers' equation (3.1) using PI scheme with exact solution (3.29) at different times, for $\Delta t = 10^{-3}$, $\Delta\tau = 10^{-3}$, $TOL = 10^{-5}$ and a grid of 100 .

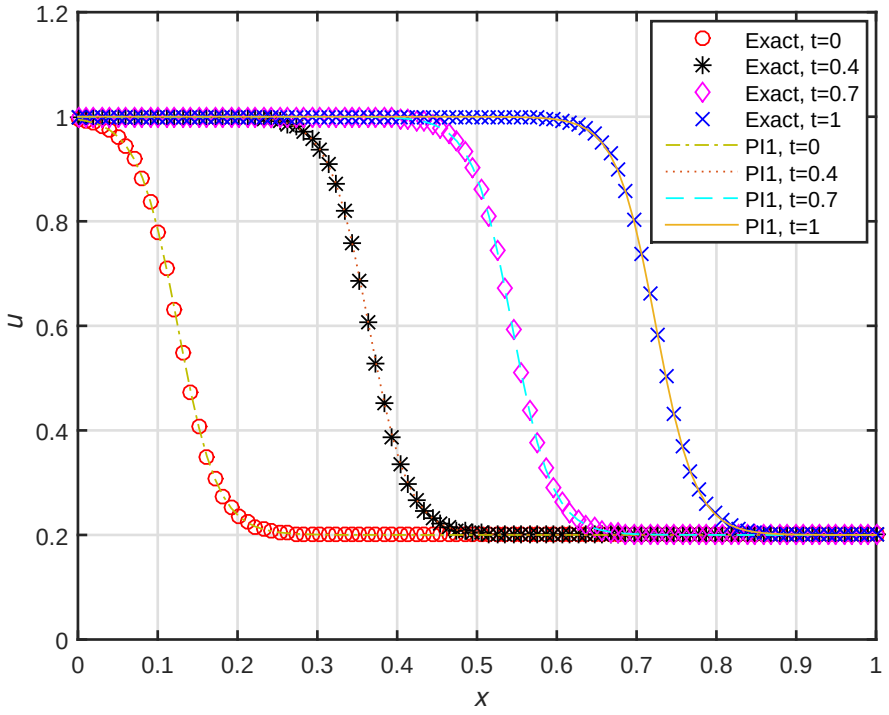

Figure 3.2: Comparison of the numerical solutions of the Burgers' equation (3.1) using PI1 scheme with exact solution (3.29) at different times for $\Delta t = 10^{-3}$ and a grid of 100 .

Table 3.1 gives the time step convergence study of the relative error norm (Ne) for different time integration schemes at a grid of 100. The numerical results show that the relative error norm reduces with decreasing time step Δt . The grid convergence study of the relative error norm (Ne) for different time integration schemes are given in Table 3.2. In our computations, we use the same time step $\Delta t = 0.001$ for PI1 and PI. It can be seen that the errors are almost the same as the grid number increases which indicates that the major numerical error comes from the temporal discretisation, not from the 1D-IRBFN spatial approximation.

Table 3.1: Burgers equations, with the analytic solution (3.29): time step convergence study of the relative error norm (Ne) for different time integration schemes at $t = 1$, $\Delta\tau = 10^{-3}$, $TOL = 10^{-5}$ and a grid size of 100 .

Δt	Ne	
	PI1	PI
5.00E-03	5.30E-03	4.14E-03
2.00E-03	1.91E-03	1.60E-03
1.00E-03	8.10E-04	1.42E-03
5.00e-04	5.60E-04	1.27E-03
2.00E-04	4.28E-04	1.12E-03
1.00E-04	3.95E-04	3.36E-04

Table 3.2: Burgers equations, with the analytic solution (3.29): grid convergence study of the relative error norm (Ne) for different time integration schemes, at $t = 1$, $\Delta\tau = 10^{-3}$, $TOL = 10^{-5}$ and time step 10^{-3} .

Grid	Ne	
	PI1	PI
51	8.07E-04	1.43E-03
101	8.10E-04	1.42E-03
151	8.11E-04	1.42E-03
201	8.12E-04	1.42E-03
251	8.12E-04	1.42E-03
301	8.12E-04	1.42E-03
351	8.12E-04	1.42E-03

For scheme PI, the further comparison of the numerical results is made with the exact ones (3.29) for different values of TOL at $t = 1$, $\Delta t = 10^{-3}$, $\Delta\tau = 10^{-3}$ and a

grid of 100. It is also clear from Fig. 3.3, the relative error norm (Ne) reduces with decreasing TOL. This indicates that the PI scheme yields more accurate solutions as TOL reduces from 5×10^{-3} to 10^{-5}, with the smallest error of 1.42×10^{-3} at $TOL = 10^{-5}$.

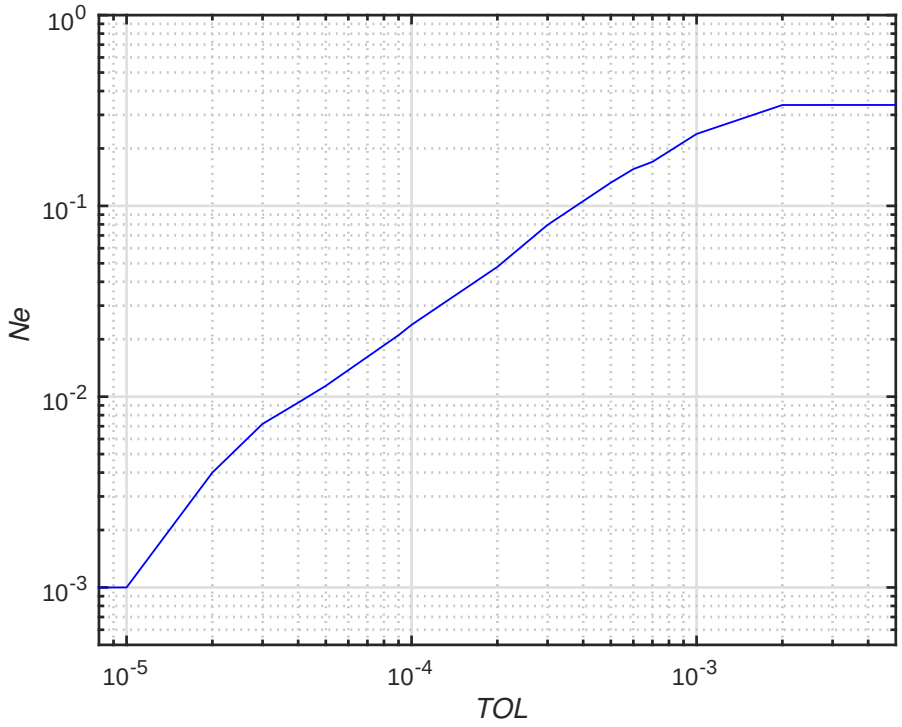

Figure 3.3: Burgers equation with the analytic solution (3.29): The relation between Ne and TOL at $t = 1$, $\Delta t = 10^{-3}$, $\Delta\tau = 10^{-3}$ and a grid of 100, PI scheme.

3.5.2 Analytical solution 2:

We consider another analytical solution of Burgers equation (Dhawan et al., 2012; Gorgulu et al., 2016) as follows:

$$u_e(x,t) = \frac{(x/t)}{1 + (t/t_0)^{1/2} \exp\left(x^2/4\eta t\right)}, \quad t \geq 1, \quad 0 \leq x \leq 1, \tag{3.30}$$

where $t_0 = \exp(1/8\eta)$. The propagation of the shock is represented with the equation above. The boundary conditions are given by $u(0,t) = 0, u(1,t) = 0$.

In our computation we take $\eta = 1/Re = 0.005$ and $\Delta t = 0.001$. The initial condition is taken at time $t = 1$. Figs. 3.4 and 3.5 show an excellent agreement between the exact solution and 1D-IRBFN results with both the PI and PI1 schemes at different times using a grid of 100, $\Delta t = 10^{-3}$, $\Delta\tau = 5 \times 10^{-3}$ and $TOL = 10^{-5}$.

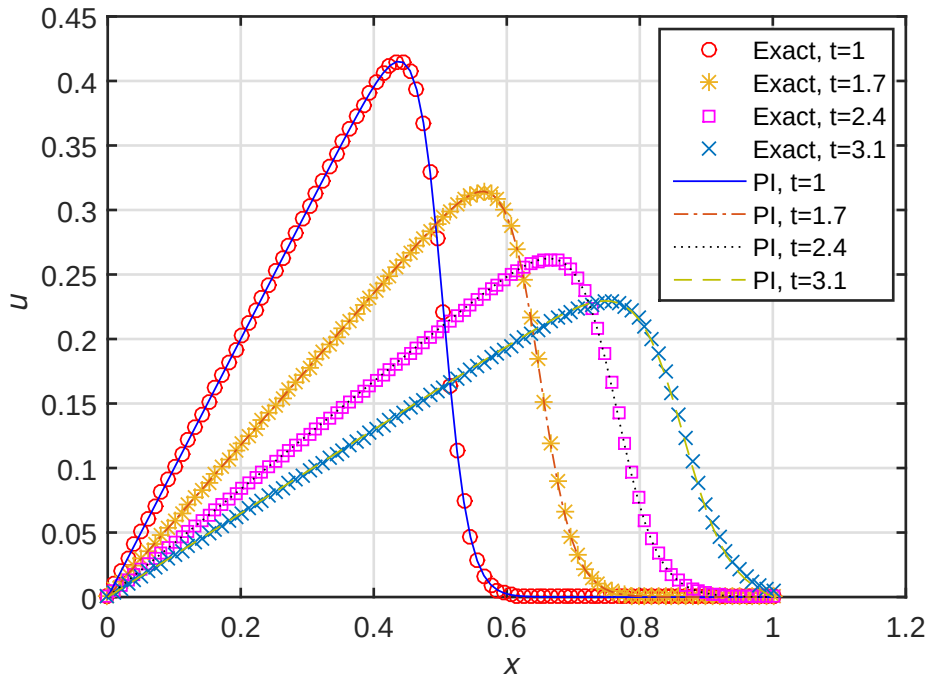

Figure 3.4: The numerical solutions of the Burgers' equation (3.1) using 1D-IRBFN method with PI scheme and the exact solution (3.30) at $t \geq 1$, $\Delta t = 10^{-3}$, $\Delta\tau = 5 \times 10^{-3}$, $TOL = 10^{-5}$ and a grid of 100 .

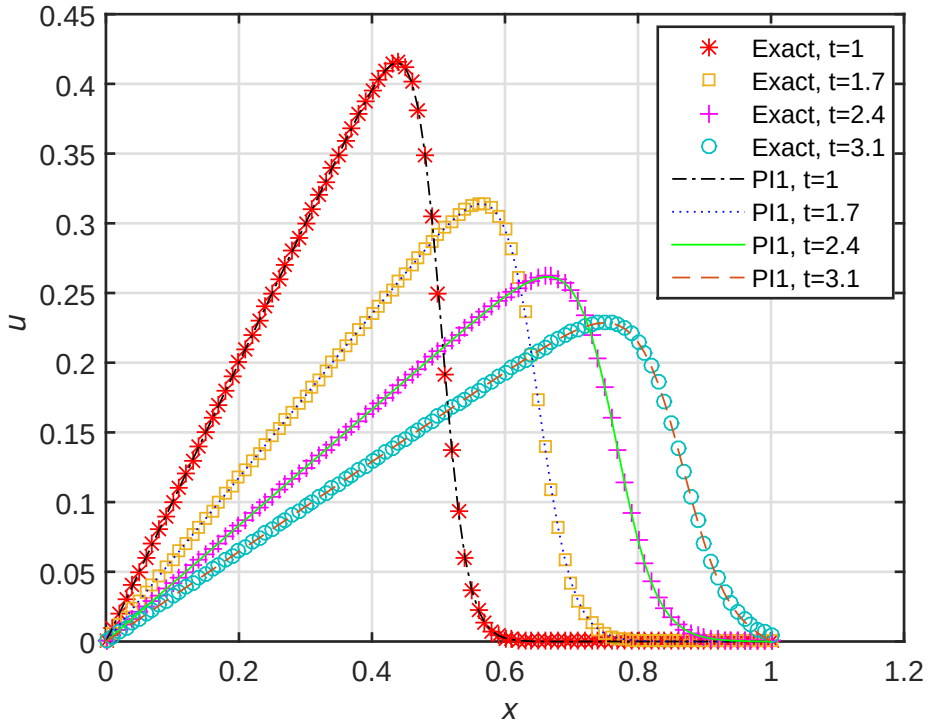

Figure 3.5: The numerical solutions of the Burgers' equation (3.1) using PI1 scheme and exact solution (3.30) at $t \geq 1$, $\Delta t = 10^{-3}$ and a grid of 100 .

In this test problem, we make a comparison between the present method and the FDM with a central difference scheme for spatial discretisation and forward (fully explicit) Euler scheme for temporal discretisation (see Appendix C for the details about FDM). The result comparison at $t = 2$ for several time step sizes and at a grid of 100 are presented in Table 3.3. Grid convergence studies for both methods with the same time step of 0.001 are shown in Table 3.4. It is noted that the 1D-IRBFN method with both PI and PI1 schemes is much more accurate than the FDM and converges faster.

Table 3.3: Burgers equation, with analytical solution (3.30): comparison between two methods at $t = 2$ with different time step sizes, $\Delta\tau = 5 \times 10^{-3}$, $TOL = 10^{-5}$ and using a grid of 100 .

Δt	Ne		
	1D-IRBFN		FDM
	PI1	PI	
5.00E-03	3.60E-03	4.4E-03	5.7E-03
2.00E-03	1.4E-03	1.7E-03	2.3E-03
1.00E-03	7.12E-04	7.85E-04	1.5E-03
5.00e-04	3.56E-04	3.45E-04	1.5E-03
2.00E-04	1.42E-04	3.52E-04	1.6E-03
1.00E-04	7.10E-05	1.19E-04	1.7E-03
5.00E-05	3.54E-05	3.20E-05	1.7E-03

Table 3.4: Burgers equation, with analytical solution (3.30): comparison between two methods at $t = 2$ for several numbers of grids $\Delta t = 10^{-3}$, $\Delta\tau = 5 \times 10^{-3}$ and $TOL = 10^{-5}$.

Grid	Ne		
	1D-IRBFN		FDM
	PI1	PI	
51	7.11E-04	7.85E-04	6.8E-03
101	7.12E-04	7.85E-04	1.5E-03
151	7.12E-04	7.85E-04	1.2E-03
201	7.12E-04	7.85E-04	1.1E-03
251	7.12E-04	7.85E-04	1.1E-03
301	7.12E-04	7.85E-04	1.2E-03

3.6 Concluding Remarks

The chapter demonstrates the accuracy of our proposed numerical approach based on the 1D-IRBFN method in conjunction with the PI and PI1 schemes through two different exact solutions of the Burgers equation. The present method outperforms the FDM with a central difference scheme in conjunction with the forward Euler scheme. The PI scheme produces more accuracy solution when using smaller values of TOL.

Chapter 4

Auto-pulses in a single-channel flow

4.1 Introduction

The main purpose of this chapter is to present numerical solutions of the model of self-propagating fluid pulses (auto-pulses) (Strunin, 2009*a*) through the single channel. This model simulates an artificial artery with *active* walls. Putting aside the technological challenges of construction of such a sophisticated device, we aim to establish theoretical principles of how the artificial walls need to move in order to facilitate a uni-directional fluid flow. As was mentioned in Chapter 2, our analysis is based on the model (Strunin, 2009*a*), which further developed the ideas of Roberts of channels with active walls (Roberts, 1994). While Roberts considered the case of negligible viscous forces compared to inertia, which is relevant to wider channels, we will consider the case when inertia is negligible compared to viscous forces, which is relevant to narrow channels.

For simplicity Strunin (2009*a*) considered a theoretical configuration of the flow contained between unbounded active elastic walls shaped (in the rest state) as planes.

This model is autonomous and based on a nonlinear partial differential equation to describe the displacement of the channel wall with respect to time t and the distance x along the channel. A theoretical plane configuration is adopted for the walls at rest. The model has the form

$$\frac{\partial w}{\partial t} = \frac{D}{3\eta}\frac{\partial}{\partial x}\left[H^3\frac{\partial^5 w}{\partial x^5}\right] - \frac{\alpha}{3\eta}\frac{\partial}{\partial x}\left[H^3\frac{\partial}{\partial x}\left(w^4\right)\right] + \beta\frac{\partial}{\partial x}\left(H^3 w^5\right) , \tag{4.1}$$

where w is the deflection of the wall from the neutral position H_0, so that $H(x,t) = H_0 + w(x,t)$, with H being counted from the middle of the channel (see Fig. 2.1), the coordinate x is directed along the flow, D is the flexural rigidity of the wall, and η is the viscosity. In (4.1), as we have already mentioned, the dissipation is represented by the term, $\partial_x\left[H^3\partial_x^5 w\right]$, and the excitation by the nonlinear term, $-\partial_x\left[H^3\partial_x\left(w^4\right)\right]$. The nonlinear term $\partial_x(H^3w^5)$ plays the role of the "bridge" between those two, directing energy from long-wave to short-wave scales.

Assuming $w << H_0$ and replacing H by $H = H_0 + w \approx H_0$ in Eq. (4.1) we get

$$\frac{\partial w}{\partial t} = \frac{DH_0^3}{3\eta}\frac{\partial^6 w}{\partial x^6} - \frac{\alpha H_0^3}{3\eta}\frac{\partial^2}{\partial x^2}\left(w^4\right) + H_0^3\beta\frac{\partial}{\partial x}\left(w^5\right) . \tag{4.2}$$

Now we non-dimensionalize Eq. (4.2) using some relevant scales to the form

$$\frac{\partial w}{\partial t} = A\frac{\partial^6 w}{\partial x^6} - B\frac{\partial^2}{\partial x^2}\left(w^4\right) + C\frac{\partial}{\partial x}\left(w^5\right) , \tag{4.3}$$

where the coefficients A, B and C are non-dimensional. By re-scaling t, x and w, equation (4.3) can be set to a canonical form where three of the coefficients A, B and C are made units. Therefore, regardless of the coefficient values used in a particular experiment, the shape of the function $w(x,t)$ simultaneously represents the shape of the solution of the canonical form of the equation only in re-scaled coordinates.

As we pointed out in Chapter 2, the model (4.2) should give auto-wave solutions in the form of pulses. In short preliminary paper (Ahmed et al., 2016) we obtained a few pulse regimes by solving the form of (4.2), written with respect to the function $\partial f/\partial x = w$. In this thesis, following Ahmed et al. (2018) we solve numerically equation (4.3) and thoroughly investigate a wide range of pulse regimes. For solving

equation (4.3) we use the One-dimensional Integrated Radial Basis Function Network (1D-IRBFN) method. While the method has been tested successfully before in a number of studies, getting the pulse regime using this method would provide yet another test.

The present chapter is structured as follows. In Section 4.2 we present the numerical method. In Section 4.3 we discuss the numerical results and study multi-pulse solutions. Conclusions are given in Section 5.4.

4.2 Numerical approach

In this section, we apply the 1D-IRBFN method (Ngo-Cong et al., 2015; Ahmed et al., 2016) in conjunction with the Picard iteration (PI) and one-step Picard iteration (PI1) schemes to solve the 6^{th} order partial differential equation (4.3). This 1D-IRBFN method is an extended version of the original 1D-IRBFN method presented in (Mai-Duy and Tran-Cong, 2001*a*; Mai-Duy and Tanner, 2007) for solving 6^{th} partial differential equations (PDEs). In this method highest-order derivative in a differential equation is approximated by radial basis functions and, further, the lower-order derivatives and function itself are then obtained by integration. The purpose of using integration is to avoid the reduction in convergence rate caused by differentiation and also to improve the numerical stability of a discrete solution. In this research, we use the following notations: $\widehat{[\,]}$ for a vector/matrix $[\,]$ that is associated with a grid line, and $[\,]_{(n)}$ to denote selected components of the vector$[\,]$. There are many types of radial basis functions (RBFs) such as Gaussians, multiquadrics (MQ), inverse multiquadrics and thin plate spline. Owing to the excellent performance of the multiquadrics RBF in the function approximation (Franke, 1982), we use it in this work. The MQ-RBF has the following form

$$G_i(x) = \sqrt{(x - c_i)^2 + {a_i}^2}\,,$$

where c_i and a_i are the centre and width of the i^{th} MQ-RBF, respectively. The set of centres is chosen to be the same as the set of collocation points, and the RBF width is determined as $a_i = bd_i$, $b > 0$ is a factor (presently $b = 1$), and d_i is the distance from the i-th centre to the nearest. The domain of interest is discretized using a uniform Cartesian grid having N nodes on the x-axis.

Applying the basic idea of the integral RBF form (Mai-Duy and Tran-Cong, 2001*a*) we decompose a 6th-order derivative of the function w into RBFs. The RBF networks are then integrated to obtain the lower-order derivatives and the function itself. We have

$$\frac{\partial^6 w(x,t)}{\partial x^6} = \sum_{i=1}^{N} u_i(t) G_i(x) = \sum_{i=1}^{N} u_i(t) H_6^{(i)}(x)\,, \tag{4.4}$$

$$\frac{\partial^5 w(x,t)}{\partial x^5} = \sum_{i=1}^{N} u_i(t) H_5^{(i)}(x) + c_1\,, \tag{4.5}$$

$$\frac{\partial^4 w(x,t)}{\partial x^4} = \sum_{i=1}^{N} u_i(t) H_4^{(i)}(x) + c_1 x + c_2\,, \tag{4.6}$$

$$\frac{\partial^3 w(x,t)}{\partial x^3} = \sum_{i=1}^{N} u_i(t) H_3^{(i)}(x) + \frac{c_1}{2}x^2 + c_2 x + c_3\,, \tag{4.7}$$

$$\frac{\partial^2 w(x,t)}{\partial x^2} = \sum_{i=1}^{N} u_i(t) H_2^{(i)}(x) + \frac{c_1}{6}x^3 + \frac{c_2}{2}x^2 + c_3 x + c_4\,, \tag{4.8}$$

$$\frac{\partial w(x,t)}{\partial x} = \sum_{i=1}^{N} u_i(t) H_1^{(i)}(x) + \frac{c_1}{24}x^4 + \frac{c_2}{6}x^3 + \frac{c_3}{2}x^2 + c_4 x + c_5\,, \tag{4.9}$$

$$w(x,t) = \sum_{i=1}^{N} u_i(t) H_0^{(i)}(x) + \frac{c_1}{120}x^5 + \frac{c_2}{24}x^4 + \frac{c_3}{6}x^3 + \frac{c_4}{2}x^2 + c_5 x + c_6\,, \tag{4.10}$$

where $\{G_i(x)\}_{i=1}^N = \{H_6^{(i)}(x)\}_{i=1}^N$ are known RBFs; $H_5^{(i)}(x) = \int H_6^{(i)}(x)dx$; $H_4^{(i)}(x) = \int H_5^{(i)}(x)dx$; $H_3^{(i)}(x) = \int H_4^{(i)}(x)dx$; $H_2^{(i)}(x) = \int H_3^{(i)}(x)dx$; $H_1^{(i)}(x) = \int H_2^{(i)}(x)dx$; $H_0^{(i)}(x) = \int H_1^{(i)}(x)dx$; $\{c_i\}_{i=1}^6$ the set of constants arising from the integration process. The new basis functions $H_5^{(i)}(x)$, $H_4^{(i)}(x)$, $H_3^{(i)}(x)$, $H_2^{(i)}(x)$ and $H_1^{(i)}(x)$ are

obtained from integrating the multiquadrics as follows,

$$
\begin{aligned}
H_5^{(i)}(x) &= \frac{r}{2}\sqrt{r^2+{a_i}^2} + \frac{{a_i}^2}{2}\ln\left|r+\sqrt{r^2+{a_i}^2}\right| ,\\
H_4^{(i)}(x) &= \left(\frac{r^2}{6} - \frac{{a_i}^2}{3}\right)\sqrt{r^2+{a_i}^2} + \frac{{a_i}^2 r}{2}\ln\left|r+\sqrt{r^2+{a_i}^2}\right| ,\\
H_3^{(i)}(x) &= \left(\frac{r^3}{24} - \frac{13{a_i}^2 r}{48}\right)\sqrt{r^2+{a_i}^2} + \left(\frac{{a_i}^2 r^2}{4} - \frac{{a_i}^4}{16}\right)\ln\left|r+\sqrt{r^2+{a_i}^2}\right| ,\\
H_2^{(i)}(x) &= \left(\frac{r^4}{120} - \frac{83{a_i}^2 r^2}{720} + \frac{{a_i}^4}{45}\right)\sqrt{r^2+{a_i}^2} + \left(\frac{{a_i}^2 r^3}{12} - \frac{{a_i}^4 r}{16}\right)\ln\left|r+\sqrt{r^2+{a_i}^2}\right|\Bigg) ,\\
H_1^{(i)}(x) &= \left(\frac{r^5}{720} - \frac{97{a_i}^2 r^3}{2880} + \frac{113{a_i}^4 r}{5760}\right)\sqrt{r^2+{a_i}^2}\\
&\quad + \left(\frac{{a_i}^2 r^4}{48} - \frac{{a_i}^4 r^2}{32} + \frac{{a_i}^6}{384}\right)\ln\left|r+\sqrt{r^2+{a_i}^2}\right| ,\\
H_0^{(i)}(x) &= \left(\frac{r^6}{5040} - \frac{253{a_i}^2 r^4}{33600} + \frac{593{a_i}^4 r^2}{67200} - \frac{{a_i}^6}{1575}\right)\sqrt{r^2+{a_i}^2}\\
&\quad + \left(\frac{{a_i}^2 r^5}{240} + \frac{{a_i}^6 r}{384} - \frac{{a_i}^4 r^3}{96}\right)\ln\left|r+\sqrt{r^2+{a_i}^2}\right| ,
\end{aligned}
$$

where $r = x - c_i$. After discretization, Eqs. (4.4)–(4.10) can be written in a compact form as

$$
\widehat{\frac{\partial^6 w}{\partial x^6}} = \widehat{H_6^{(i)}}\widehat{\alpha}\,, \quad \widehat{\frac{\partial^5 w}{\partial x^5}} = \widehat{H_5^{(i)}}\widehat{\alpha}\,, \quad \widehat{\frac{\partial^4 w}{\partial x^4}} = \widehat{H_4^{(i)}}\widehat{\alpha}\,,
$$

$$
\widehat{\frac{\partial^3 w}{\partial x^3}} = \widehat{H_3^{(i)}}\widehat{\alpha}\,, \quad \widehat{\frac{\partial^2 w}{\partial x^2}} = \widehat{H_2^{(i)}}\widehat{\alpha}\,, \quad \widehat{\frac{\partial w}{\partial x}} = \widehat{H_1^{(i)}}\widehat{\alpha}\,, \quad \widehat{w} = \widehat{H_0^{(i)}}\widehat{\alpha}\,, \tag{4.11}
$$

where

$$
\widehat{H_6^{(i)}} = \begin{bmatrix}
H_6^{(1)}(x_1) & H_6^{(2)}(x_1) & \dots & H_6^{(N)}(x_1) & 0 & 0 & 0 & 0 & 0 & 0\\
H_6^{(1)}(x_2) & H_6^{(2)}(x_2) & \dots & H_6^{(N)}(x_2) & 0 & 0 & 0 & 0 & 0 & 0\\
\dots & \dots & \dots & \dots & \dots & \dots & \dots & \dots & \dots & \dots\\
H_6^{(1)}(x_N) & H_6^{(2)}(x_N) & \dots & H_6^{(N)}(x_N) & 0 & 0 & 0 & 0 & 0 & 0
\end{bmatrix}, \tag{4.12}
$$

$$
\widehat{H_5^{(i)}} = \begin{bmatrix}
H_5^{(1)}(x_1) & H_5^{(2)}(x_1) & \dots & H_5^{(N)}(x_1) & 1 & 0 & 0 & 0 & 0 & 0\\
H_5^{(1)}(x_2) & H_5^{(2)}(x_2) & \dots & H_5^{(N)}(x_2) & 1 & 0 & 0 & 0 & 0 & 0\\
\dots & \dots & \dots & \dots & \dots & \dots & \dots & \dots & \dots & \dots\\
H_5^{(1)}(x_N) & H_5^{(2)}(x_N) & \dots & H_5^{(N)}(x_N) & 1 & 0 & 0 & 0 & 0 & 0
\end{bmatrix}, \tag{4.13}
$$

...,

$$\widehat{H_0^{(i)}} = \begin{bmatrix} H_0^{(1)}(x_1) & H_0^{(2)}(x_1) & \dots & H_0^{(N)}(x_1) & x_1^5/5! & x_1^4/4! & x_1^3/3! & x_1^2/2! & x_1 & 1 \\ H_0^{(1)}(x_2) & H_0^{(2)}(x_2) & \dots & H_0^{(N)}(x_2) & x_2^5/5! & x_2^4/4! & x_2^3/3! & x_2^2/2! & x_2 & 1 \\ \dots & \dots & \dots & \dots & \dots & \dots & \dots & \dots & \dots & \dots \\ H_0^{(1)}(x_N) & H_0^{(2)}(x_N) & \dots & H_0^{(N)}(x_N) & x_N^5/5! & x_N^4/4! & x_N^3/3! & x_N^2/2! & x_N & 1 \end{bmatrix}, \tag{4.14}$$

where $\{x_i\}_{i=1}^N$ is the set of nodal points, $\widehat{w} = (w_1, w_2, w_3, ..., w_N)^T$, $w_i = w(x_i, t)$, $\widehat{u} = (u_1, u_2, u_3, ..., u_N)^T$ and $\widehat{c} = (c_1, c_2, c_3, c_4, c_5, c_6)^T$. We denote $\widehat{\alpha} = (u_1, u_2, u_3, ..., u_N, c_1, c_2, ..., c_6)^T$. Equation (4.3) is discretized with respect to both time and space variables. Firstly, the time interval $[0, T]$ is partitioned into N subintervals $[t^{(n)}, t^{(n+1)}]$ of length $\Delta t = T/N$ with $t^{(0)} = 1$ and $t^{(N+1)} = T$. The discretization of the problem in time is then accomplished by a time stepping scheme, followed by the spatial discretization based on the IRBFN method. Among many possible time-stepping schemes, the standard θ-scheme (Quarteroni and Valli, 2008), $0 \leq \theta \leq 1$ is used in this work,

$$\frac{w^{(n+1)} - w^{(n)}}{\Delta t} = \theta W^{(n+1)} + (1-\theta) W^{(n)}, \tag{4.15}$$

where W denotes the right hand side (RHS) of (4.3). Note that the case $\theta = 0$ corresponds to the explicit forward Euler method and $\theta = 1$ to the implicit backward Euler method. The scheme associated with the case $\theta = 1/2$ is equivalent to the (semi-implicit) Crank-Nicolson method which is second-order accurate.

We re-write Eq. (4.3) as

$$\frac{\partial w}{\partial t} = f(w) \tag{4.16}$$

where

$$f(w) = A\frac{\partial^6 w}{\partial x^6} - B\left[12w^2\left(\frac{\partial w}{\partial x}\right)^2 + 4w^3\frac{\partial^2 w}{\partial x^2}\right] + 5Cw^4\frac{\partial w}{\partial x}. \tag{4.17}$$

Applying the standard θ-scheme with $\theta = 1/2$ to Eq. (4.16) results in

$$\frac{w^{(n+1)} - w^{(n)}}{\Delta t} = \frac{1}{2}\left[f(w)\right]^{(n+1)} + \frac{1}{2}\left[f(w)\right]^{(n)} \tag{4.18}$$

where $\triangle t = t^{(n+1)} - t^{(n)}$ is the physical time step; and the superscripts (n) and $(n+1)$ denote the previous and current physical time levels, respectively. Note that $[f(w)]^{(n+1)}$ in Eq. (4.18) consists of nonlinear terms. In order to linearize these nonlinear terms, we add a pseudo term into Eq. (4.18) as follows (Jameson, 1991; Ngo-Cong et al., 2012*b*):

$$\frac{\partial w}{\partial \tau} + \frac{w^{(n+1)}}{\Delta t} - \frac{1}{2}\left[f(w)\right]^{(n+1)} = \frac{w^{(n)}}{\Delta t} + \frac{1}{2}\left[f(w)\right]^{(n)} \tag{4.19}$$

where τ is the pseudo time. Linearization of Eq. (4.19) using the Picard iteration method (Islam et al., 2017; Paniconi and Putti, 1994) yields

$$\begin{aligned}
&\frac{w^{(n+1,m+1)} - w^{(n+1,m)}}{\Delta \tau} + \frac{w^{(n+1,m+1)}}{\Delta t} \\
&- \frac{1}{2}\left\{ A\Big(\frac{\partial^6 w}{\partial x^6}\Big)^{(n+1,m+1)} + 5C\left(w^4\right)^{(n+1,m)}\Big(\frac{\partial w}{\partial x}\Big)^{(n+1,m+1)} \right. \\
&\left. -B\left[12w^{(n+1,m)}\Big(\Big(\frac{\partial w}{\partial x}\Big)^2\Big)^{(n+1,m)} w^{(n+1,m+1)} + 4\left(w^3\right)^{(n+1,m)}\left(\frac{\partial^2 w}{\partial x^2}\right)^{(n+1,m+1)}\right]\right\} \\
&= \frac{w^{(n)}}{\Delta t} + \frac{1}{2}\left[f(w)\right]^{(n)}
\end{aligned} \tag{4.20}$$

or

$$\begin{aligned}
&\frac{w^{(n+1,m+1)}}{\Delta \tau} + \frac{w^{(n+1,m+1)}}{\Delta t} - \frac{1}{2}\left\{ A\Big(\frac{\partial^6 w}{\partial x^6}\Big)^{(n+1,m+1)} + 5C\left(w^4\right)^{(n+1,m)}\Big(\frac{\partial w}{\partial x}\Big)^{(n+1,m+1)} \right. \\
&\left. -B\left[12w^{(n+1,m)}\Big(\Big(\frac{\partial w}{\partial x}\Big)^2\Big)^{(n+1,m)} w^{(n+1,m+1)} + 4\left(w^3\right)^{(n+1,m)}\left(\frac{\partial^2 w}{\partial x^2}\right)^{(n+1,m+1)}\right]\right\} \\
&= \frac{w^{(n+1,m)}}{\Delta \tau} + \frac{w^{(n)}}{\Delta t} + \frac{1}{2}\left[f(w)\right]^{(n)}
\end{aligned} \tag{4.21}$$

where $\triangle \tau = \tau^{(n+1)} - \tau^{(n)}$ is the pseudo time step; and the superscripts (m) and $(m+1)$ denote the previous and current pseudo time levels, respectively. Eq. (4.21) is then discretized in space using the 1D-IRBFN method. After inserting appropriate

values of w and its derivatives using (4.11), Eq. (4.21) is written as

$$\left[\begin{array}{l} \frac{\widehat{H}_0}{\Delta\tau}+\frac{\widehat{H}_0}{\Delta t} \\ -\frac{1}{2}\left\{\begin{array}{l} A\widehat{H}_6+5C\left(\widehat{H}_0\widehat{\alpha}^{(n+1,m)}\right)^4\widehat{H}_1 \\ -B\left[12\widehat{H}_0\widehat{\alpha}^{(n+1,m)}\left(\widehat{H}_1\widehat{\alpha}^{(n+1,m)}\right)^2\widehat{H}_0+4\left(\widehat{H}_0\widehat{\alpha}^{(n+1,m)}\right)^3\widehat{H}_2\right] \end{array}\right\} \end{array}\right]\widehat{\alpha}^{(n+1,m+1)}$$

$$=\frac{\widehat{H}_0\widehat{\alpha}^{(n+1,m)}}{\Delta\tau}+\left[\begin{array}{l} \frac{\widehat{H}_0}{\Delta t}+\frac{1}{2}\left\{\begin{array}{l} A\widehat{H}_6+5C\left(\widehat{H}_0\widehat{\alpha}^{(n)}\right)^4\widehat{H}_1 \\ -B\left[12\widehat{H}_0\widehat{\alpha}^{(n)}\left(\widehat{H}_1\widehat{\alpha}^{(n)}\right)^2\widehat{H}_0+4\left(\widehat{H}_0\widehat{\alpha}^{(n)}\right)^3\widehat{H}_2\right] \end{array}\right\} \end{array}\right]\widehat{\alpha}^{(n)} \tag{4.22}$$

For simplicity, the above equation can be written as,

$$E_1\widehat{\alpha}^{(n+1,m+1)}=\mathrm{RHS}_1^{(n+1,m)} \tag{4.23}$$

and the boundary conditions as

$$E_2\widehat{\alpha}^{(n+1,m+1)}=\mathrm{RHS}_2\,. \tag{4.24}$$

The Picard iteration is performed at every physical time level $(n+1)$. A stopping criteria for the Picard iteration is as follows:

$$CM=\frac{\sqrt{\sum_{i=1}^{N}\left(w_i^{(n+1,m+1)}-w_i^{(n+1,m)}\right)^2}}{\sqrt{\sum_{i=1}^{N}\left(w_i^{(n+1,m+1)}\right)^2}}<TOL \tag{4.25}$$

where TOL is a given tolerance and presently set to be 2×10^{-5}; and N the number of interior points. If the stopping criteria is fulfilled, we specify $w^{(n)}=w^{(n+1,m+1)}$, then advance the physical time t. The system of equations (4.23)–(4.24) is solved simultaneously at each time step for $\widehat{\alpha}^{(n+1,m+1)}$ until the prescribed time T is reached. Instead of iterating until the stopping criteria is achieved, one may iterate a specific number of pseudo-time steps. One-step Picard iteration corresponds to using the solution at the previous time level to linearize nonlinear terms. The linearization of

Eq. (4.18) using the one-step Picard iteration method yields

$$\frac{w^{(n+1)}}{\Delta t}-\frac{1}{2}\left\{A\Big(\frac{\partial^6 w}{\partial x^6}\Big)^{(n+1)}+5C\left(w^4\right)^{(n)}\left(\frac{\partial w}{\partial x}\right)^{(n+1)}\right.$$
$$\left.-B\left[12w^{(n)}\Big(\Big(\frac{\partial w}{\partial x}\Big)^2\Big)^{(n)}w^{(n+1)}+4\left(w^3\right)^{(n)}\left(\frac{\partial^2 w}{\partial x^2}\right)^{(n+1)}\right]\right\}=\frac{w^{(n)}}{\Delta t}+\frac{1}{2}\left[f\left(w\right)\right]^{(n)} \tag{4.26}$$

After inserting appropriate values of w and its derivatives using (4.11), equation (4.26) is written as

$$\left[\begin{array}{l}\frac{\widehat{H}_0}{\Delta t}-\frac{1}{2}\left\{\begin{array}{l}A\widehat{H}_6+5C\left(\widehat{H}_0\widehat{\alpha}^{(n)}\right)^4\widehat{H}_1\\ -B\left[12\widehat{H}_0\widehat{\alpha}^{(n)}\left(\widehat{H}_1\widehat{\alpha}^{(n)}\right)^2\widehat{H}_0+4\left(\widehat{H}_0\widehat{\alpha}^{(n)}\right)^3\widehat{H}_2\right]\end{array}\right\}\end{array}\right]\widehat{\alpha}^{(n+1)}=$$

$$\left[\begin{array}{l}\frac{\widehat{H}_0}{\Delta t}+\frac{1}{2}\left\{\begin{array}{l}A\widehat{H}_6+5C\left(\widehat{H}_0\widehat{\alpha}^{(n)}\right)^4\widehat{H}_1\\ -B\left[12\widehat{H}_0\widehat{\alpha}^{(n)}\left(\widehat{H}_1\widehat{\alpha}^{(n)}\right)^2\widehat{H}_0+4\left(\widehat{H}_0\widehat{\alpha}^{(n)}\right)^3\widehat{H}_2\right]\end{array}\right\}\end{array}\right]\widehat{\alpha}^{(n)} \tag{4.27}$$

For simplicity, the above equation can be written as,

$$E_1\widehat{\alpha}^{(n+1)}=\mathrm{RHS}_1 \tag{4.28}$$

and the boundary conditions as

$$E_2\widehat{\alpha}^{(n+1)}=\mathrm{RHS}_2\,. \tag{4.29}$$

The system of equations (4.28)–(4.29) is solved simultaneously at each physical time step for $\widehat{\alpha}^{(n+1)}$ until the prescribed time T is reached.

The following section presents the numerical results.

4.3 Results of the numerical experiments

In this section, we present the basic numerical solutions of the main equation (4.3).

We start by selecting the coefficients values, domain size and the initial condition.

They need to provide a reasonable (not too long) time for the dynamic to reach a settled stage (when the pulse is formed and settled in shape) and guarantee sufficient spatial resolution of the main hump and also the oscillatory tail (consequence of the 6th-order dissipation) visible on every graph. The initial condition needs to be large enough in order to prevent a collapse into a trivial state $w(x,t)$ =const, corresponding to the absence of motion. Eventually we chose $A = 1$, $B = 1$ and $C = 1$. Domain size can differ from experiment to experiment depending on the initial conditions. The initial conditions are shown in every figure. As for the boundary conditions, we use either homogeneous conditions, that is zero values of the function and its first two derivatives on the edges, or stipulate spatial periodicity of w implying equal values of w and its first five derivatives on the edges of the domain, respectively.

4.3.1 Single-pulse regime under homogeneous boundary conditions

In these numerical experiments the boundary conditions are chosen homogeneous, that is zero values of the function and its first two derivatives on the left and on the right edges,

$$w^{(k)}(x_0) = 0\,, \quad w^{(k)}(x_0 + L) = 0\,, \quad k = 0, 1, 2\,.$$

The initial condition is chosen to be

$$w(x, 0) = 1.2\, \exp[-0.25(x + 12.5)^2] \tag{4.30}$$

see Fig. 4.1 .

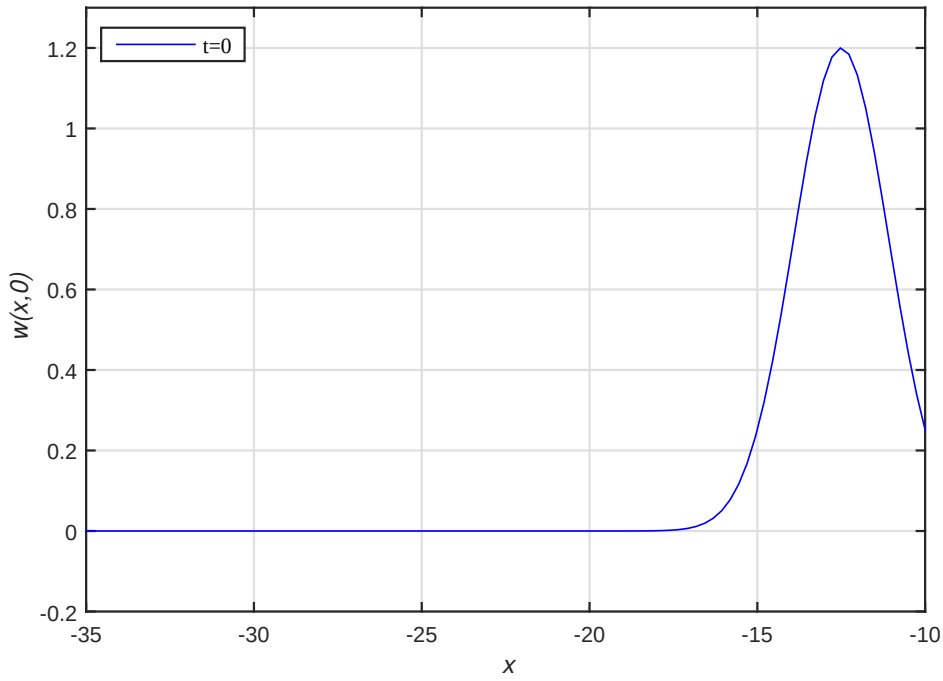

Figure 4.1: The initial condition (4.30).

Experiment 1: PI1 scheme

In the first experiment, we apply the 1D-IRBFN method in conjunction with PI1 scheme to solve the equation (4.3).

Fig. 4.2 presents the influence of time step on the 1D-IRBFN solution of Eq. (4.3) at the time moment $t = 7$ and a grid size of 100. It can be seen that present numerical results converge as the time step reduces.

Fig. 4.3 shows a grid convergence study of Eq. (4.3) at $t = 7$, using a time step of 0.001.

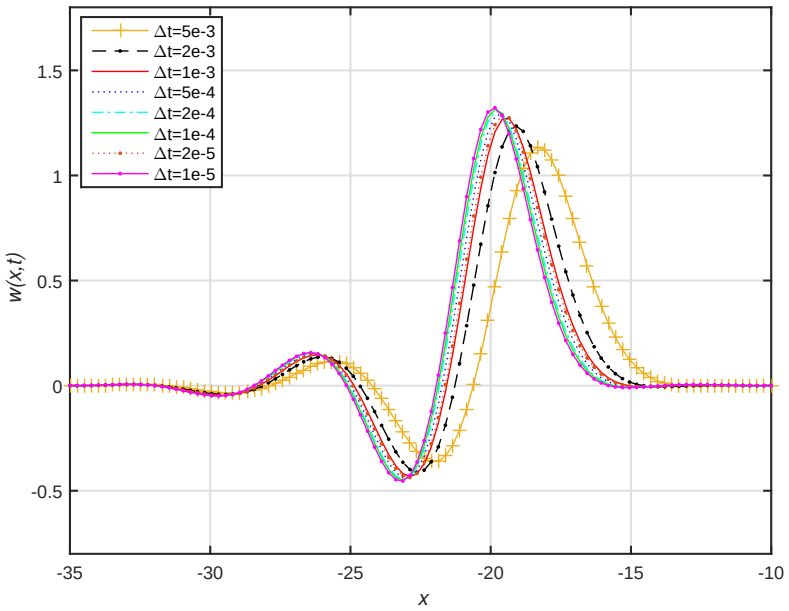

Figure 4.2: Time step convergence study using the PI1 scheme, at $t = 7$ and a grid size of 100 .

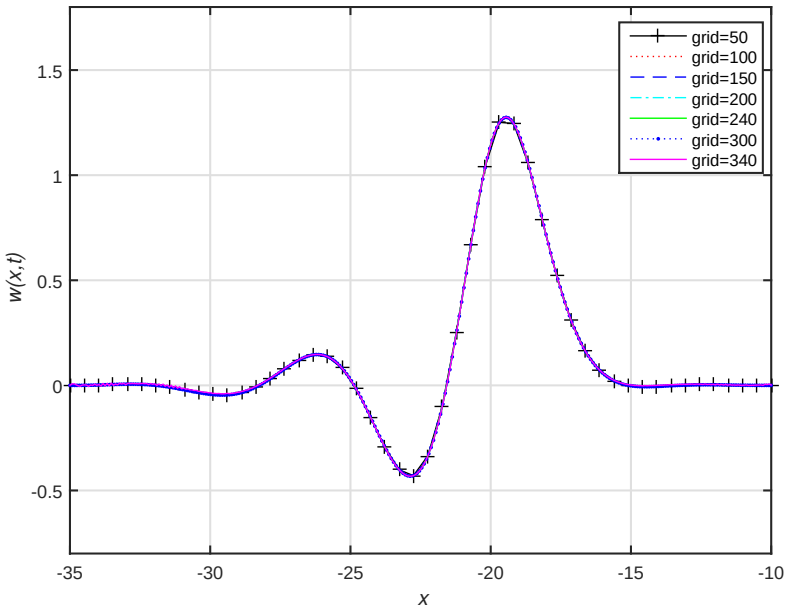

Figure 4.3: Grid convergence study using the PI1 scheme, at $t = 7$ and $\Delta t = 10^{-3}$.

As we can see the obtained results almost unchanged for the grid size greater than or equal to 100. Therefore, in the following analyses, we will use a grid of 100 and time step 0.001 to investigate the pulse propagation.

Fig. 4.4 shows the snapshots of the settled regime – it has the form of the pulse propagating to the left.

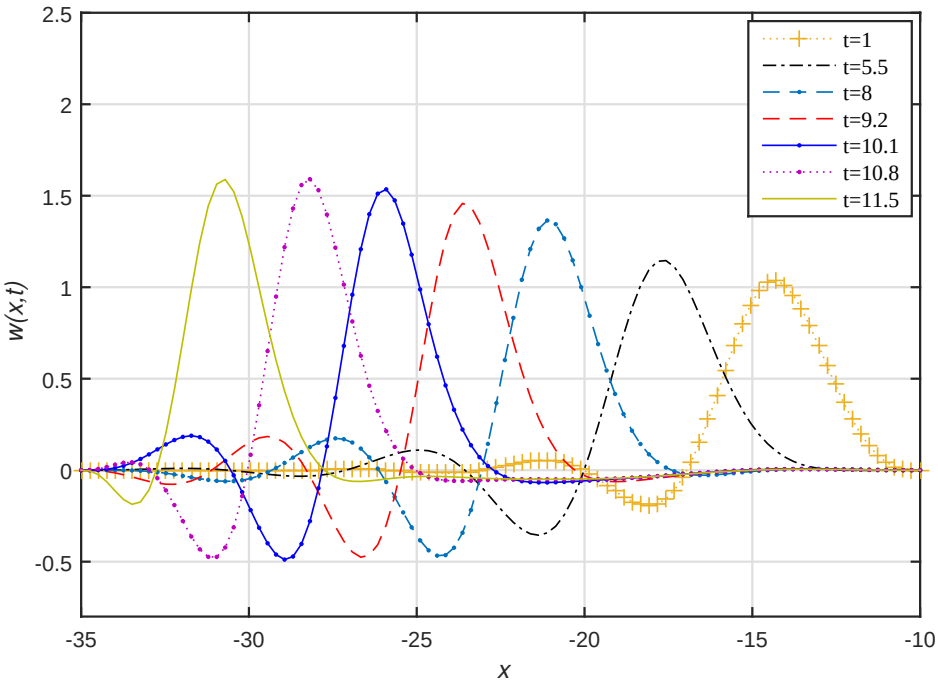

Figure 4.4: Numerical results of Eq. (4.3) at different moments ($t = 1$ to 11.5) using the PI1 scheme.

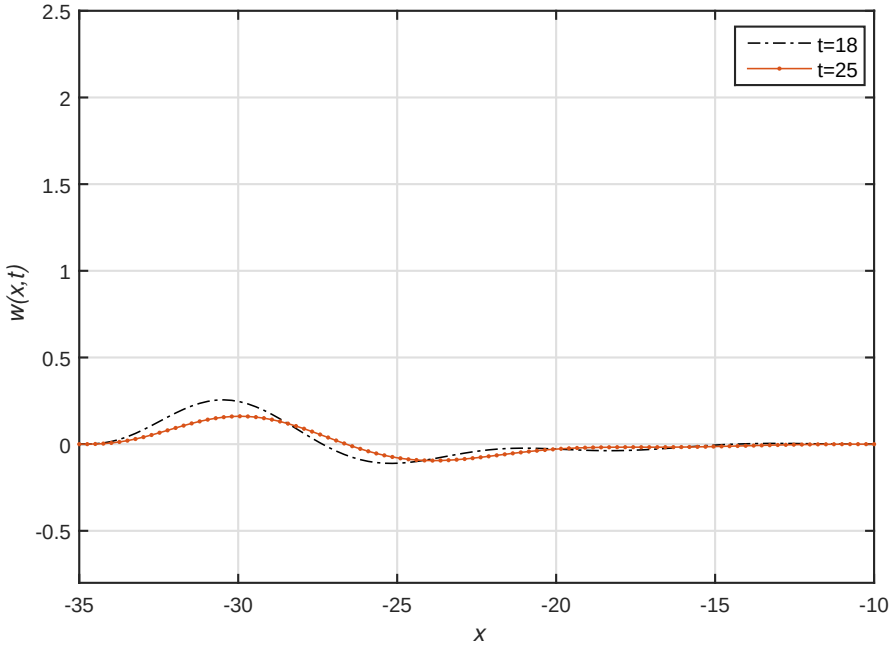

Figure 4.5: Continuation from Fig. 4.4 at $t = 18, 25$.

This is a typical outcome of the single-pulse experiments demonstrating the formation of the pulse from an arbitrary set initial condition. The pulse can only continue in this form until the presence of the boundary is felt. Fig. 4.5 shows that the pulse decays after hitting the boundary.

Experiment 2: PI scheme

In the second experiment, we apply the 1D-IRBFN method in conjunction with PI scheme to solve the equation (4.3).

Fig. 4.6 presents the time step convergence study for 1D-IRBFN methods in conjunction with PI scheme at the time moment $t = 7$ and a grid size of 100. It is noted that present numerical results converge with decreasing time step.

Fig. 4.7 shows a grid convergence study for 1D-IRBFN methods in conjunction with PI scheme at $t = 7$, using a time step of 0.001 .

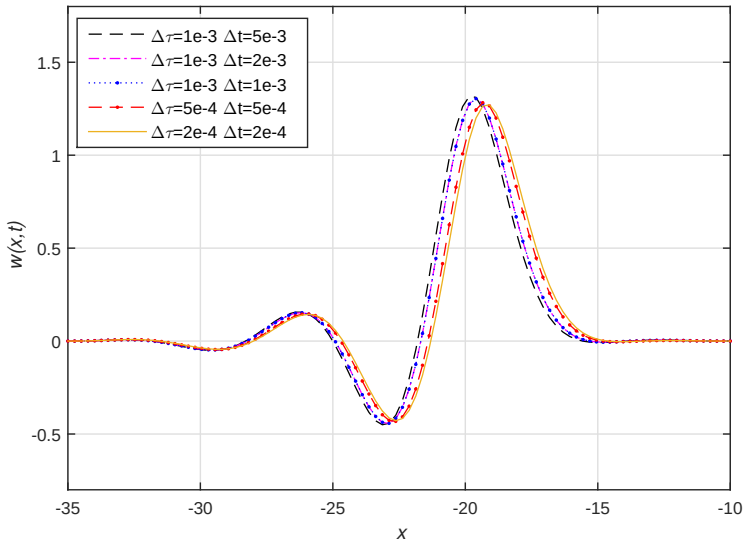

Figure 4.6: Time step convergence study using the PI scheme, at $t = 7$, $TOL = 2{\times}10^{-5}$ and a grid size of 100 .

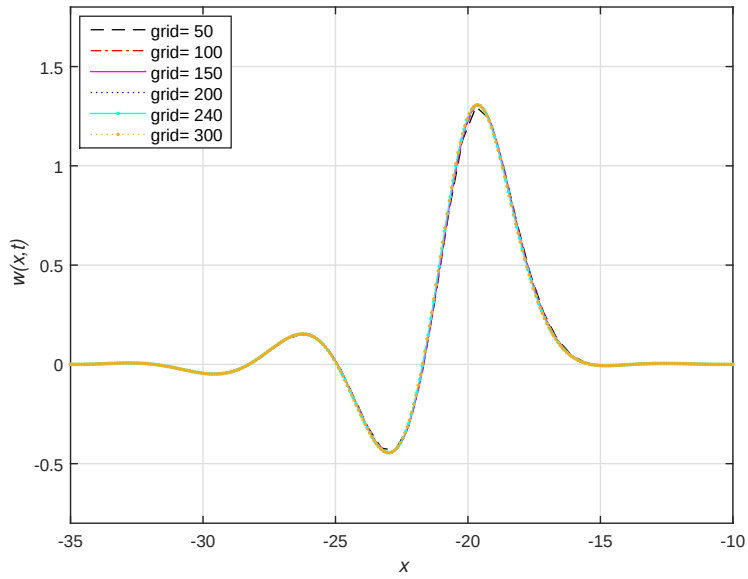

Figure 4.7: Grid convergence study using the PI scheme, at $t = 7$, $TOL = 2 \times 10^{-5}$, $\Delta\tau = 10^{-3}$ and $\Delta t = 10^{-3}$.

It can be seen that the obtained results are almost unchanged for different grid sizes. Therefore, in the following analyses, we will use a grid of 100 and time step 0.001 to investigate the pulse propagation.

The solution of Eq. (4.3) for different moments are given in Fig. 4.8. As expected the pulse moves from the right to the left with increasing time.

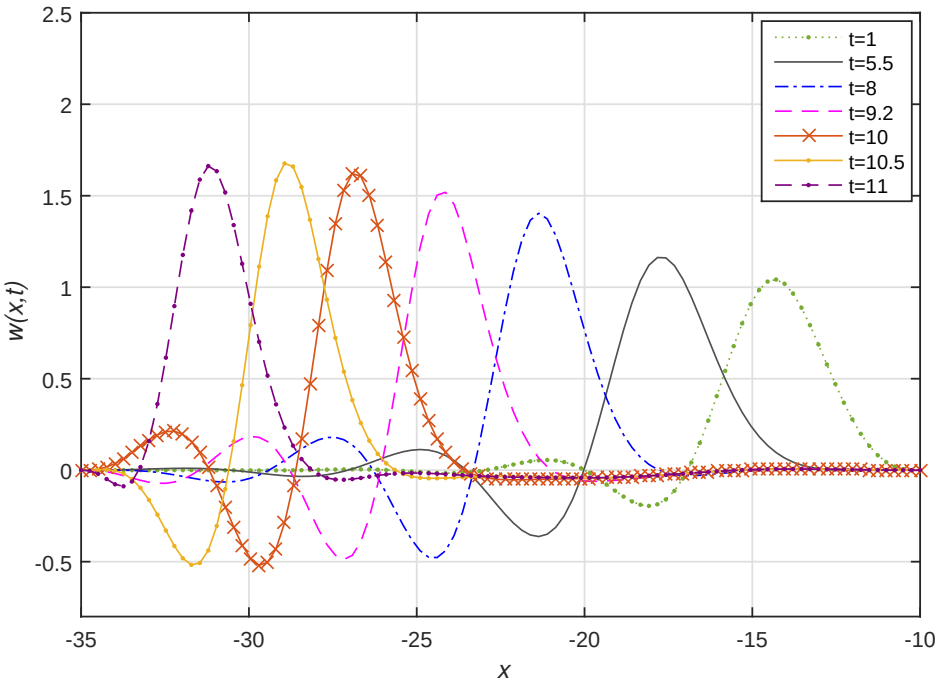

Figure 4.8: The snapshots from the numerical results of Eq. (4.3) at different moments ($t = 1$ to 11), $\Delta\tau = 10^{-3}$ and $TOL = 2 \times 10^{-5}$ using the PI scheme.

Fig. 4.9 shows that the pulse decays after hitting the boundary.

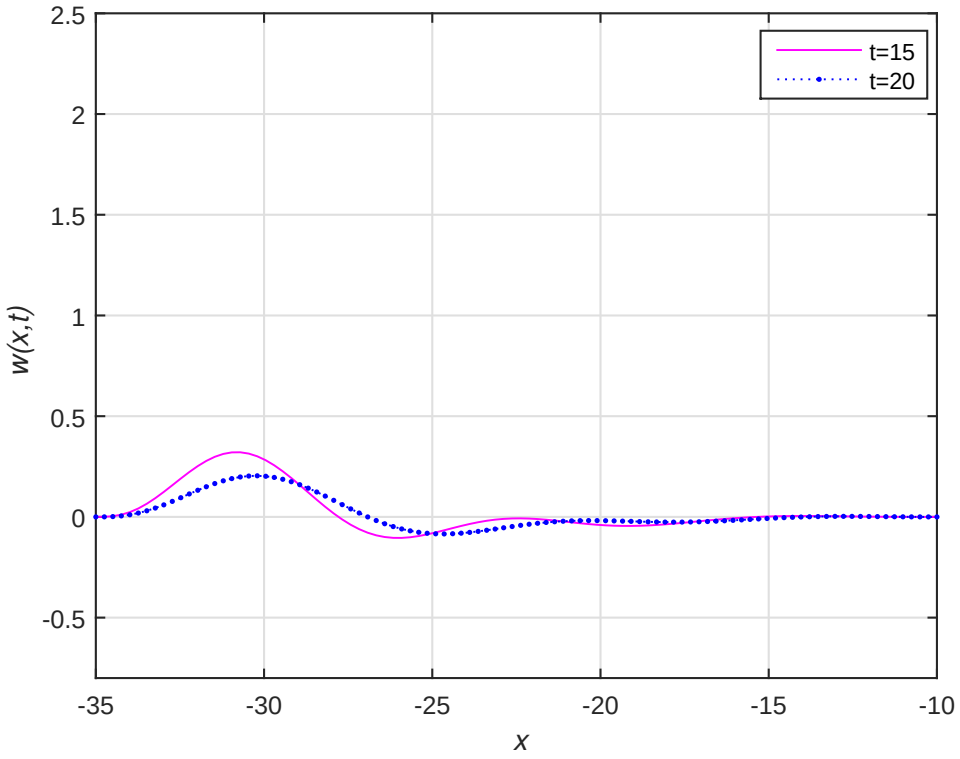

Figure 4.9: Continuation from Fig. 4.8, $t = 15, 20$.

Fig. 4.10 shows the comparison between PI and PI1 solutions of Eq. (4.3) at $t = 7$, using a grid size of 100, and $\Delta t = 10^{-3}$. For PI scheme, we use $\Delta\tau = 10^{-3}$ and $TOL = 2 \times 10^{-5}$. The two solutions are almost the same.

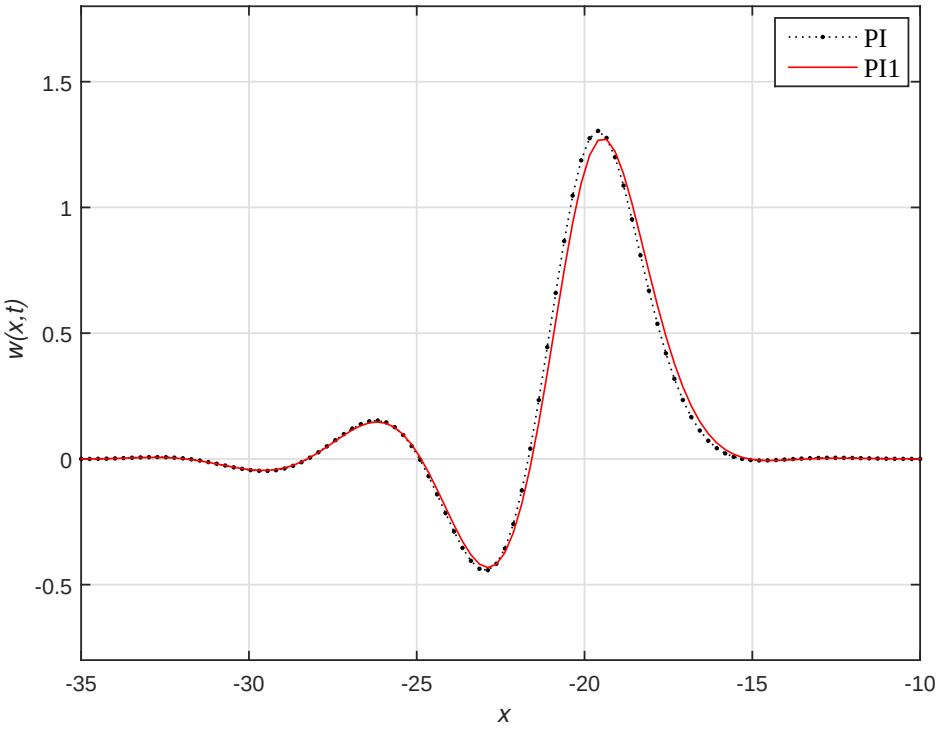

Figure 4.10: Compare between two schemes PI and PI1.

Tables 4.1 and 4.2 show the comparison of CPU time between PI and PI1 for different time step sizes and grid sizes, respectively. It can be seen that the PI1 scheme is more efficient than PI scheme in terms of the CPU time and yields almost the same result as that of the PI scheme as shown in Fig. 4.10. Therefore, we use the PI1 scheme in our numerical experiments in this study to investigate the propagation of the pulse through the channel.

Table 4.1: An autonomous model of pulse propagation (4.3) subject to homogeneous boundary conditions: comparison of CPU time at $t = 7$ and using a grid size of 100. For PI scheme, $\Delta\tau = 10^{-3}$, $TOL = 2 \times 10^{-5}$.

	CPU time (s)	
Δt	PI	PI1
5.00E-03	65.033382	2.937604
2.00E-03	46.659640	8.082634
1.00E-03	78.453442	17.251796
5.00e-04	148.616893	42.993233
2.00E-04	367.049220	176.331310

Table 4.2: An autonomous model of pulse propagation (4.3) subject to homogeneous boundary conditions: comparison of CPU time at $t = 7$, and $\Delta t = 10^{-3}$. For PI scheme, $\Delta\tau = 10^{-3}$, $TOL = 2 \times 10^{-5}$.

	CPU time (s)	
Grid	PI	PI1
51	62.212462	7.418407
101	78.453442	17.251796
151	104.972522	29.345711
201	155.340266	45.568273
301	542.258412	67.644509

4.3.2 Single-pulse regimes under periodic boundary conditions

In these numerical experiments, we use periodic boundary conditions with the period L. As Eq. (4.3) is of 6th order, the values of the function itself and its first five

derivatives on the left and the right edges of the domain are assumed to coincide, respectively.

$$w^{(k)}(x_0) = w^{(k)}(x_0 + L)\,, \quad k = 0, 1, 2, 3, 4, 5\,.$$

The number of nodes is 100, and the time step 0.001 .

In the first experiment, the initial condition is the same as in Section 4.3.1 and the size of the domain $L = 50$. Fig. 4.11 shows the initial condition and snapshots of the solution at early times. After a while, the solution takes the familiar pulse form as shown in Fig. 4.12 .

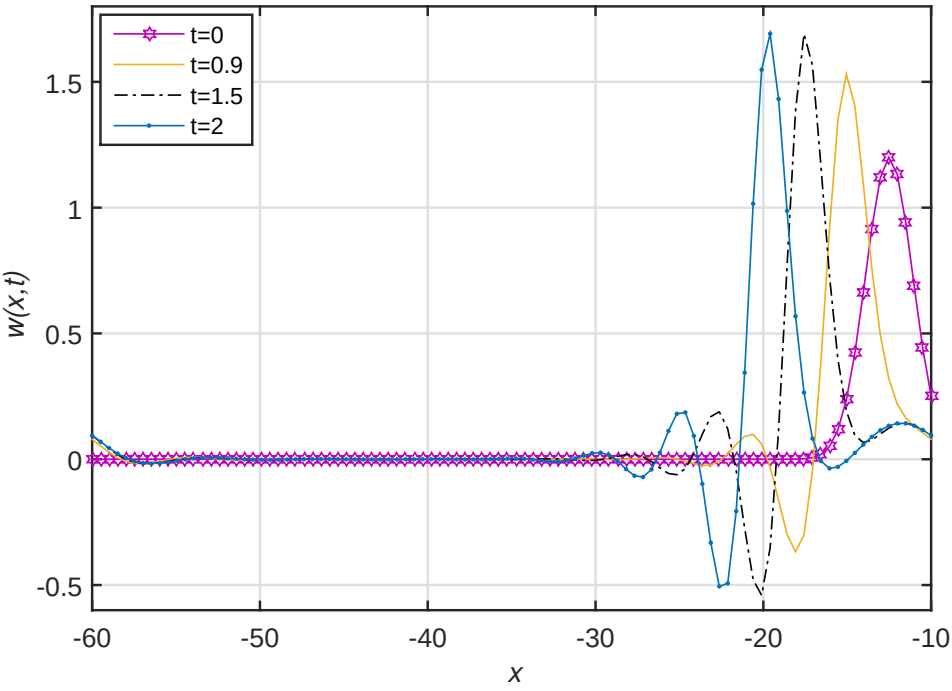

Figure 4.11: The initial condition $w(x, 0) = 1.2\,\exp[-0.25(x + 12.5)^2]$. The snapshots are for $t = 0$ to 2 .

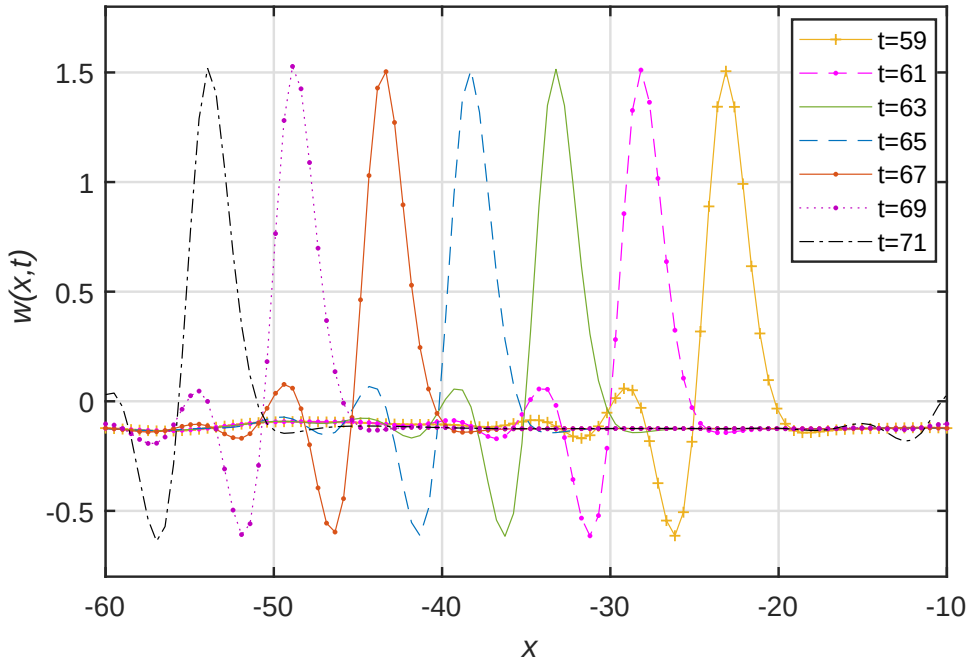

Figure 4.12: Continuation from Fig. 4.11, $t = 59$ to 71.

The initial condition in the next numerical experiment is

$$w(x, 0) = 1.8 \sin(x)\,, \tag{4.31}$$

as shown in Fig. 4.13, where the size of the domain $L = 35$. Here, the initial condition is not periodic and is, therefore, not consistent with the periodic boundary conditions. However, the equation quickly enforces periodicity, see Fig. 4.14. With time, the six initial crests gradually merge into one, settling down in the regime with one single pulse propagating to the left as in Fig. 4.15.

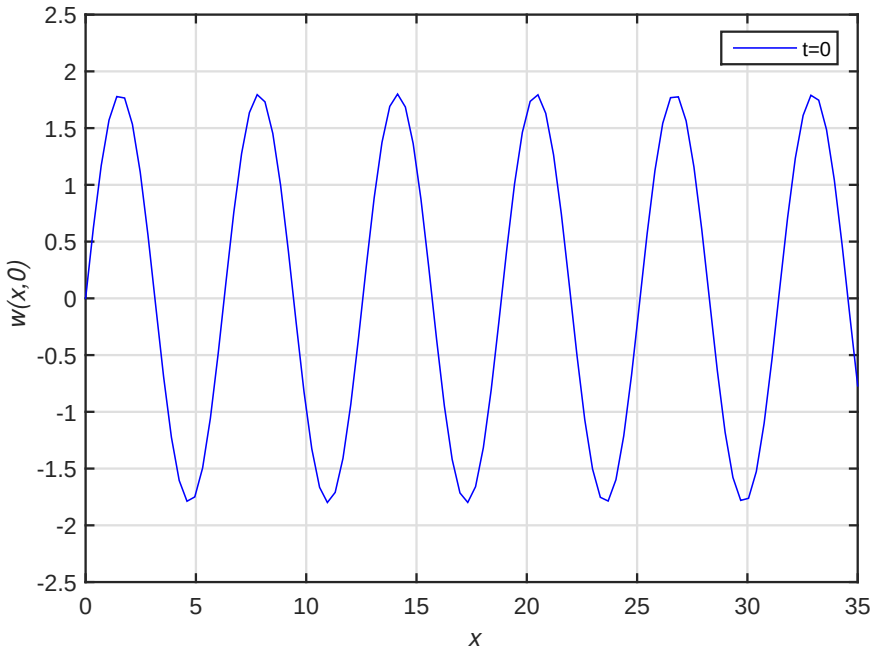

Figure 4.13: The initial condition (4.31).

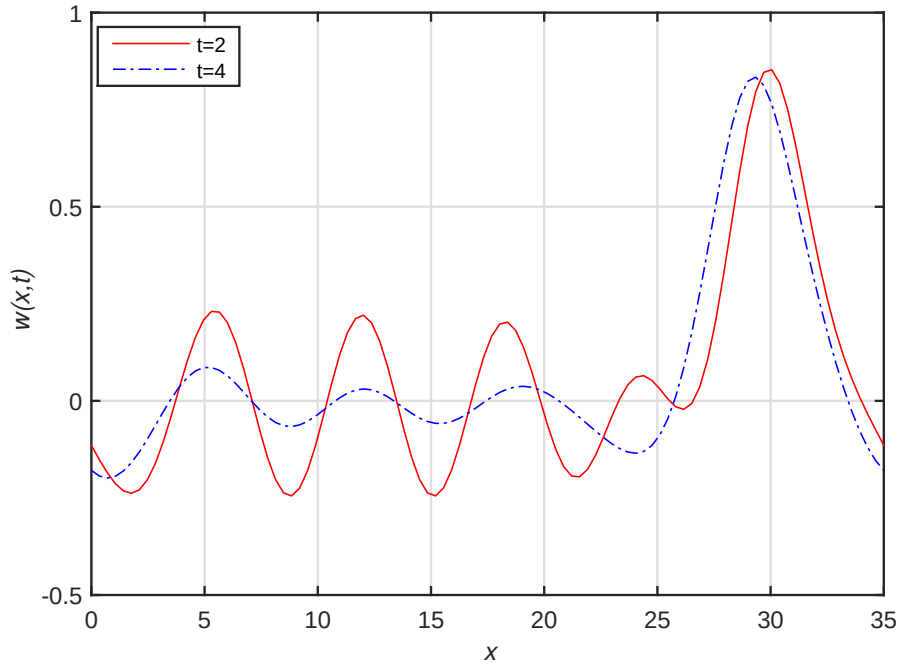

Figure 4.14: The solution evolved from the initial condition (4.31); the snapshots are for $t = 2, 4$.

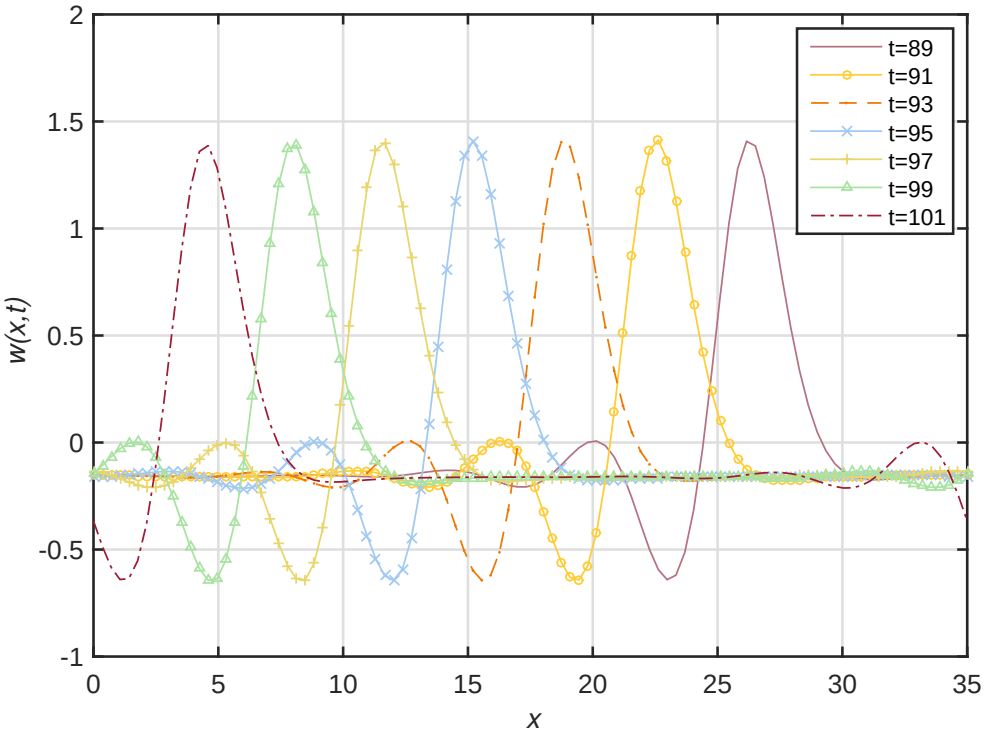

Figure 4.15: Continuation from Fig. 4.14, $t = 89$ to 101 .

In our last experiment, the initial condition is

$$w(x,0) = 1.3\,[\sin(x) + 0.5\sin(4x) + 0.125]\ , \tag{4.32}$$

as shown in Fig. 4.16, where the size of the domain $L = 35$. Fig. 4.17 shows the early stage of the evolution. After a sufficiently long time the solution settles in the form of single pulse shown in Fig. 4.18.

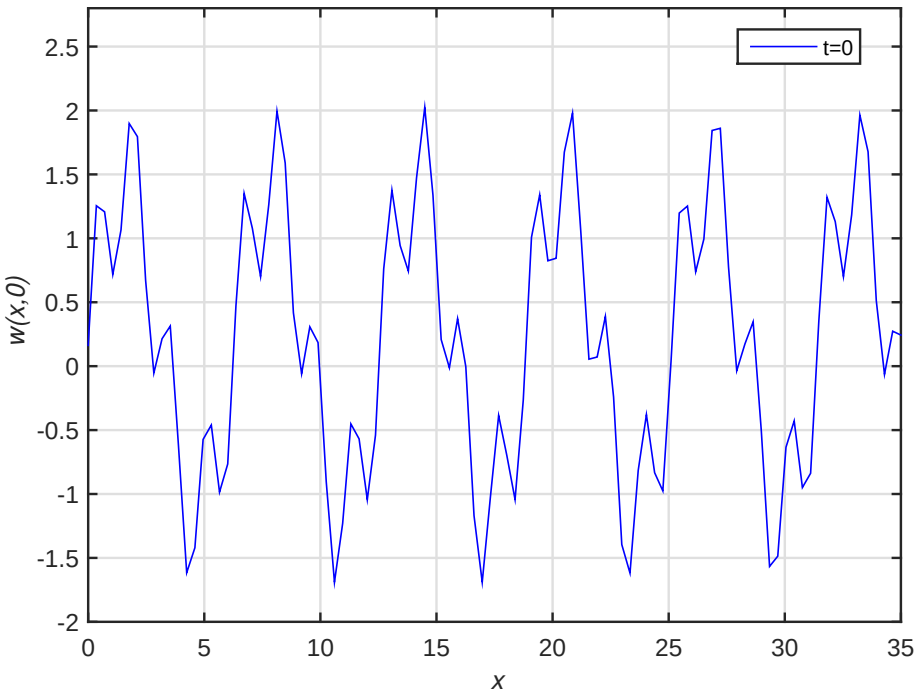

Figure 4.16: The initial condition (4.32).

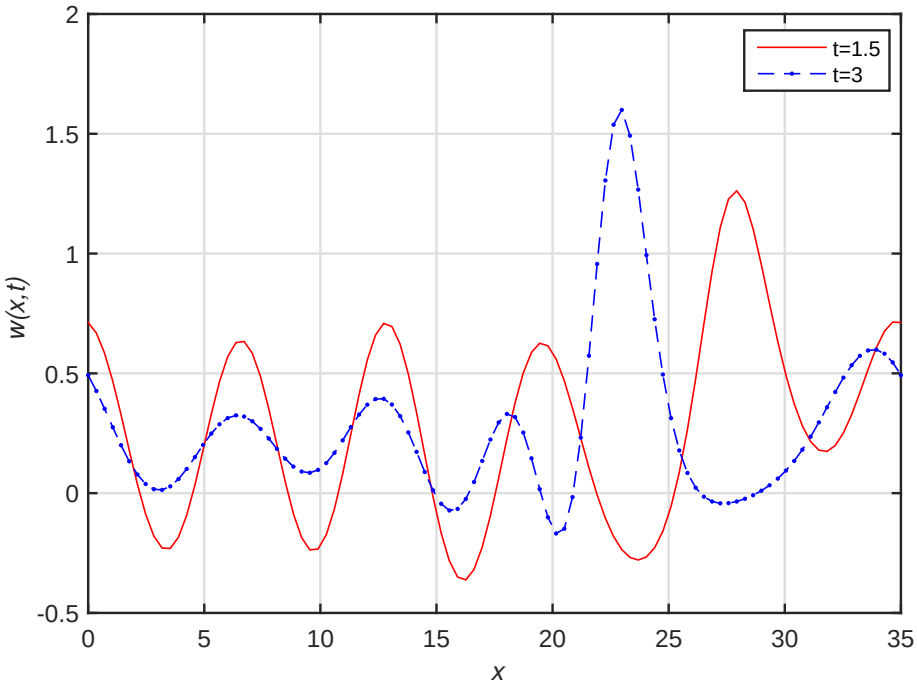

Figure 4.17: Early stage of the evolution; $t = 1.5, 3$.

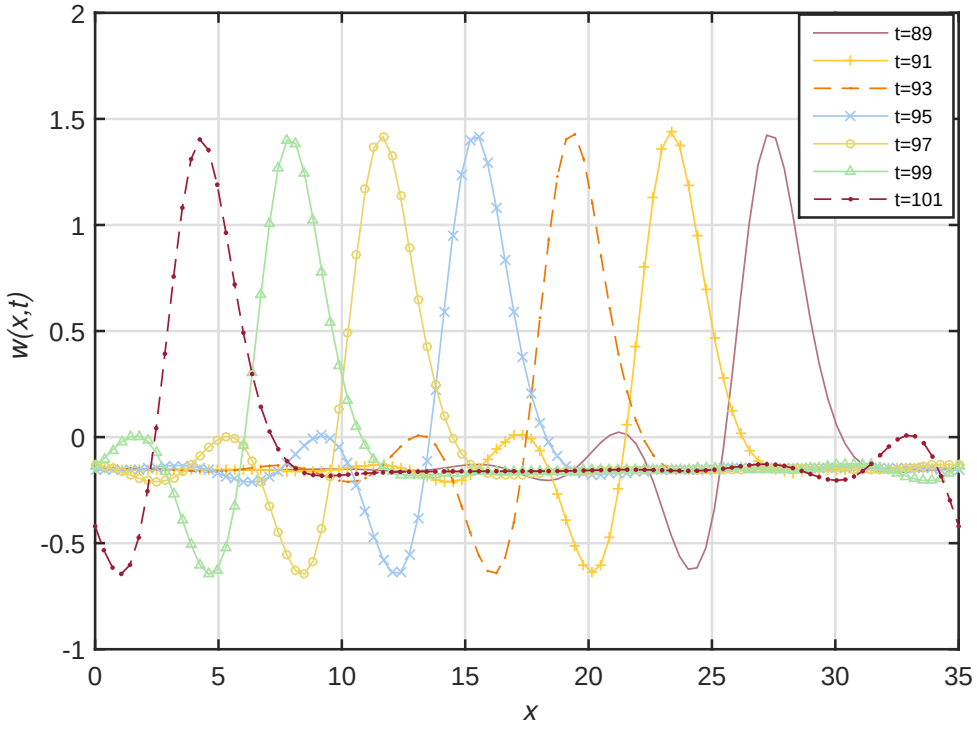

Figure 4.18: The settled regime between $t = 89$ and $t = 101$.

4.3.3 Multiple-pulse regimes under periodic boundary conditions

In our numerical experiments in this section we again use the periodic boundary conditions. The number of nodes is 100, and the time step 0.001. In the first numerical experiment the initial condition is chosen in the form of a large hump,

$$w(x,0) = 0.9\frac{[\exp(0.23(x+22.5)) - \exp(-0.23(x+22.5))]}{[\exp(0.23(x+22.5)) + \exp(-0.5(x+22.5))]}, \tag{4.33}$$

displayed in Fig. 4.19. Obviously this shape is not consistent with the periodic boundary conditions, however, the equation quickly enforces periodicity (Fig. 4.20) as in Figs. 4.13–4.14.

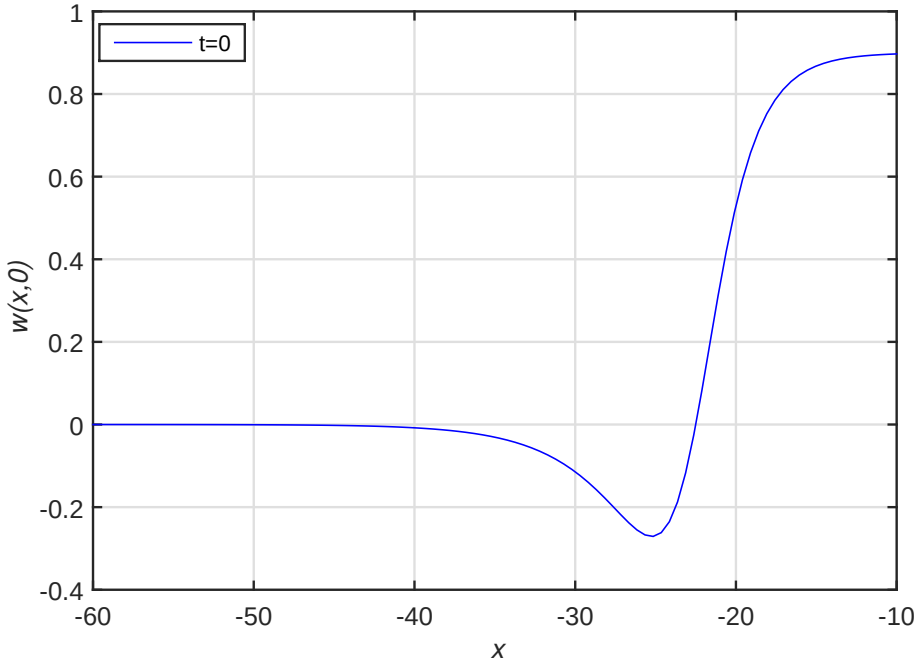

Figure 4.19: The initial condition (4.33).

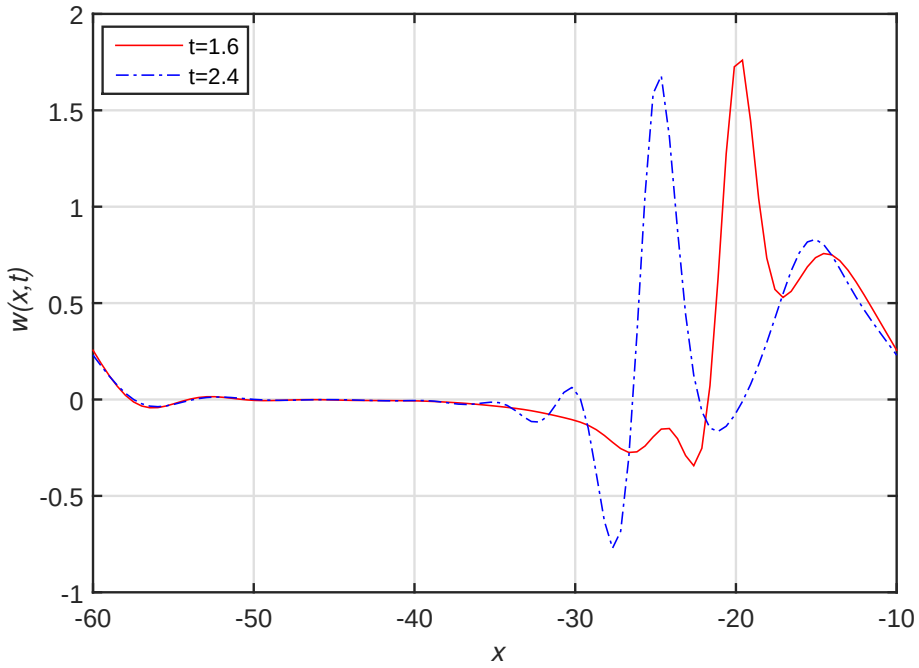

Figure 4.20: The snapshots at $t = 1.6, 2.4$.

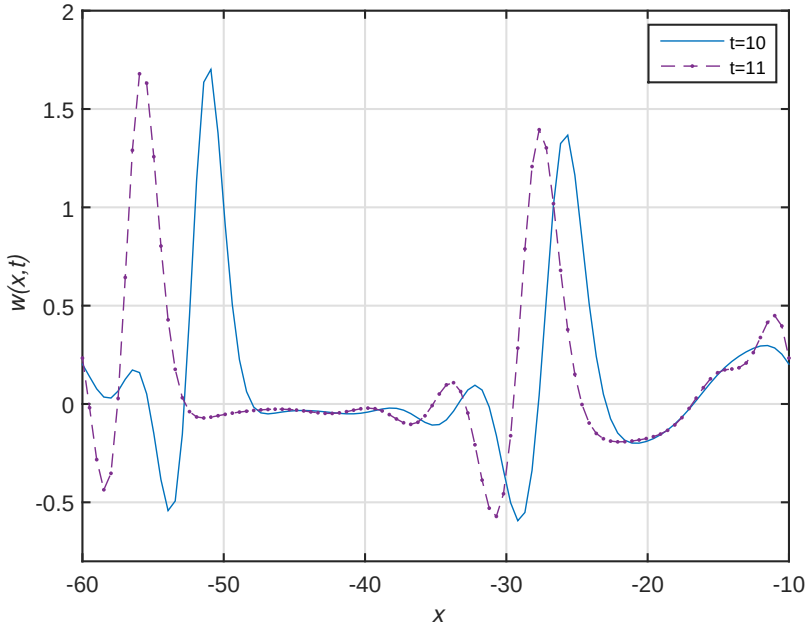

Figure 4.21: The snapshots at $t = 10, 11$.

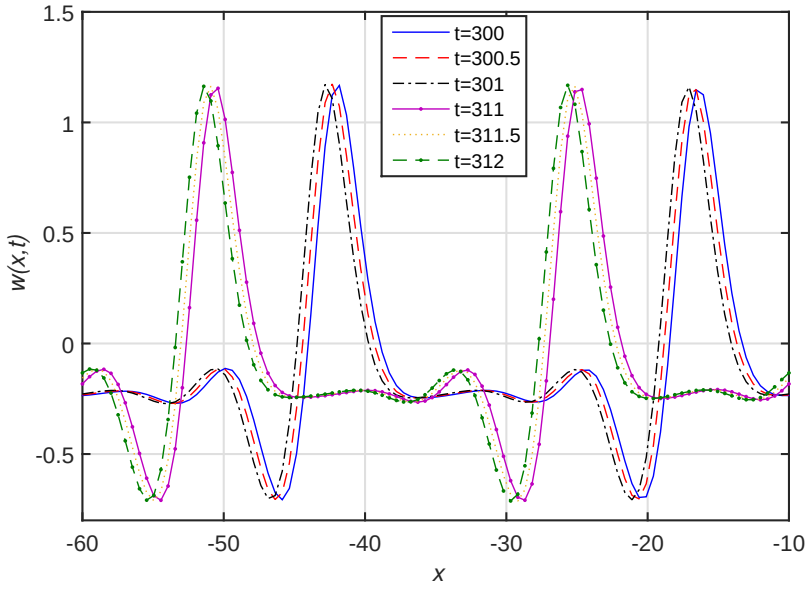

Figure 4.22: Continuation from Fig. 4.21, settled stage of the evolution. The snapshots are for the three close moments $t = 300, 300.5, 301$ and the another three close moments $t = 311, 311.5, 312$.

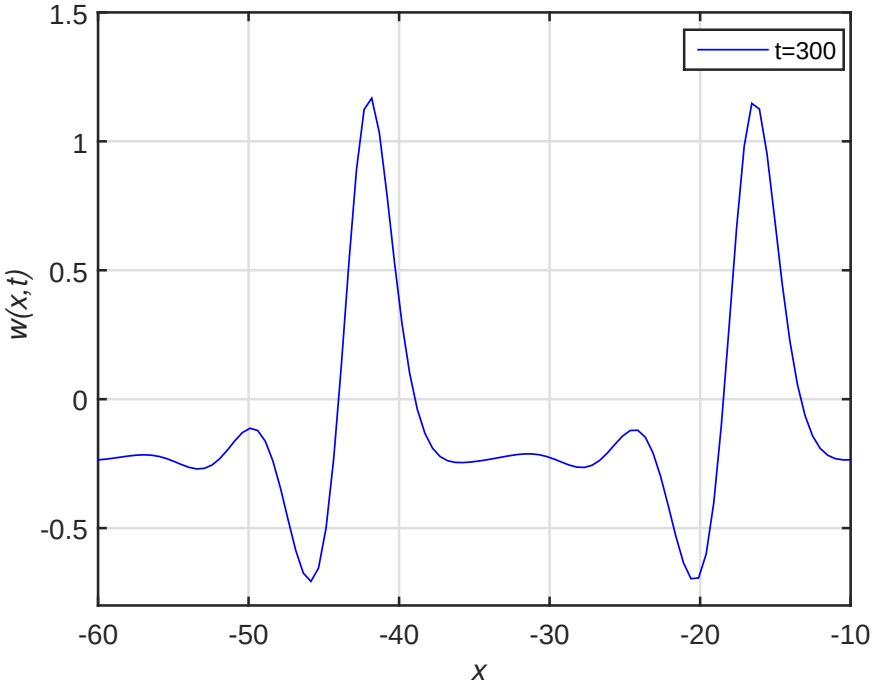

Figure 4.23: A selected profile from Fig. 4.22, $t = 300$.

See that after some time the big hump breaks down into two pulses (Figs. 4.20–4.21). We ran this experiments until the motion settled as demonstrated in Fig. 4.22. It shows the settled two-pulse formation separated by roughly one cycle; this is why we see four pulses in the figure. A single snapshot in Fig. 4.23 reveals that there are actually only two pulses at a moment.

We observe from Figs. 4.20–4.23 that the pulses gradually move away from each other before settling certain distance apart. Generally, for any experiment where two pulses are formed within one period L, the question is which of the following possibilities eventually realizes. Possibility 1: The distance between the pulses increases until the leading pulse (call it pulse 1) catches up with pulse 2 from behind, after which they merge back into a single pulse. In this case the distance, if measured from pulse 2 to pulse 1 from right to left, would become one full period. Possibility 2: The distance between the pulses becomes half the period. In this regime the

pulses may move either (a) without oscillations, or (b) with oscillations. Possibility 3: After an initial period of increase, the distance between the pulses decreases back to zero and the pulses re-combine. Possibility 4: The distance goes to (or oscillates about) a constant level which is not equal to half the period. In this and other similar experiments that we ran, possibility 2(b) realized, with the oscillations being relatively small. This is illustrated by Fig. 4.24.

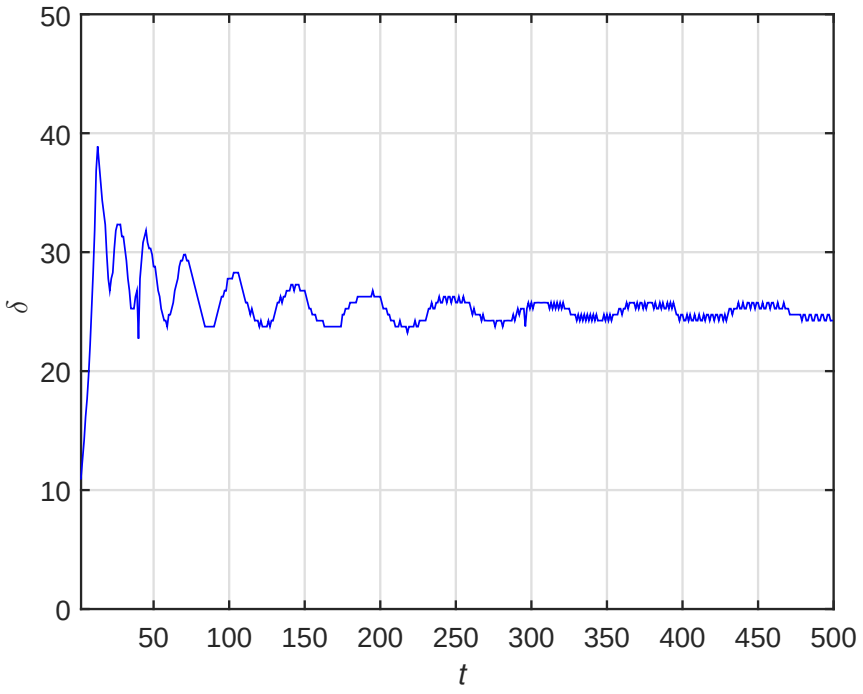

Figure 4.24: The evolution of the distance between two pulses. The period $L = 50$.

Our next group of experiments deal with three-pulse regimes within one period L. Of course, three pulses can be created in many different ways. We chose to seed them by an initial condition shaped as three sinusoidal crests as follows (Fig. 4.25),

$$w(x, 0) = 0.8 \sin(x/3) . \tag{4.34}$$

Figs. 4.26–4.28 show the early stage of the evolution. After a sufficiently long time the solution settles in the form shown in Fig. 4.29.

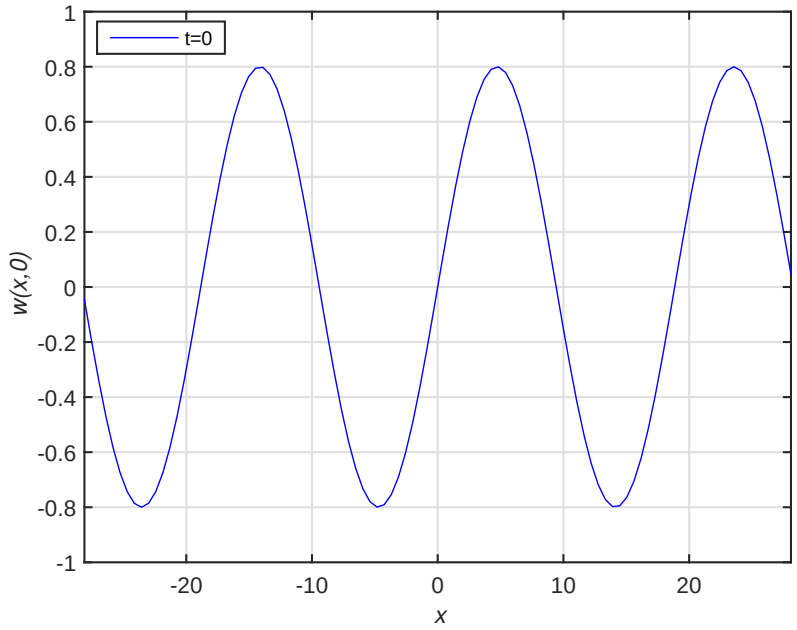

Figure 4.25: The initial condition (4.34).

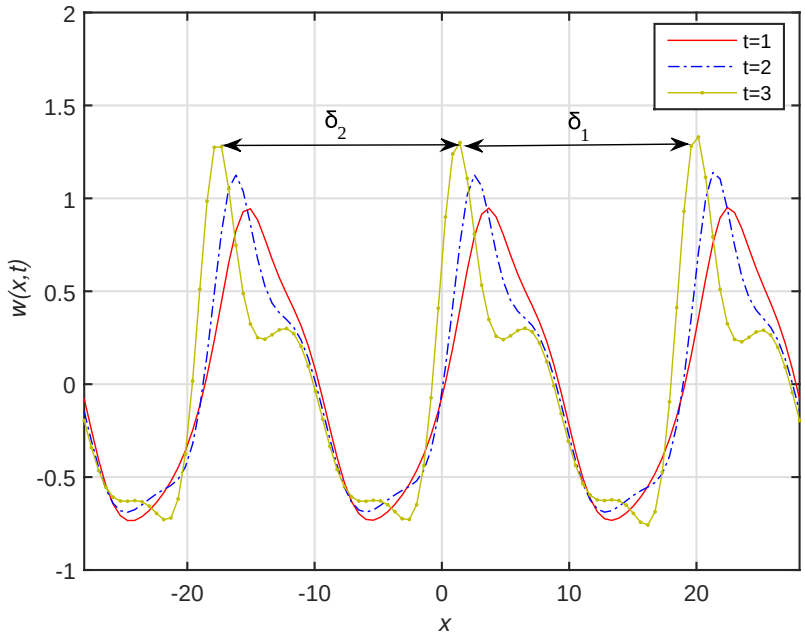

Figure 4.26: Formation of a three-pulse regime from the initial condition (4.34). The snapshots are for $t = 1$ to 3.

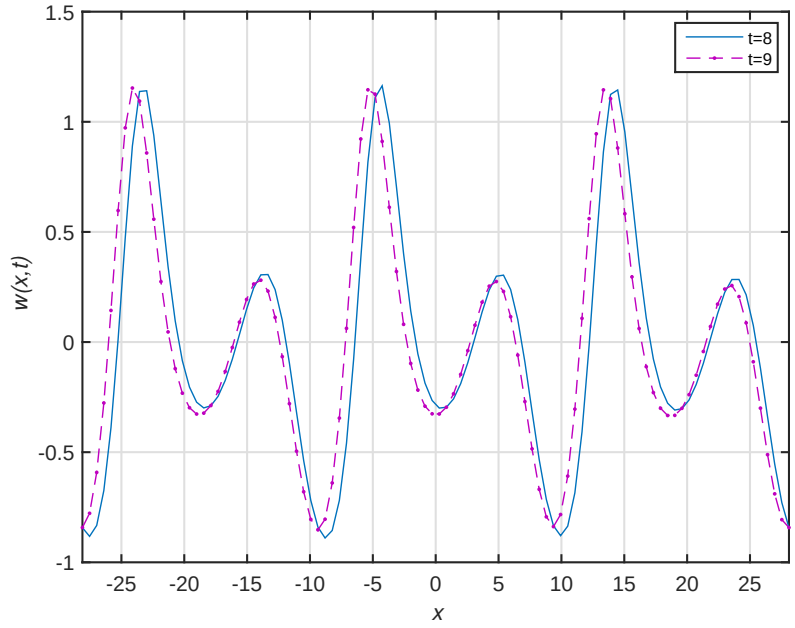

Figure 4.27: The snapshots are for $t = 8, 9$.

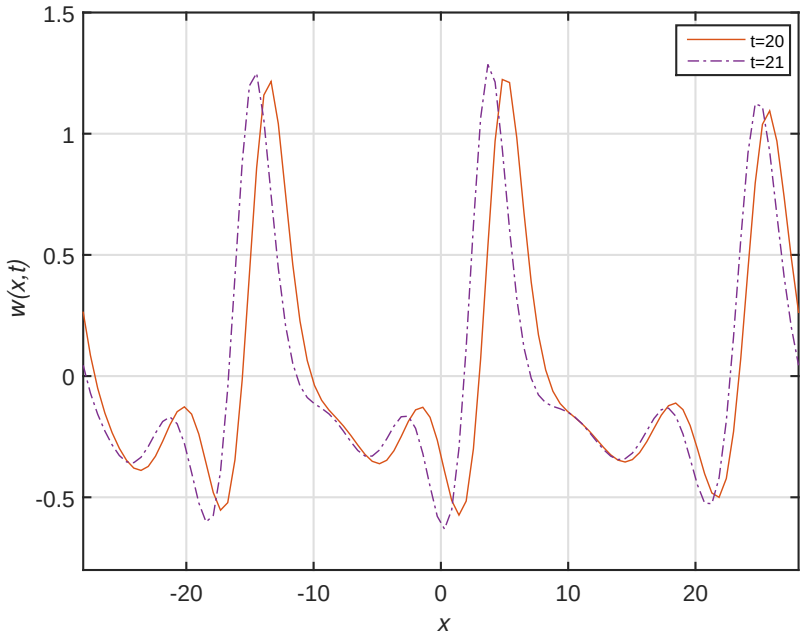

Figure 4.28: The solution evolved from the initial condition (4.34). The snapshots are for $t = 20, 21$.

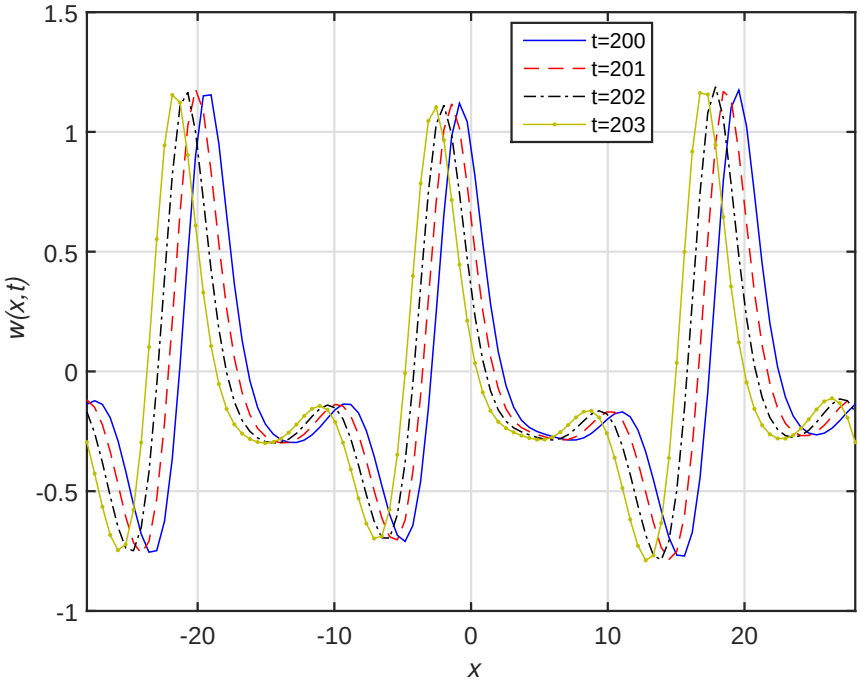

Figure 4.29: Continuation from Fig. 4.28, $t = 200$ to 203 .

We measured the distance δ_1 between the leading pulse 1 and the following pulse 2 and the distance δ_2 between the latter and the following pulse 3. Eventually an oscillatory regime settles as shown in Fig 4.30. The average values about which the oscillations occur, are $\delta_1 = 17$ and $\delta_2 = 19$. Taking into account the period $L = 56.2$, the pulse 3 – pulse 1 separation equals $\delta_3 = 56.2 - 17 - 19 = 20.2$. Thus, the separation of the pulses over the length of the period is not uniform unlike in the previous case of two pulses.

In general, this is an expected dynamic as multiple-pulse formations inevitably incur interaction of pulses via their tails. The more pulses are seeded within one period L and the larger the period, the more non-uniform dynamics may be expected. However, one should bear in mind that any artificial or real artery has limited length; it is bounded by branching points where special boundary conditions need to replace our conditions of periodicity. We leave this issue outside of the scope of this study.

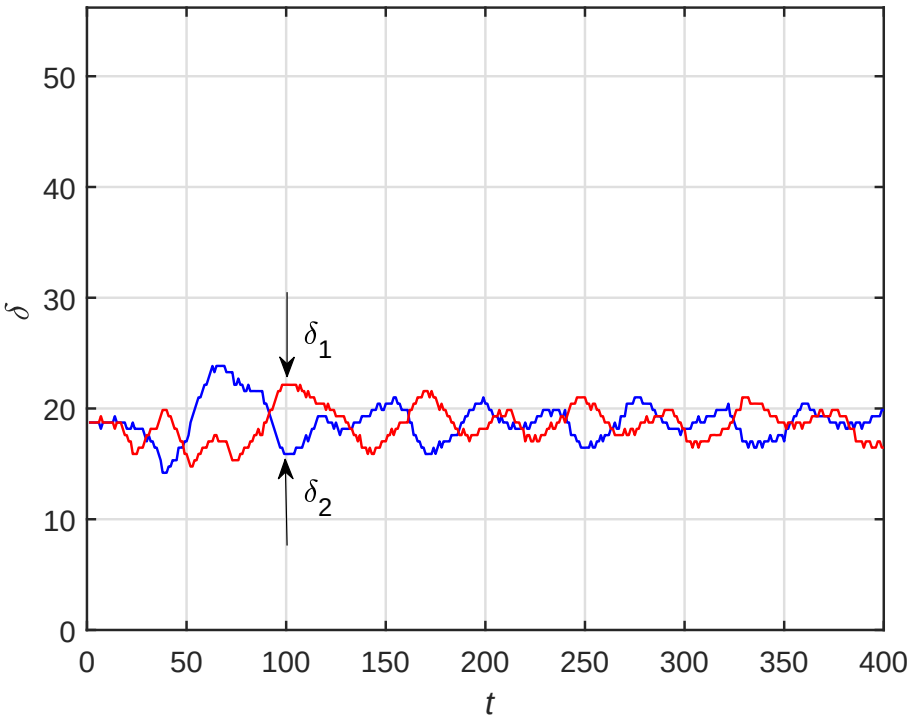

Figure 4.30: The evolution of the distance between three pulses. The period $L = 56.2$.

We also conducted experiments with the E-containing terms included and the results are very close to those for the equation without these terms.

4.4 Conclusion

We presented numerical solutions of the model describing auto-pulses in a single channel simulating an artificial artery with active elastic walls. Viscosity plays dominant role over inertia in the model. For simplicity we adopted an unbounded plain channel geometry and smallness of the wall deflection. We demonstrated the process of formation of a pulse from an arbitrary initial condition. Subject to spatially periodic boundary conditions, the system generates regimes with one, two or more pulses within one spatial period. We investigated the time-dependence of the dis-

tance between adjacent pulses in a two-pulse regime and detected small sustained fluctuations. Three-pulse regimes are also explored. The numerical experiments show slight non-uniformity of the average pulse separation and the presence of relatively small fluctuations.

Chapter 5

Evaluation of phenomenological parameters. Mass flux

5.1 Introduction

In the previous chapter, a variety of pulse solutions is obtained using periodic boundary conditions. The dynamics of one, two and three pulses per period are explored. The main purpose of this chapter is to calculate the fluid mass flux due to the pulses. Also, using the values of mechanical parameters from literature, we evaluate the empirical coefficients of the model responsible for the active motion of the walls.

5.2 Mass flux

We need to demonstrate that the self-motion of the walls facilitates a non-zero average max flux of the fluid. With the walls moving back and forth, it is not a priori obvious that such flux is non-zero. As the pulse moves to the left, some amount of the fluid also gets transferred in the same direction but some amount will go back

after the pulse is gone. We need to show that the amount of the fluid moving to the left is larger than the amount coming back. To show that we calculate the mass flux through the cross-section of the channel based on the obtained periodic solution of the first experiment in Section 4.3.2. We note that integrating a travelling wave as a function of $\xi = x + \lambda t$ over one period in time, T, is equivalent to integrating over one period in space, so we will replace dt by dx/λ, where λ is the wave speed. Using (2.12), the instantaneous flux equals

$$Q = H\frac{\partial u}{\partial t} - \frac{H^3}{3\eta}\frac{\partial p}{\partial x}\,.$$

We substitute in here the following expressions:

$$p = D\frac{\partial^4 w}{\partial x^4} - \alpha w^4$$

from (2.22) and (2.23) (recall that for the short model (2.31), the E-term in (2.22) disappears), and

$$H\frac{\partial u}{\partial t} = -\beta H^3 w^5 + K$$

from (2.24), and

$$H = H_0 + w$$

from (2.33). As a result, the total flux over one period

$$\begin{aligned}\int_T Q\,dt &= \frac{1}{\lambda}\int_L \left[-\beta\left(H_0+w\right)^3 w^5 + K\right]\,dx - \frac{1}{3\eta\lambda}\int_L \left(H_0+w\right)^3\left[D\frac{\partial^5 w}{\partial x^5} - \alpha\frac{\partial}{\partial x}\left(w^4\right)\right]\,dx\\ &\approx -\frac{H_0^3\beta}{\lambda}\int_L\left(1+3\frac{w}{H_0}+\dots\right)w^5 dx + \frac{KL}{\lambda}\\ &\quad - \frac{H_0^3}{3\eta\lambda}\int_L\left[1+3\frac{w}{H_0}+3\left(\frac{w}{H_0}\right)^2+\dots\right]\left[D\frac{\partial^5 w}{\partial x^5} - \alpha\frac{\partial}{\partial x}\left(w^4\right)\right]\,dx\,. \qquad (5.1)\end{aligned}$$

Looking at the last integral in (5.1), we realize that, due to periodicity,

$$\int_L \frac{\partial^5 w}{\partial x^5}\,dx = 0\,, \quad \int_L \frac{\partial}{\partial x}\left(w^4\right)\,dx = 0\,.$$

Furthermore, integrating by parts,

$$\int_L w\cdot\frac{\partial^5 w}{\partial x^5}\,dx = 0\,, \quad \int_L w\cdot\frac{\partial}{\partial x}\left(w^4\right)\,dx = 0\,.$$

Consequently, the input from the last integral in (5.1), representing the input from the pressure gradient, is quadratic in small "parameter" w/H_0. Let us show that the input from the shear stress is linear in w/H_0 and, therefore, makes major contribution into the flux. First, we need to determine K from the condition of zero displacement of the wall after one period. We are going to integrate $\partial u/\partial t$ and require that the total change of u over one period be zero. While u is measured in cm, it does not represent a displacement of any particular physical particle, but measures the amount of different particles that pass by the location x during one period. Zero total change of u requires that all the particles of the wall that moved from the left to the right come back from the right to the left by the end of one period. This process is illustrated below in Figs. 5.1–5.19 and also in (x,t)-plane in Fig. 5.20. Using (2.30) we have

$$0 = \int_T \frac{\partial u}{\partial t}\,dt = \frac{1}{\lambda}\int_L \left[-(H_0+w)^2\beta w^5 + \frac{K}{H_0+w}\right] dx$$

$$\approx \frac{1}{\lambda}\int_L \left[-H_0^2\left(1+2\frac{w}{H_0}+\dots\right)\beta w^5 + \frac{K}{H_0}\left(1-\frac{w}{H_0}+\dots\right)\right] dx\,.$$

Up to the linear terms in w/H_0,

$$K = \frac{H_0^3\beta\left[\int_L w^5\,dx + 2\int_L\left(\frac{w}{H_0}\right)w^5\,dx+\dots\right]}{L\left[1-\frac{1}{L}\int_L\left(\frac{w}{H_0}\right)\,dx+\dots\right]}$$

$$= \frac{H_0^3\beta}{L}\left[\int_L w^5\,dx + 2\int_L\left(\frac{w}{H_0}\right)w^5\,dx+\dots\right]\left[1+\frac{1}{L}\int_L\left(\frac{w}{H_0}\right)\,dx+\dots\right]$$

$$\approx \frac{H_0^3\beta}{L}\int_L w^5\,dx + \frac{2H_0^3\beta}{L}\int_L\left(\frac{w}{H_0}\right)w^5\,dx + \frac{H_0^3\beta}{L^2}\left(\int_L w^5\,dx\right)\cdot\left(\int_L\frac{w}{H_0}\,dx\right).$$

As a result,

$$\int_T Q\,dt \approx -\frac{H_0^2\beta}{\lambda}\int_L w^6\,dx + \frac{H_0^2\beta}{\lambda L}\left(\int_L w^5\,dx\right)\cdot\left(\int_L w\,dx\right).$$

The dynamics of the horizontal displacement u according to the equation

$$\frac{\partial u}{\partial t} = -H_0^3\beta w^5 + K \tag{5.2}$$

are shown in Figs. 5.1–5.19.

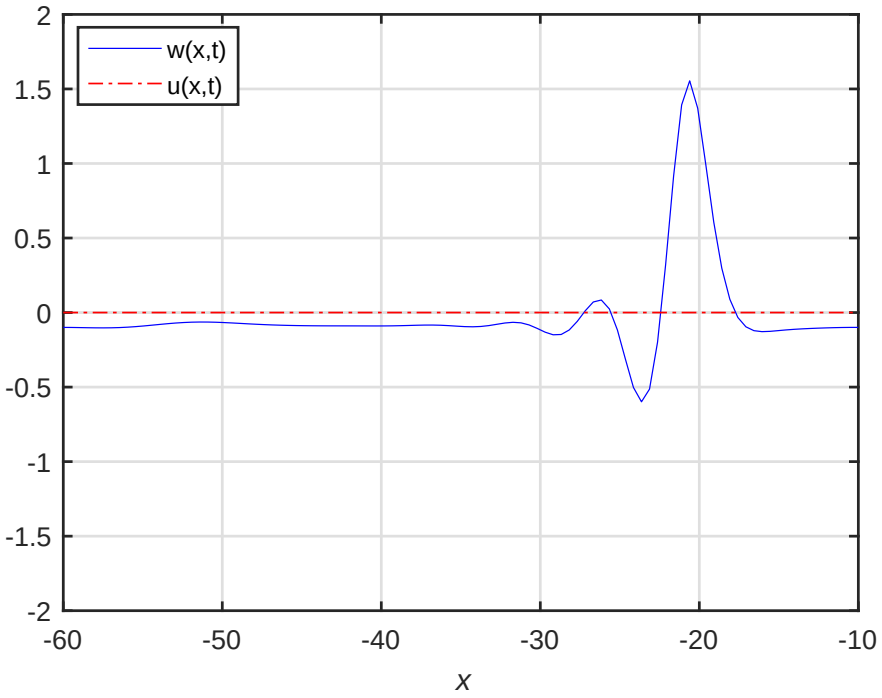

Figure 5.1: The initial conditions for equation (5.2): the settled pulse for w and the zero displacement for u.

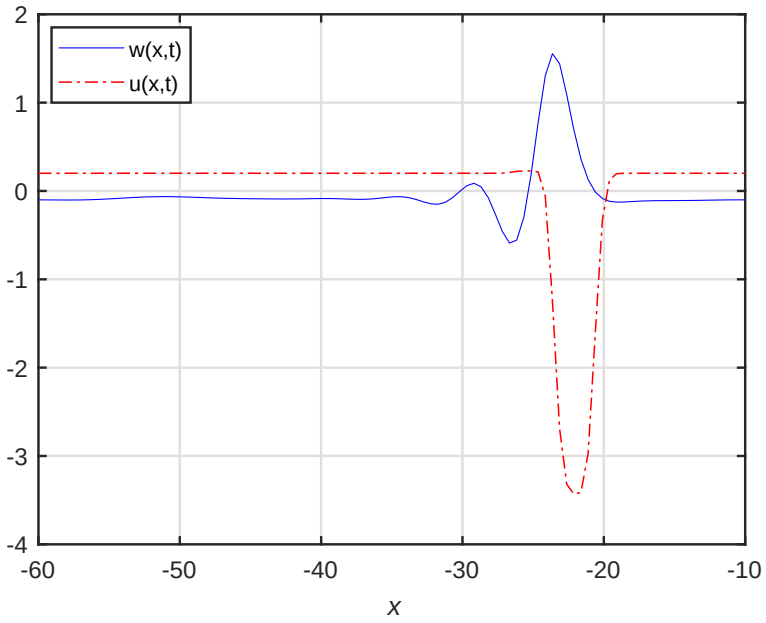

Figure 5.2: Continuation from Fig. 5.1, $t = 1$.

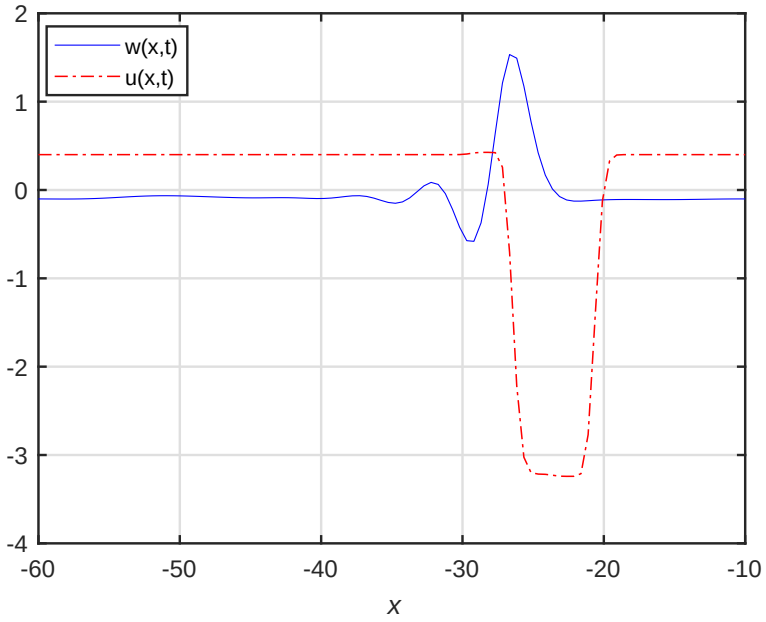

Figure 5.3: Continuation from Fig. 5.2, $t = 2$.

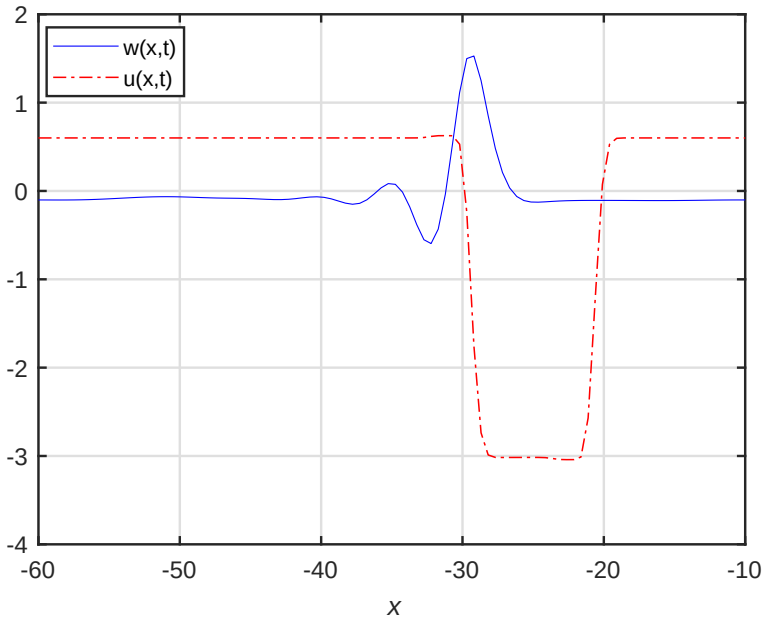

Figure 5.4: Continuation from Fig. 5.3, $t = 3$.

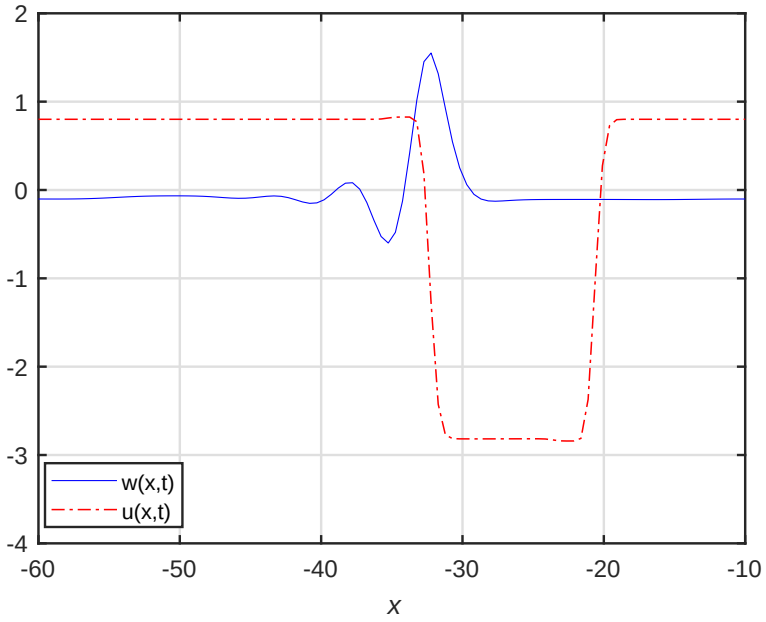

Figure 5.5: Continuation from Fig. 5.4, $t = 4$.

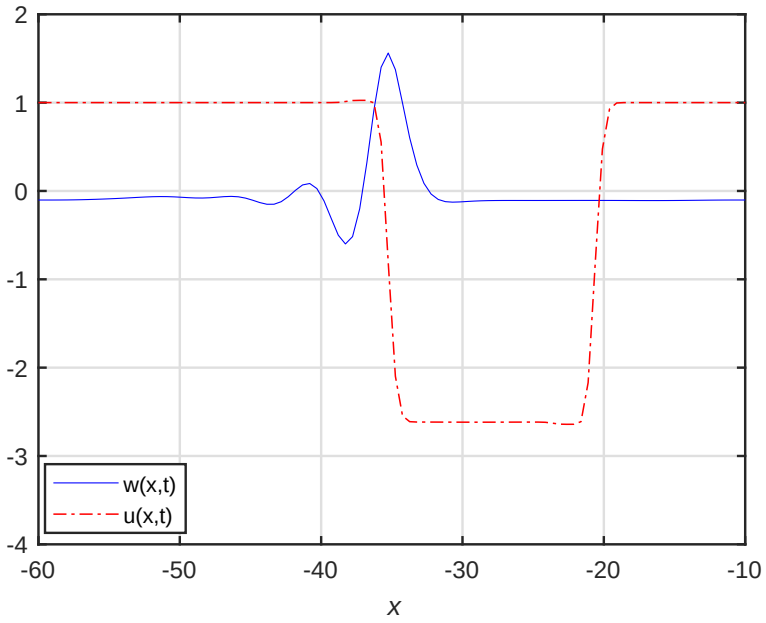

Figure 5.6: Continuation from Fig. 5.5, $t = 5$.

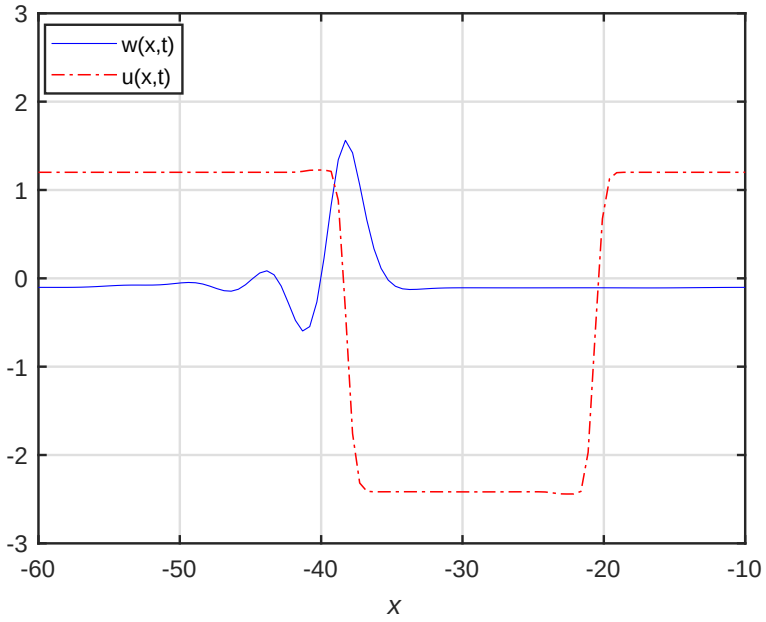

Figure 5.7: Continuation from Fig. 5.6, $t = 6$.

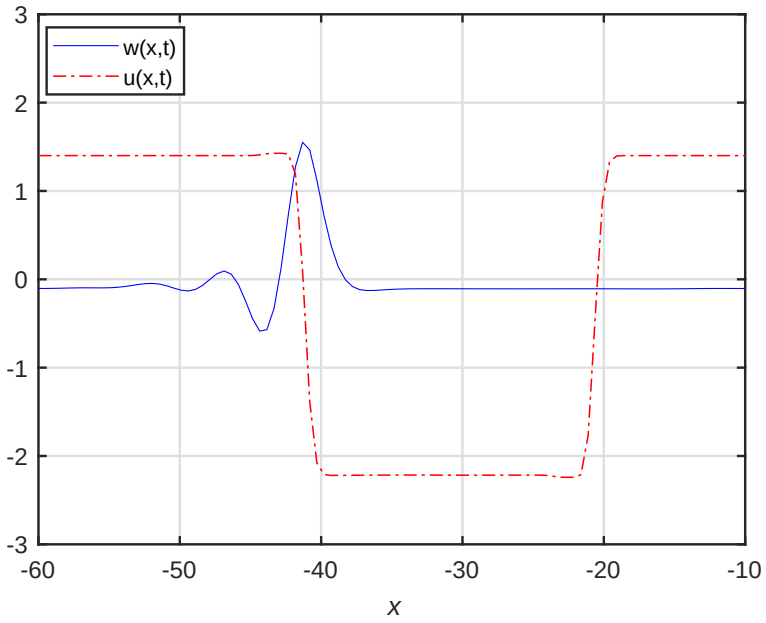

Figure 5.8: Continuation from Fig. 5.7, $t = 7$.

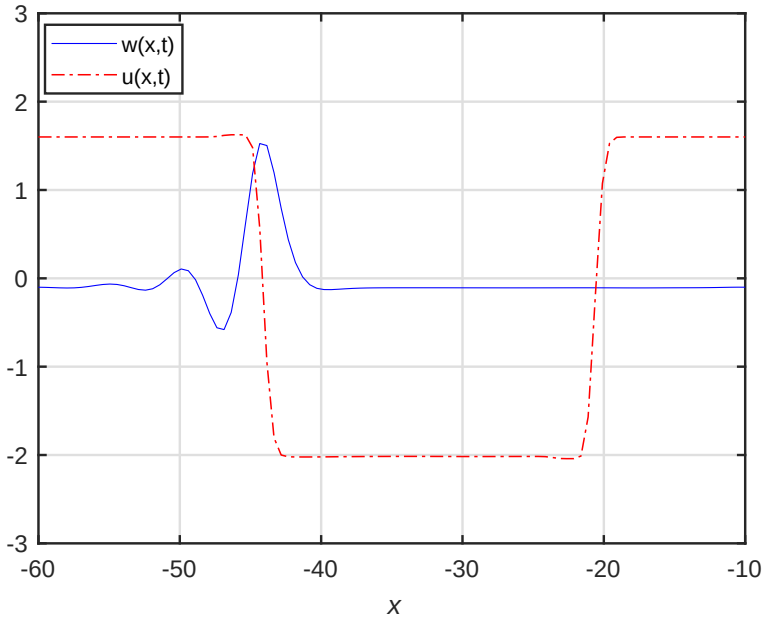

Figure 5.9: Continuation from Fig. 5.8, $t = 8$.

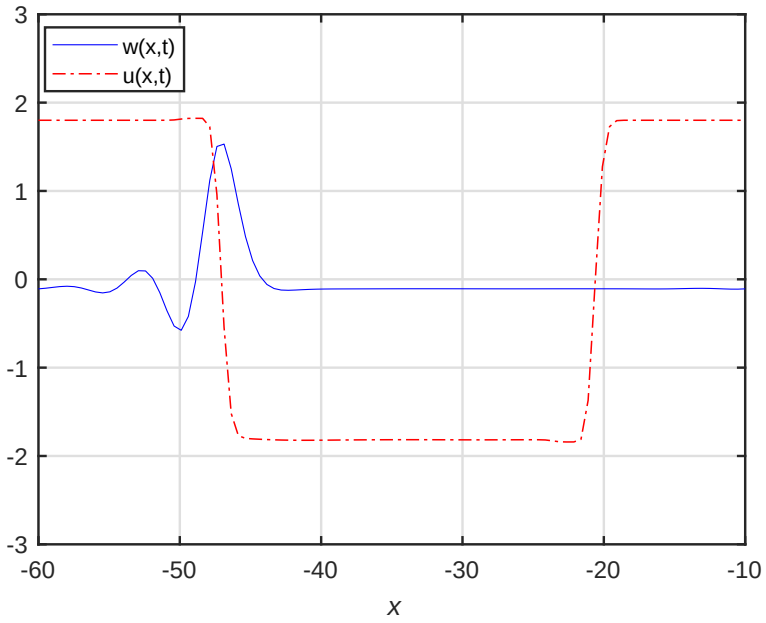

Figure 5.10: Continuation from Fig. 5.9, $t = 9$.

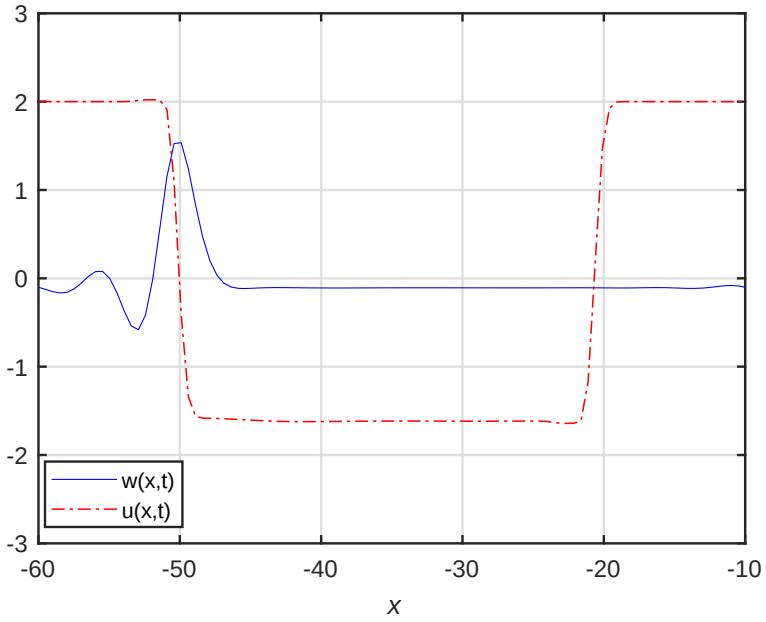

Figure 5.11: Continuation from Fig. 5.10, $t = 10$.

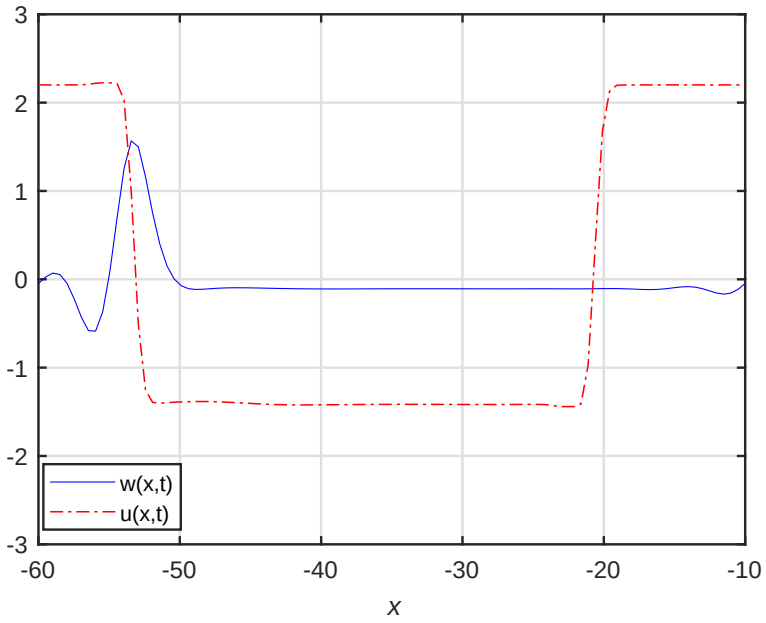

Figure 5.12: Continuation from Fig. 5.11, $t = 11$.

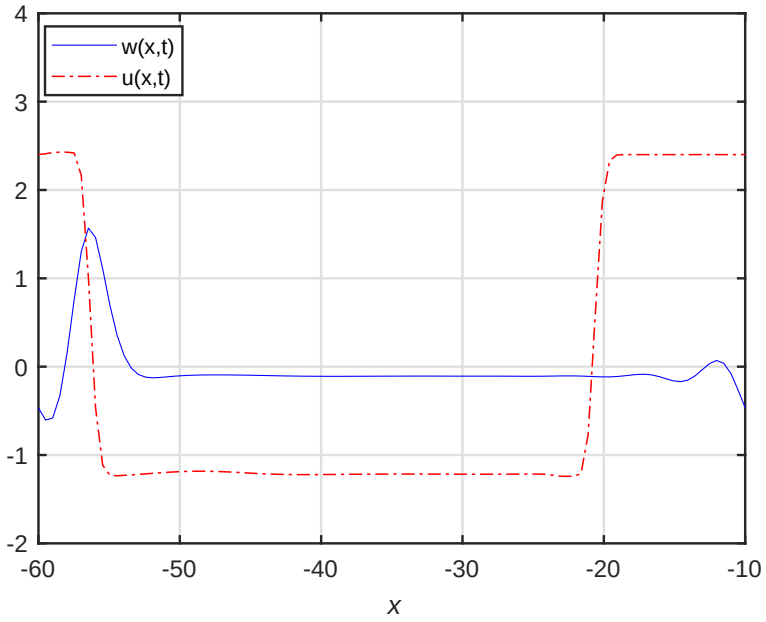

Figure 5.13: Continuation from Fig. 5.12, $t = 12$.

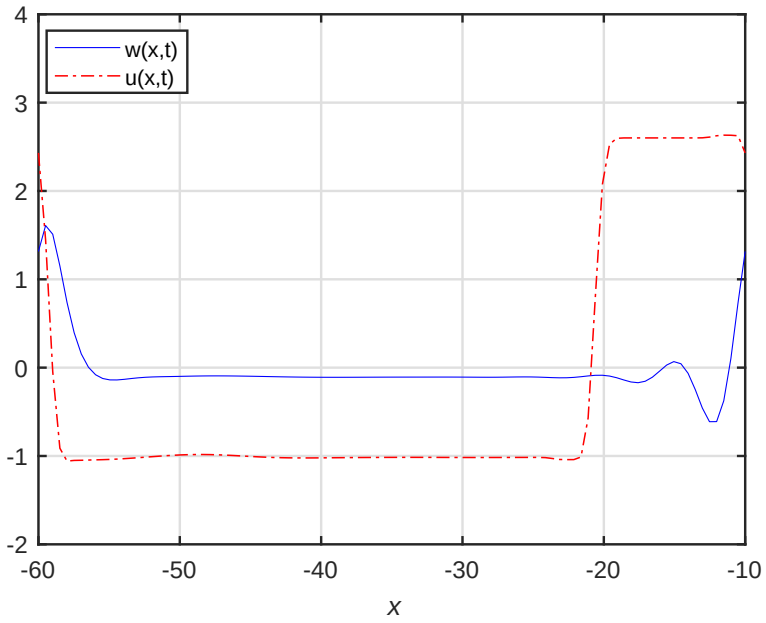

Figure 5.14: Continuation from Fig. 5.13, $t = 13$.

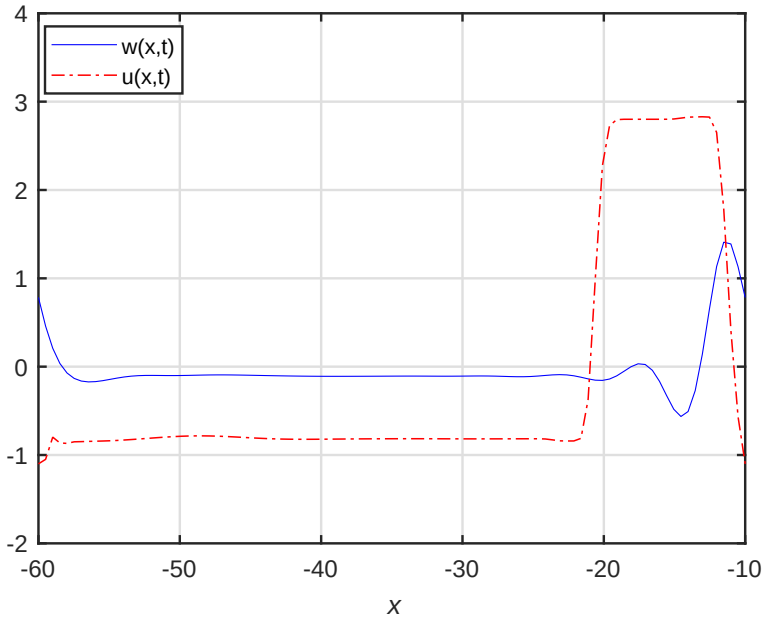

Figure 5.15: Continuation from Fig. 5.14, $t = 14$.

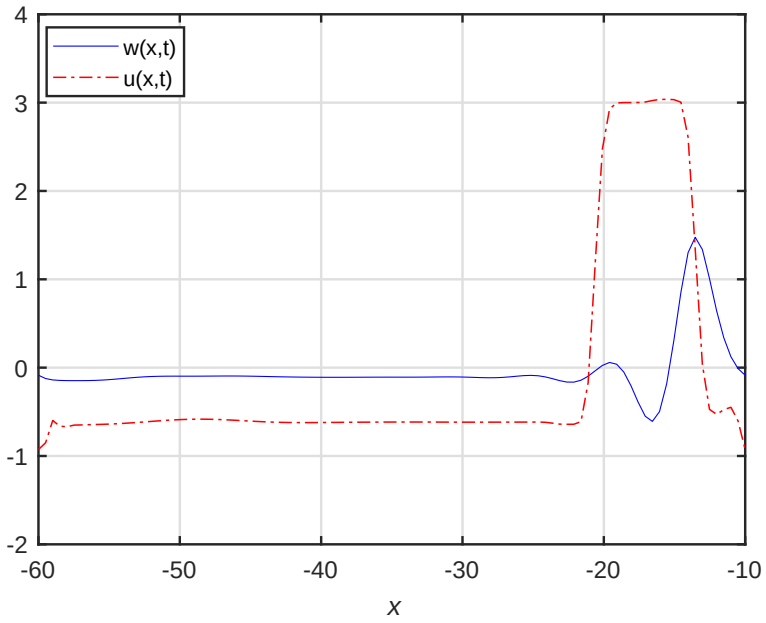

Figure 5.16: Continuation from Fig. 5.15, $t = 15$.

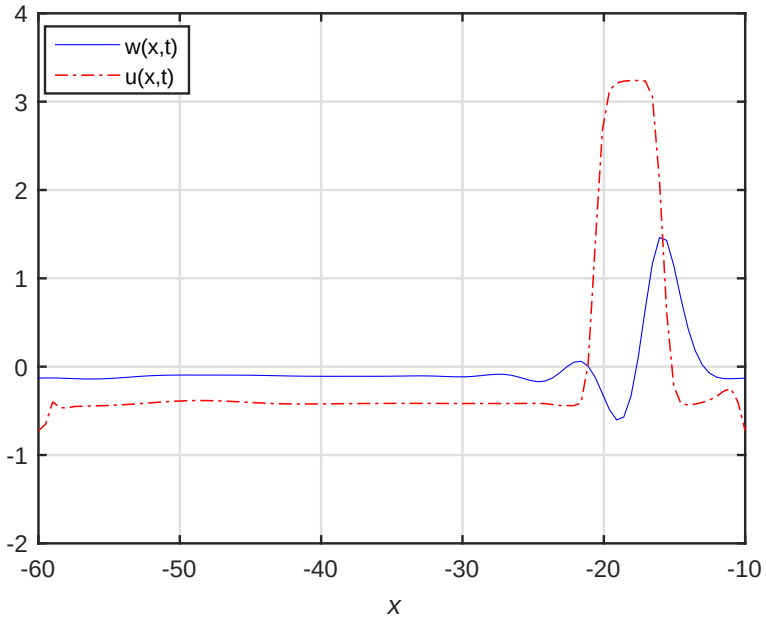

Figure 5.17: Continuation from Fig. 5.16, $t = 16$.

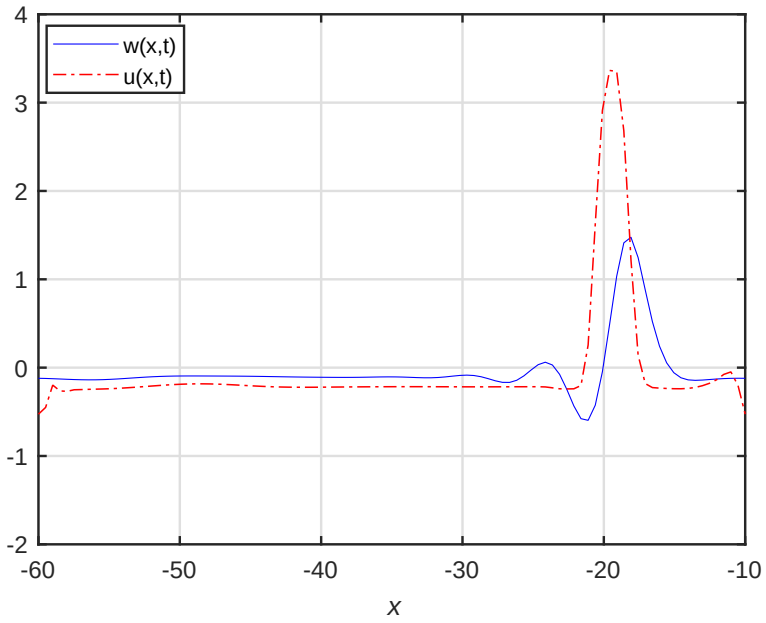

Figure 5.18: Continuation from Fig. 5.17, $t = 17$.

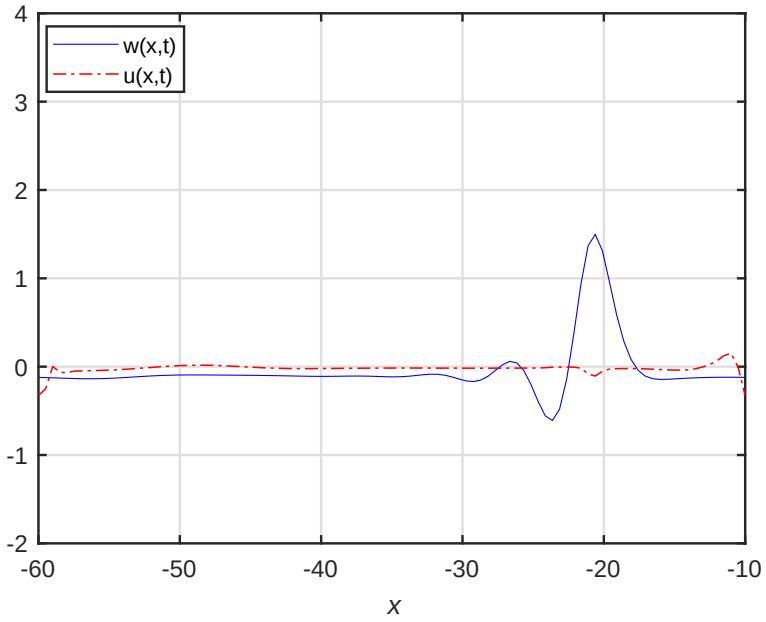

Figure 5.19: Continuation from Fig. 5.18, $t = 18$.

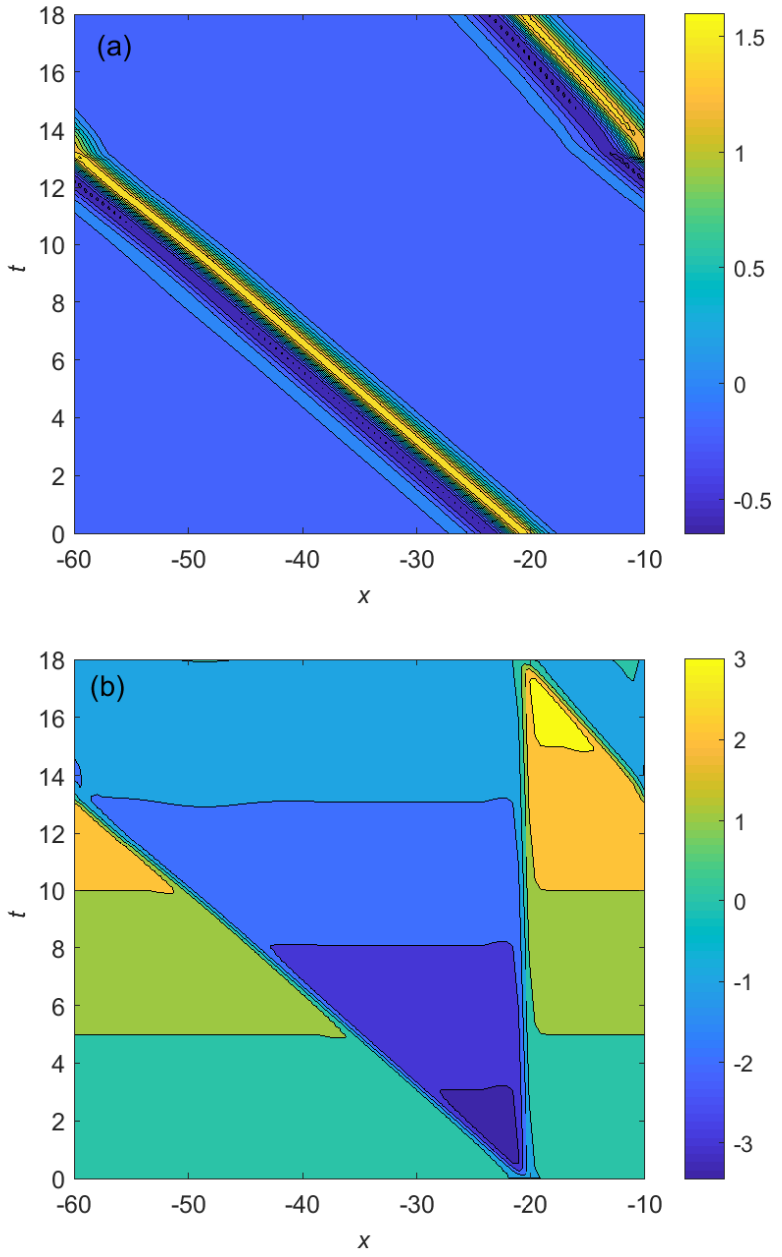

Figure 5.20: Numerical results from: (a) Eq. (4.3) and (b) Eq. (5.2) in the (x, t)-plane over one period ($0 \leq t \leq 18$). The initial conditions are chosen to be the settled pulse for w and the zero displacement for u. The pulse is moving from the right to the left. The u-plot shows rapid motion of the wall to the left followed by its slow return to the original position.

Observe that at each location x the wall quickly moves to the left with the pulse during its immediate passage and then slowly returns to its original position. For the shown experiment, taking into account $L = 50$, we calculate

$$\int_L w^6\,dx = 12.4, \quad \int_L w^5\,dx = 8.9, \quad \int_L w\,dx = -2.0\,,$$

giving

$$\frac{\lambda}{H_0^2\beta}\int_L Q\,dt = -\int_L w^6\,dx + \frac{1}{L}\left(\int_L w^5\,dx\right)\left(\int_L w\,dx\right) = -12.7\,. \tag{5.3}$$

An important thing is that that the flux is non-zero and negative. In support of this result, in the Appendix D we present an evaluation of the flux based on a simplified step-like sketch of the pulse.

5.3 Evaluation of the model coefficients

In this section, we evaluate the coefficients α and β, which were introduced in the original model (Strunin, 2009*a*) empirically. Let us re-scale the main dimensional equation (4.2) in two steps. In step one, we non-dimensionalize the equation using H_0 as the spatial scale and η/E as the time scale. Then, in step two, we re-scale w, t and x using the yet-to-be-determined non-dimensional scaling factors W, T and X, respectively. Thus,

$$w = H_0 w_{1p}\,, \quad w_{1p} = W w_{2p}\,,$$

$$x = H_0 x_{1p}\,, \quad x_{1p} = X x_{2p}\,,$$

$$t = \eta t_{1p}/E\,, \quad t_{1p} = T t_{2p}\,.$$

The resulting non-dimensional equation is

$$\frac{\partial w_{2p}}{\partial t_{2p}} = A\frac{\partial^6 w_{2p}}{\partial x_{2p}^6} - B\frac{\partial^2}{\partial x_{2p}^2}\left(w_{2p}^4\right) + C\frac{\partial}{\partial x_{2p}}\left(w_{2p}^5\right)\,, \tag{5.4}$$

where

$$A = \frac{DT}{3EH_0^3X^6}\,, \quad B = \frac{\alpha H_0^4 TW^3}{3EX^2}\,, \quad C = \frac{\beta\eta H_0^6 TW^4}{EX}\,. \tag{5.5}$$

In fact, (5.4) is the non-dimensional equation (4.3) which we solved numerically. In the numerical experiments we used

$$A = 1\,, \quad B = 1\,, \quad C = 1\,. \tag{5.6}$$

Using the single-pulse solution in Chapter 4 (Fig. 4.12), we can measure the non-dimensional amplitude of the pulse Δw_{2p} and the non-dimensional pulse speed $\Delta x_{2p}/\Delta t_{2p}$. Returning to the dimensional quantities, we have, for the dimensional pulse amplitude,

$$\Delta w = H_0 W \Delta w_{2p} \tag{5.7}$$

and, for the dimensional pulse speed,

$$v = \frac{\Delta x}{\Delta t} = \frac{H_0 X E}{\eta T} \frac{\Delta x_{2p}}{\Delta t_{2p}}\,. \tag{5.8}$$

We require that the coefficients α and β lead to realistic orders of magnitude for Δw and v in (5.7)–(5.8). Of course we remember that our hypothetical channels do not have realistic cylindrical shape, but the methodology of evaluation of α and β is applicable to any version of the model including possible future versions with cylindrical configuration. From the literature, by the order of magnitude, $v = 4\,\mathrm{m/s}$ (London and Pannier, 2010; Lehmann, 1999), and $\Delta w = 0.001\,\mathrm{m}$. The three equations (5.6) (where A, B and C are given by (5.5)) and equations (5.7) and (5.8) form a system of five equations with respect to the five parameters W, X, T, α and β that are to be determined. We find

$$W = \left(\frac{\Delta w}{\Delta w_{2p}}\right) H_0^{-1}\,,$$

$$X = D^{1/5}(3\eta)^{-1/5}\, v^{-1/5} H_0^{-2/5} \left(\frac{\Delta x_{2p}}{\Delta t_{2p}}\right)^{1/5}\,,$$

$$T = E D^{1/5} H_0^{3/5}\, 3^{-1/5}\, (v\eta)^{-6/5} \left(\frac{\Delta x_{2p}}{\Delta t_{2p}}\right)^{6/5}\,,$$

$$\alpha = H_0^{-12/5} \left(\frac{\Delta x_{2p}}{\Delta t_{2p}}\right)^{-4/5} D^{1/5}(3\eta)^{4/5} \left(\frac{\Delta w_{2p}}{\Delta w}\right)^{3} v^{4/5}\,,$$

$$\beta = \left(\frac{\Delta x_{2p}}{\Delta t_{2p}}\right)^{-1} \left(\frac{\Delta w_{2p}}{\Delta w}\right)^{4} v\, H_0^{-3}\,.$$

As we noted, $\Delta x_{2p}/\Delta t_{2p}$ and Δw_{2p} are measured from the numerical experiments (Fig. 4.12): $\Delta x_{2p}/\Delta t_{2p} = 2.53$ and $\Delta w_{2p} = 2.1$ approximately. The other parameters have the following approximate values: $H_0 = 0.005\,\mathrm{m}$, the Young's modulus $E = 3 \times 10^5\,\mathrm{Pa}$ (Zhang et al., 2005), the Poisson ratio $\nu = 0.5$ (Olufsen et al., 2000; Matthys et al., 2007; Surovtsova, 2005; Avolio, 1980; Kalita, 2004; Quarteroni et al., 2000), the blood viscosity $\eta = 0.004\,\mathrm{Pa}\cdot\mathrm{s}$ (Avolio, 1980) and the wall thickness $h = 0.001\,\mathrm{m}$ (Quarteroni et al., 2000) . Therefore, the flexural rigidity $D = Eh^3/[12(1-\nu^2)] = 3.3\times10^{-5}\,\mathrm{Pa}\cdot\mathrm{m}^3$. Based on these figures, we have, by the order of magnitude,

$$\alpha = 1.6 \times 10^{13}\,\mathrm{Pa}\cdot\mathrm{m}^{-4}$$

and

$$\beta = 2.5 \times 10^{20}\,\mathrm{m}^{-6}\cdot\mathrm{s}^{-1}\,.$$

5.4 Conclusion

The fluid mass flux carried out by the pulse is calculated. Based on the numerical results, we evaluated the empirical parameters α and β responsible for the active component of the wall dynamics.

Chapter 6

Auto-pulses in a branching channel flow with active elastic boundaries

6.1 Introduction

Branching flow is extremely interesting topic in its own right and in this chapter we study it both theoretically and numerically. The arterial systems are characterised by branching with a network of larger arteries splitting into smaller arteries which continue to bifurcate into arterioles and then into the capillaries. Therefore we are interested in simulation of branching pulses in our theoretical model. We emphasize again that this model simulates an *artificial* artery with *active* walls. Our goal in this chapter is to determine the conditions that ensure that a pulse propagating through a thick channel "survives" when the channel subdivides into two thinner channels. In other words, we want the model to be self-consistent that is to have characteristics that guarantee the propagation of the pulses over the entire system of branching channels (Strunin and Ahmed, 2019). The main equation describing pulses in each

channel is,

$$\frac{\partial w}{\partial t} = \frac{D}{3\eta}\frac{\partial}{\partial x}\left[H^3\frac{\partial^5 w}{\partial x^5}\right] - \frac{\alpha}{3\eta}\frac{\partial}{\partial x}\left[H^3\frac{\partial}{\partial x}\left(w^4\right)\right] + \beta\frac{\partial}{\partial x}\left(H^3 w^5\right) , \tag{6.1}$$

where H is the width of the given channel and α and β may generally differ between the channels. Assuming $w << H_0$ and replacing H by $H = H_0 + w \approx H_0$ in Eq. (6.1) we get

$$\frac{\partial w}{\partial t} = \frac{D}{3\eta}H_0^3\frac{\partial^6 w}{\partial x^6} - \frac{1}{3\eta}\alpha H_0^3\frac{\partial^2}{\partial x^2}\left(w^4\right) + H_0^3\beta\frac{\partial}{\partial x}\left(w^5\right) . \tag{6.2}$$

This chapter is organised as follows. Section 6.3 presents the numerical approach. This is then followed by the discussion of numerical results in Section 6.3. Conclusions are given in Section 6.4.

6.2 Numerical approach: One-dimensional Integrated Radial Basis Function Networks

To solve the model numerically we used the One-dimensional Integrated Radial Basis Function Network (1D-IRBFN) method in conjunction with one-step Picard iteration (PI1) scheme (Ahmed et al., 2016).

In the 1D-IRBFN method the highest-order derivative, 6^{th} order, is approximated by radial basis functions. The lower-order derivatives and function itself are then obtained by integration. The purpose of using integration instead of conventional differentiation to construct the RBF approximations is to improve the stability and accuracy of the numerical solution. The integration process naturally gives rise to arbitrary constants that serve as additional expansion coefficients. Therefore, the constants facilitate the employment of some extra equations in the process of converting the RBF weights into the function values, which helps in the implementation of multiple boundary conditions. The RBFs yield better accuracy, are easy to implement and have the capability to provide a very accurate solution using relatively low

numbers of grid points. The so-called multiquadric (MQ) functions were found to be the most efficient basis function to use in the method (Mai-Duy and Tran-Cong, 2001*a*). It was found that the MQ functions yield more accurate results in comparison with other radial basis functions (Franke, 1982; Haykin, 1999). The following section presents the numerical results.

6.3 Numerical results and discussion

6.3.1 Two-channel experiment

In this numerical experiment we consider a thick channel branching into two thin channels as shown in Fig. 6.1. In the state of rest each of the thin channels has half the width of the thick channel.

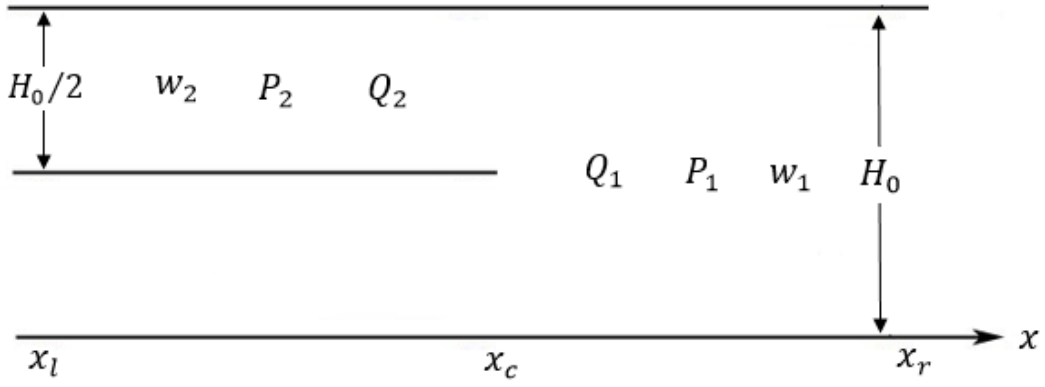

Figure 6.1: Branching channels (in the state of rest).

The displacements of the channel walls satisfy the equations

$$\frac{\partial w_1}{\partial t} = \frac{D}{3\eta} H_0^3 \frac{\partial^6 w_1}{\partial x^6} - \frac{\alpha_1}{3\eta} H_0^3 \frac{\partial^2}{\partial x^2} \left(w_1^4\right) + \beta_1 H_0^3 \frac{\partial}{\partial x} \left(w_1^5\right), \tag{6.3}$$

$$\frac{\partial w_2}{\partial t} = \frac{D}{3\eta}\left(\frac{H_0}{2}\right)^3 \frac{\partial^6 w_2}{\partial x^6} - \frac{\alpha_2}{3\eta}\left(\frac{H_0}{2}\right)^3 \frac{\partial^2}{\partial x^2}\left(w_2^4\right) + \beta_2\left(\frac{H_0}{2}\right)^3 \frac{\partial}{\partial x}\left(w_2^5\right), \qquad (6.4)$$

where we assume that the parameters α_i (and β_i) may be different between the channels. The boundary conditions are chosen homogeneous, namely zero values of the function and its first two derivatives at the edges, $x = x_l$ (l stands for "left") and $x = x_r$ (r stands for "right"),

$$w_1(x_r) = 0, \quad \frac{\partial w_1}{\partial x}(x_r) = 0, \quad \frac{\partial^2 w_1}{\partial x^2}(x_r) = 0\,,$$

$$w_2(x_l) = 0, \quad \frac{\partial w_2}{\partial x}(x_l) = 0, \quad \frac{\partial^2 w_2}{\partial x^2}(x_l) = 0\,.$$

In the experiments we used $x_r = 0$ and $x_l = -45$ (see Figs. 6.2-6.10). For the branching (contact) point the following boundary conditions are set. The kinematic condition expresses continuity of the wall displacement,

$$w_1(x_c) = w_2(x_c)\,, \qquad (6.5)$$

where c stands for "contact", see Fig. 6.1. The next conditions ensure continuity of the pressure (see (2.16)),

$$\begin{aligned} &\frac{\partial w_1}{\partial x}(x_c) = \frac{\partial w_2}{\partial x}(x_c)\,, \quad &&\frac{\partial^2 w_1}{\partial x^2}(x_c) = \frac{\partial^2 w_2}{\partial x^2}(x_c)\,, \\ &\frac{\partial^3 w_1}{\partial x^3}(x_c) = \frac{\partial^3 w_2}{\partial x^3}(x_c)\,, \quad &&\frac{\partial^4 w_1}{\partial x^4}(x_c) = \frac{\partial^4 w_2}{\partial x^4}(x_c)\,. \end{aligned} \qquad (6.6)$$

We used $x_c = -25$ (see Figs. 6.2-6.10). The last condition will ensure continuity of the mass flux. According to (2.12), the flux for the thick channel is

$$Q_1 = -\frac{H_0^3}{3\eta}\frac{\partial p_1}{\partial x} + v_1(x, H_0, t)\, H_0\,. \qquad (6.7)$$

As the width of the thin channel is $H_0/2$, from Eq. (6.7) the mass flux for the thin channel is

$$Q_2 = -\frac{(H_0/2)^3}{3\eta}\frac{\partial p_2}{\partial x} + v_2\left(x, \frac{H_0}{2}, t\right)\frac{H_0}{2}\,. \qquad (6.8)$$

Thy continuity of the flux requires

$$Q_1 = 2Q_2\,. \qquad (6.9)$$

Therefore, using (6.7), (6.8) we get

$$-\frac{(H_0/2)^3}{3\eta}\frac{\partial p_2}{\partial x}+v_2\left(x,\frac{H_0}{2},t\right)\ \frac{H_0}{2}=-\frac{H_0^3}{6\eta}\frac{\partial p_1}{\partial x}+v_1\left(x,H_0,t\right)\ \frac{H_0}{2}\,. \tag{6.10}$$

Assuming continuity of the velocity in (6.10) we have

$$4\frac{\partial p_1}{\partial x}=\frac{\partial p_2}{\partial x}\,. \tag{6.11}$$

Substituting (2.22) into (6.11), we obtain

$$\begin{aligned}&4\left[D\frac{\partial^5 w_1(x_c)}{\partial x^5}-\frac{\partial^2}{\partial x^2}\left(N\frac{\partial w_1(x_c)}{\partial x}\right)-\alpha\frac{\partial}{\partial x}w_1^4(x_c)\right]\\&=\left[D\frac{\partial^5 w_2(x_c)}{\partial x^5}-\frac{\partial^2}{\partial x^2}\left(N\frac{\partial w_2(x_c)}{\partial x}\right)-\alpha\frac{\partial}{\partial x}w_2^4(x_c)\right],\end{aligned} \tag{6.12}$$

and, inserting (2.17) into (6.12),

$$\begin{aligned}&4\left[D\frac{\partial^5 w_1(x_c)}{\partial x^5}-\alpha\frac{\partial}{\partial x}w_1^4(x_c)\ -\frac{Eh}{1-\nu^2}\frac{\partial^2}{\partial x^2}\left(\frac{\partial u}{\partial x}\frac{\partial w_1(x_c)}{\partial x}+\frac{1}{2}\left(\frac{\partial w_1(x_c)}{\partial x}\right)^3\right)\right]\\&=\left[D\frac{\partial^5 w_2(x_c)}{\partial x^5}-\alpha\frac{\partial}{\partial x}w_2^4(x_c)\ -\frac{Eh}{1-\nu^2}\frac{\partial^2}{\partial x^2}\left(\frac{\partial u}{\partial x}\frac{\partial w_2(x_c)}{\partial x}+\frac{1}{2}\left(\frac{\partial w_2(x_c)}{\partial x}\right)^3\right)\right].\end{aligned} \tag{6.13}$$

Assuming u small and negligible the Eq. (6.13) becomes

$$\begin{aligned}&4D\frac{\partial^5 w_1(x_c)}{\partial x^5}-4\alpha\frac{\partial}{\partial x}w_1^4(x_c)-\frac{4Eh}{2(1-\nu^2)}\frac{\partial^2}{\partial x^2}\left(\frac{\partial w_1(x_c)}{\partial x}\right)^3\\&=D\frac{\partial^5 w_2(x_c)}{\partial x^5}-\frac{Eh}{2(1-\nu^2)}\frac{\partial^2}{\partial x^2}\left(\frac{\partial w_2(x_c)}{\partial x}\right)^3-\alpha\frac{\partial}{\partial x}w_2^4(x_c)\,.\end{aligned} \tag{6.14}$$

Using the conditions (6.5) and (6.6) in Eq. (6.14), we get

$$4D\frac{\partial^5 w_1(x_c)}{\partial x^5}-3\frac{Eh}{2(1-\nu^2)}\frac{\partial^2}{\partial x^2}\left(\frac{\partial w_1(x_c)}{\partial x}\right)^3-3\alpha\frac{\partial}{\partial x}w_1^4(x_c)=D\frac{\partial^5 w_2(x_c)}{\partial x^5}\,. \tag{6.15}$$

The size of spatial domain and number of nodes were chosen so as to ensure reasonable duration of each numerical experiment and satisfactory spatial resolution of the pulses. The number of nodes was 100, the time step 0.001, and the size of the

domain $x_r - x_l = 45$. In the first experiment, we assumed that $\alpha_2 = \alpha_1$ and $\beta_2 = \beta_1$. After non-dimensionalizing the thick channel equation to the form

$$\frac{\partial w_1}{\partial t} = \frac{\partial^6 w_1}{\partial x^6} - \frac{\partial^2}{\partial x^2}\left(w_1^4\right) + \frac{\partial}{\partial x}\left(w_1^5\right) \tag{6.16}$$

the non-dimensional thin channel equation becomes

$$\frac{\partial w_2}{\partial t} = a\frac{\partial^6 w_2}{\partial x^6} - b\frac{\partial^2}{\partial x^2}\left(w_2^4\right) + c\frac{\partial}{\partial x}\left(w_2^5\right) \ , \tag{6.17}$$

where $a = b = c = 1/8$. We set the initial condition in the thick channel as $w_1(x,0) = 1.2.\exp\left[-0.25(x+2.5)^2\right]$ and in the thin channel $w_2(x,0) = 0$ as shown in Fig. 6.2.

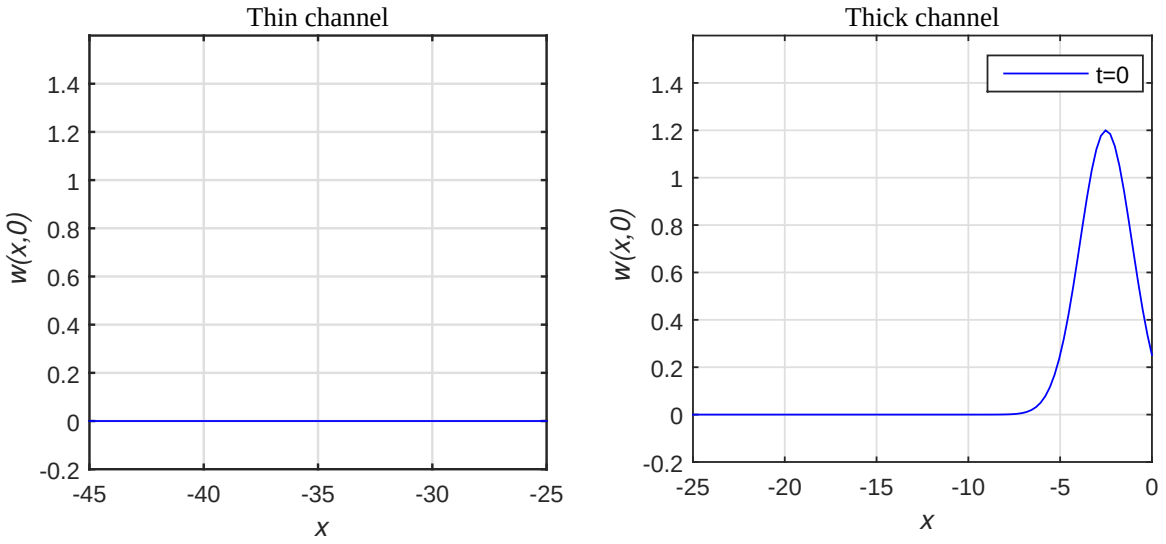

Figure 6.2: The initial condition initiating the pulse in the thick channel.

From Fig. 6.3, we see that in this particular experiment the pulse in the thick channel is not propagating to the thin channel. In the second experiment, in an attempt to make the pulse propagate into the thin channel we increased the value of β_2 (the thin channel parameter) by the factor of eight ($a = 1/8, b = 1/8, c = 1$).

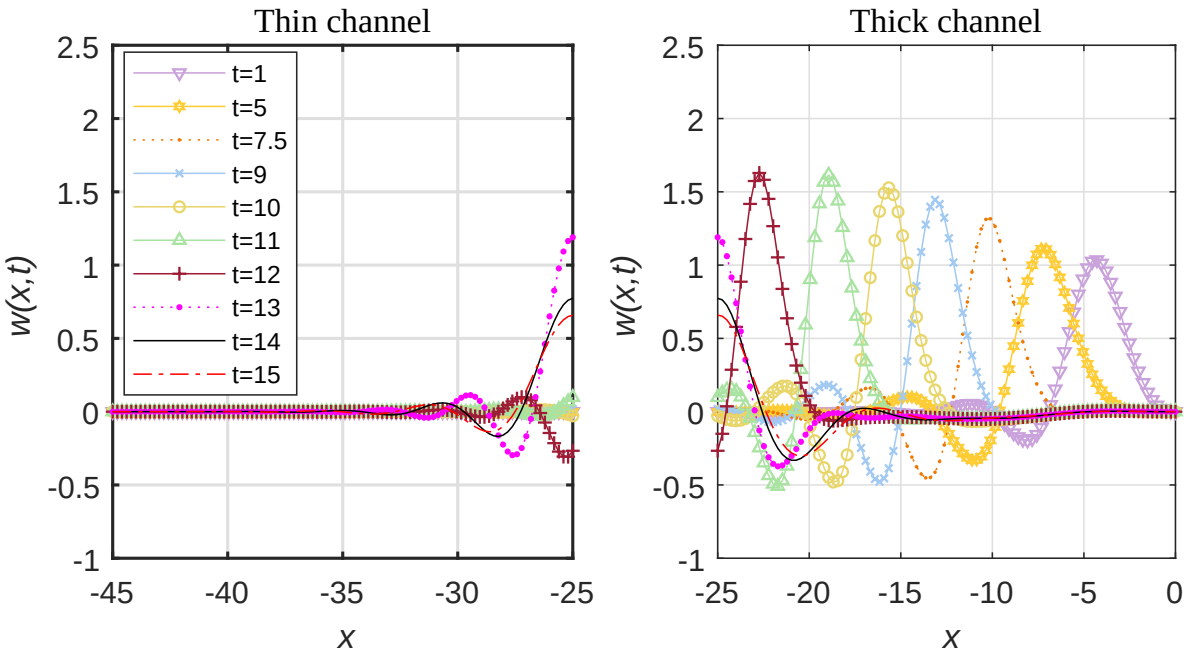

Figure 6.3: The solution from $t = 1$ to $t = 15$.

As a result, we observed the dynamics shown in Fig. 6.4, The pulse propagates from the right end of the thick channel towards its left end as time goes. The evolution of the pulse starts from a single hump in the thick channel. After a while, the solution takes a familiar pulse-like form moving towards the contact point. The homogeneous boundary conditions were used at the left end of the thin channel and right end of the thick channel. At $t = 12$, the pulse reaches the contact point ($x = -25$). Affected by the boundary conditions at the branching point, the pulse then penetrates into the thin channel.

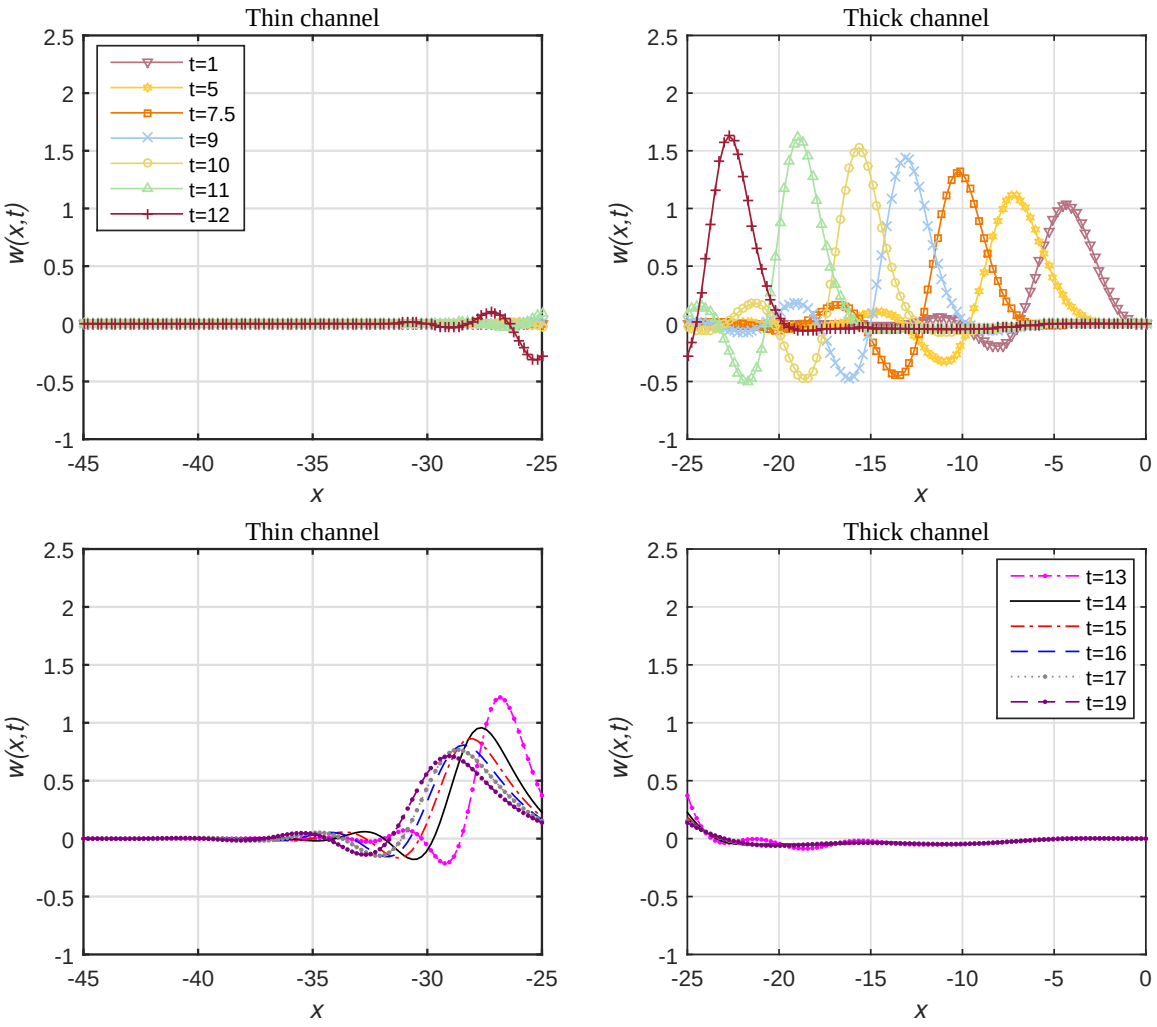

Figure 6.4: Pulse propagation through the contact point showing the early and late stages $(1 < t < 19)$.

We can clearly see that despite the pulse moves into the thin channel, it eventually decays. We suggested that the reason for this was that the excitation coefficient in the thin channel is not large enough. As a result, there is not enough energy to support the pulse in the thin channel. Therefore, we increased the excitation coefficient α_2 in the thin channel, so that the thin channel non-dimensional parameters $a = 1/8, b = 1/4, c = 1$ (Fig. 6.5). An interesting question is what is the minimum (critical) value of b in the thin channel to guarantee the pulse survival. We increased

the excitation coefficient b in the thin channel from experiment to experiment by increments (Figs. 6.5-6.9) until the pulse survived.

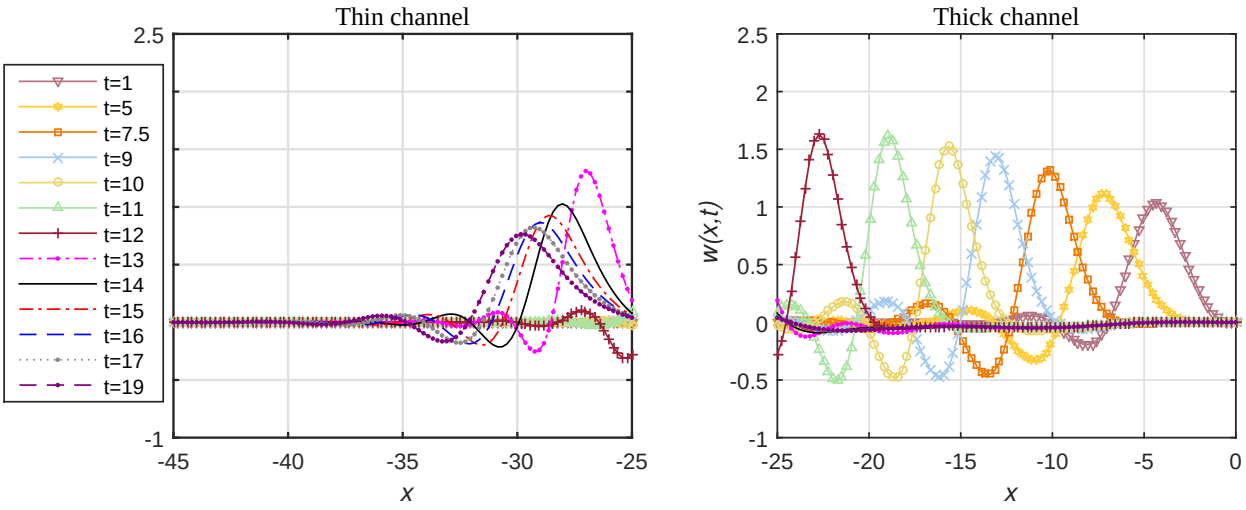

Figure 6.5: The experiment with $\alpha_2 = 2\,\alpha_1$ $(a = 1/8, b = 1/4, c = 1)$; the time ranges from $t = 1$ to 19 .

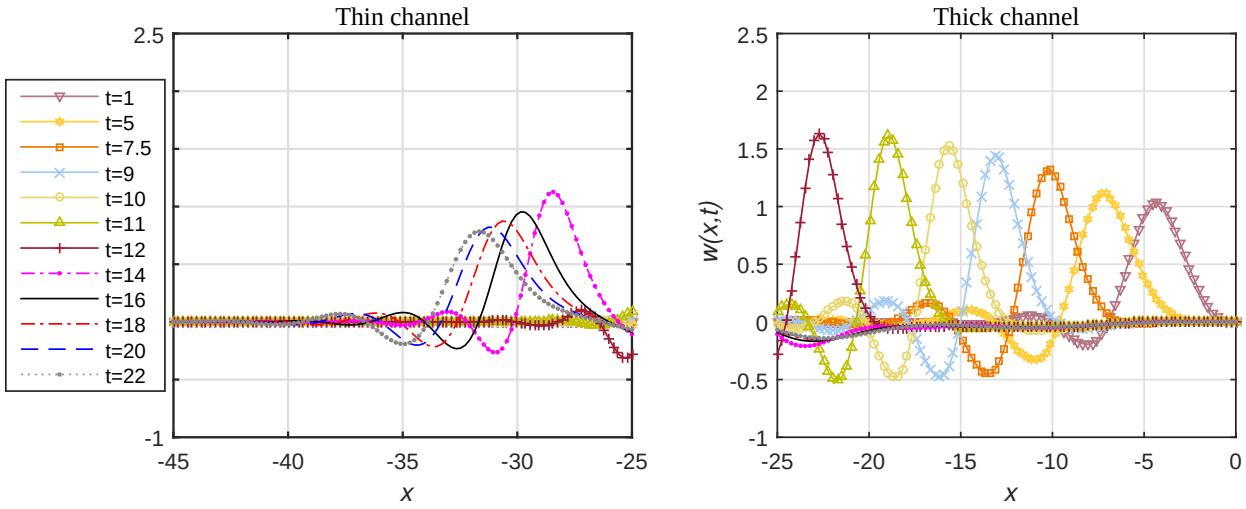

Figure 6.6: The experiment with $\alpha_2 = 3\,\alpha_1$ $(a = 1/8, b = 3/8, c = 1)$; the time ranges from $t = 1$ to 22 .

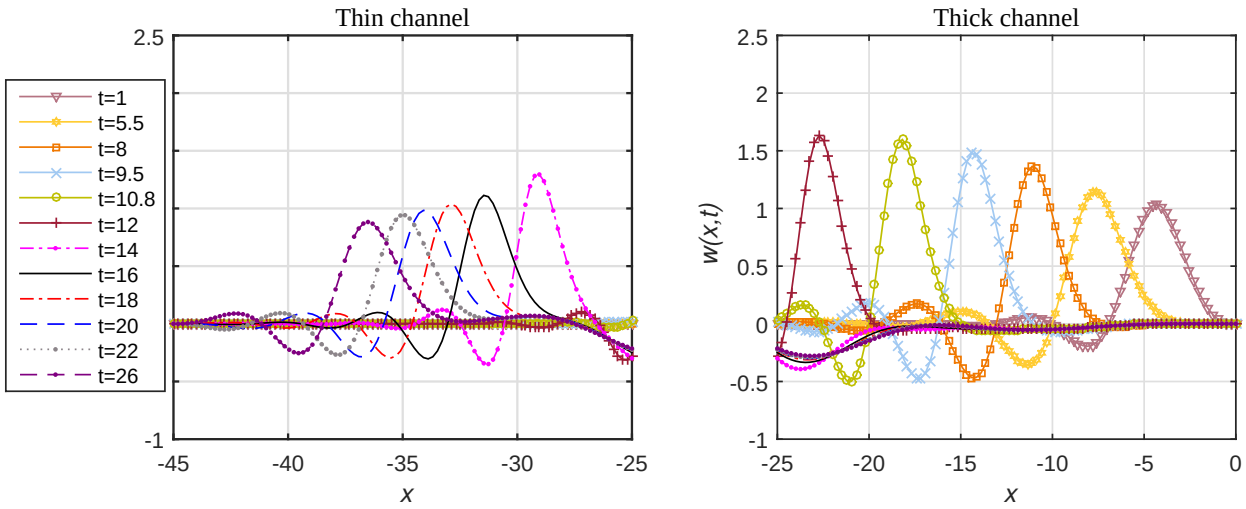

Figure 6.7: The experiment with $\alpha_2 = 4\,\alpha_1$ $(a = 1/8, b = 1/2, c = 1)$; the time ranges from $t = 1$ to 26.

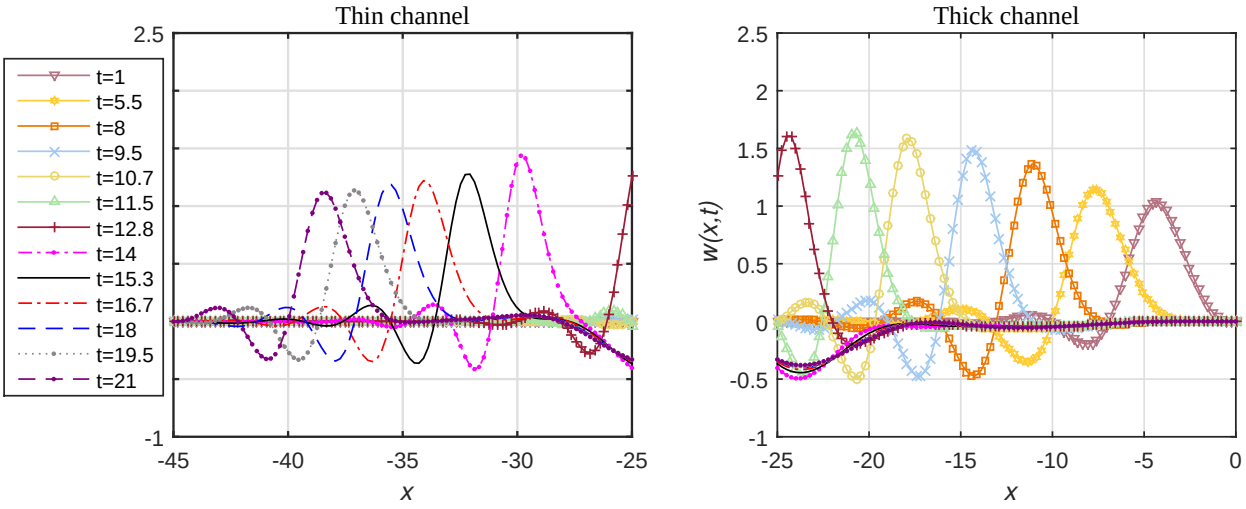

Figure 6.8: The experiment with $\alpha_2 = 4.5\,\alpha_1$ $(a = 1/8, b = 4.5/8, c = 1)$; the time ranges from $t = 1$ to 21.

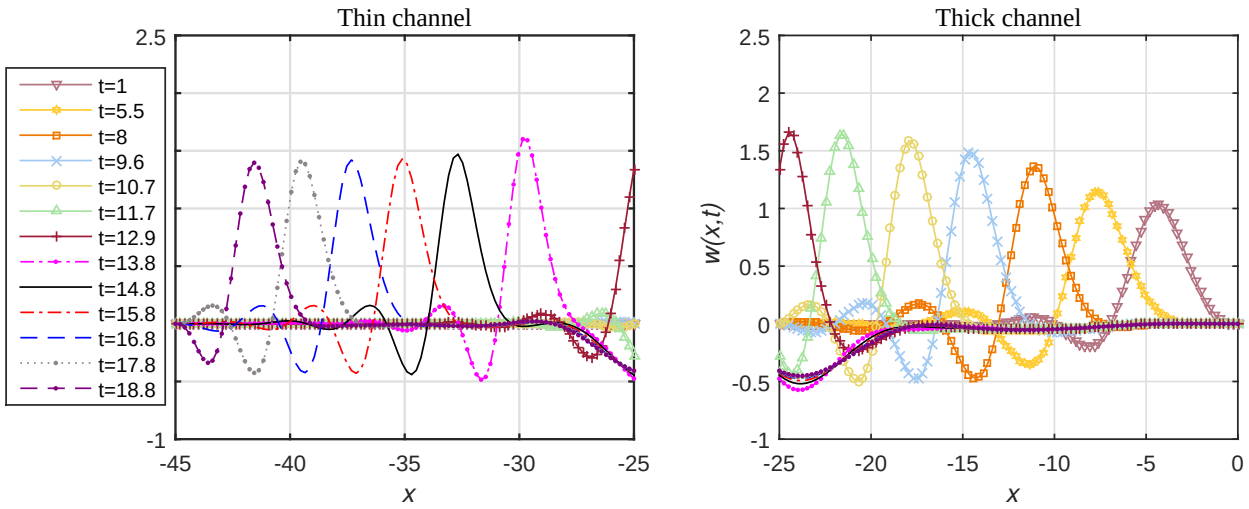

Figure 6.9: The experiment with $\alpha_2 = 4.9\,\alpha_1$ $(a = 1/8, b = 4.9/8, c = 1)$; the time ranges from $t = 1$ to 18.8.

Fig. 6.9 shows that the evolution of the pulse starts from a hump in the thick channel. After a while, the solution takes a familiar pulse-like form moving towards the contact point. The homogeneous boundary conditions were used at the left end of the thin channel and right end of the thick channel. Eventually the pulse motion ceased after it hit the boundary as shown in Fig. 6.10.

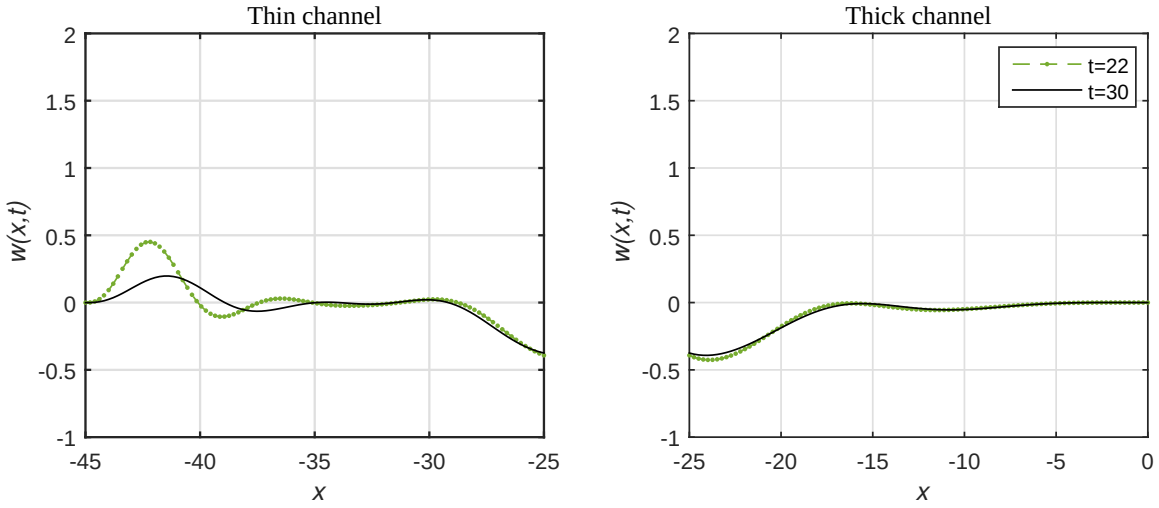

Figure 6.10: Continuation from Fig. 6.9. $t = 22, 30$.

We determined that the critical value of the excitation coefficient in the thin channel is approximately $b = 0.6$.

6.3.2 Three-channel experiment

In this numerical experiment, we consider a three-channel configuration where a thick channel branches out into two thin channels, and each of them in turn branches out into two even thinner channels. In the state of rest each of the thinner channels has half the width of the thicker channel with which it is in contact. The boundary conditions and the initial condition are the same as in the previous experiment. The displacement of the thinnest channel wall, w_3 , satisfies the equation

$$\frac{\partial w_3}{\partial t} = \frac{D}{3\eta}\left(\frac{H_0}{4}\right)^3 \frac{\partial^6 w_3}{\partial x^6} - \frac{\alpha_3}{3\eta}\left(\frac{H_0}{4}\right)^3 \frac{\partial^2}{\partial x^2}\left(w_3^4\right) + \beta_3\left(\frac{H_0}{4}\right)^3 \frac{\partial}{\partial x}\left(w_3^5\right) . \qquad (6.18)$$

Now we non-dimensionalize Eq. (6.18) to the form

$$\frac{\partial w_3}{\partial t} = a_1 \frac{\partial^6 w_3}{\partial x^6} - b_1 \frac{\partial^2}{\partial x^2}\left(w_3^4\right) + c_1 \frac{\partial}{\partial x}\left(w_3^5\right) . \qquad (6.19)$$

where the non-dimensional coefficient $a_1 = 1/46, b_1 = 4.9/46, c_1 = 1/8$. We run the numerical experiments in the similar fashion to the two-channel experiments, until the pulse survived in the thinnest channel as shown in Fig. 6.16. First we increased the value of β_3 (the thinnest channel parameter) by the factor of eight ($a_1 = 1/46, b_1 = 4.9/46, c_1 = 1$) to make the pulse propagate into the thinnest channel (Fig. 6.11). Then we increased the excitation coefficient b_1 in the thinnest channel from experiment to experiment by increments (Figs. 6.12-6.16) until the pulse survived.

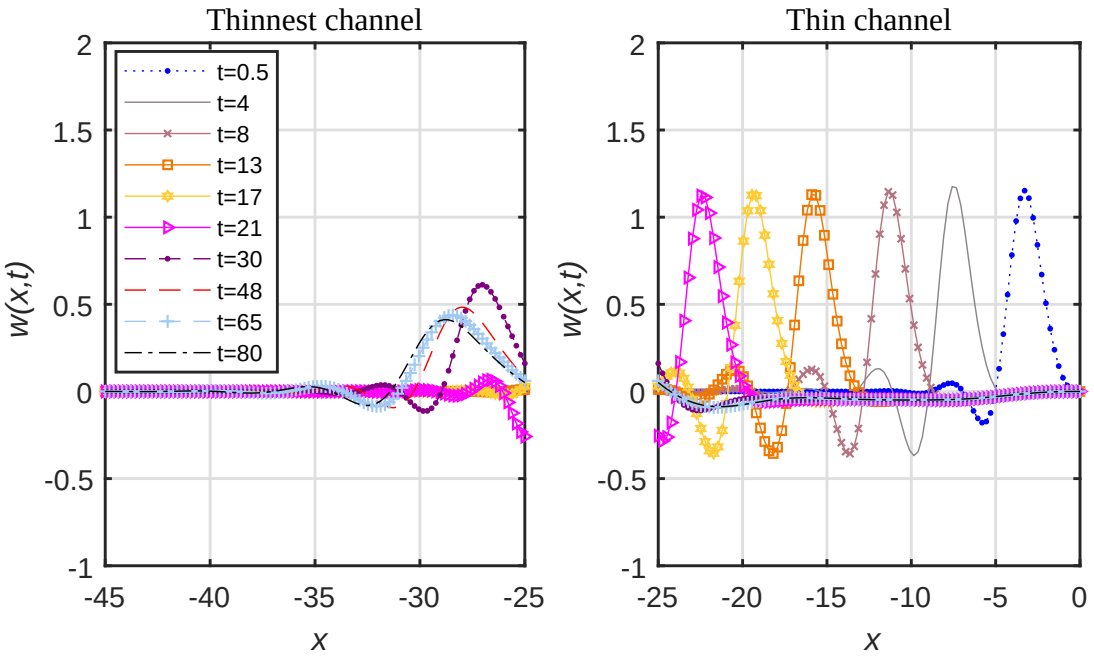

Figure 6.11: The experiment with $\alpha_3 = \alpha_2$; the time ranges from $t = 0.5$ to 80.

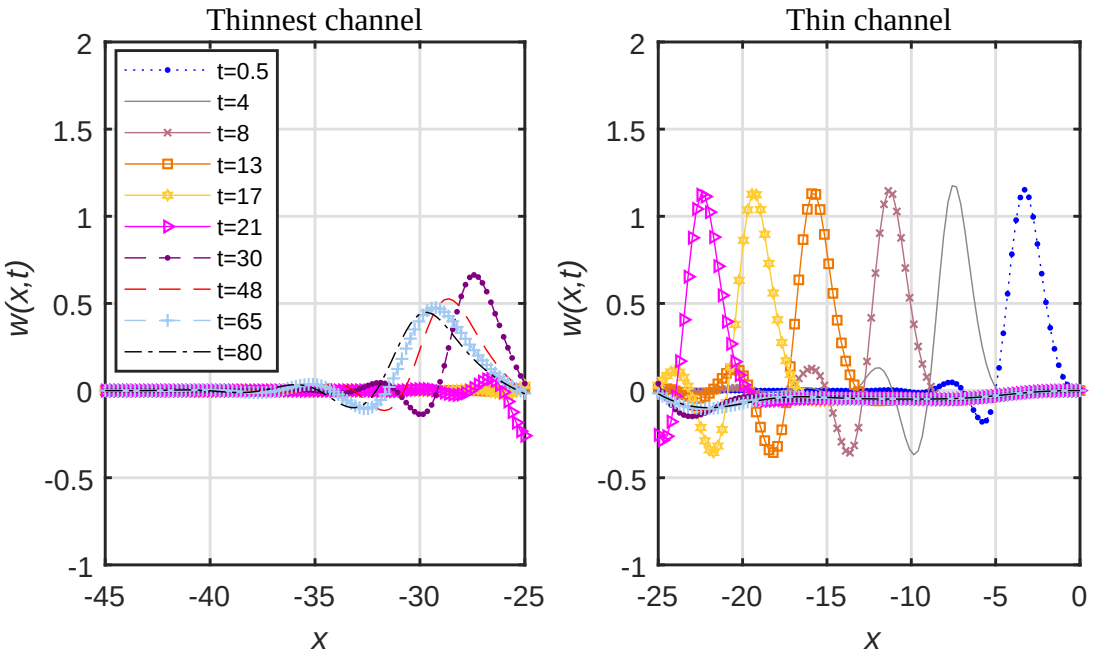

Figure 6.12: The experiment with $\alpha_3 = 2\,\alpha_2$; the time ranges from $t = 0.5$ to 80.

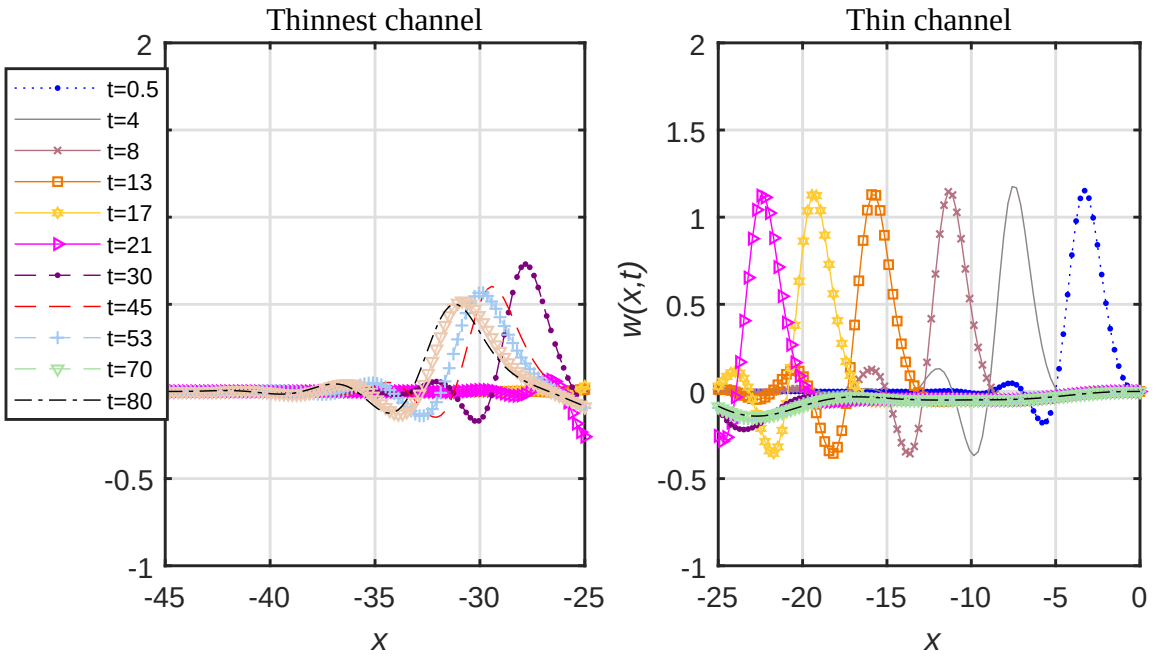

Figure 6.13: The experiment with $\alpha_3 = 3\,\alpha_2$; the time ranges from $t = 0.5$ to 80.

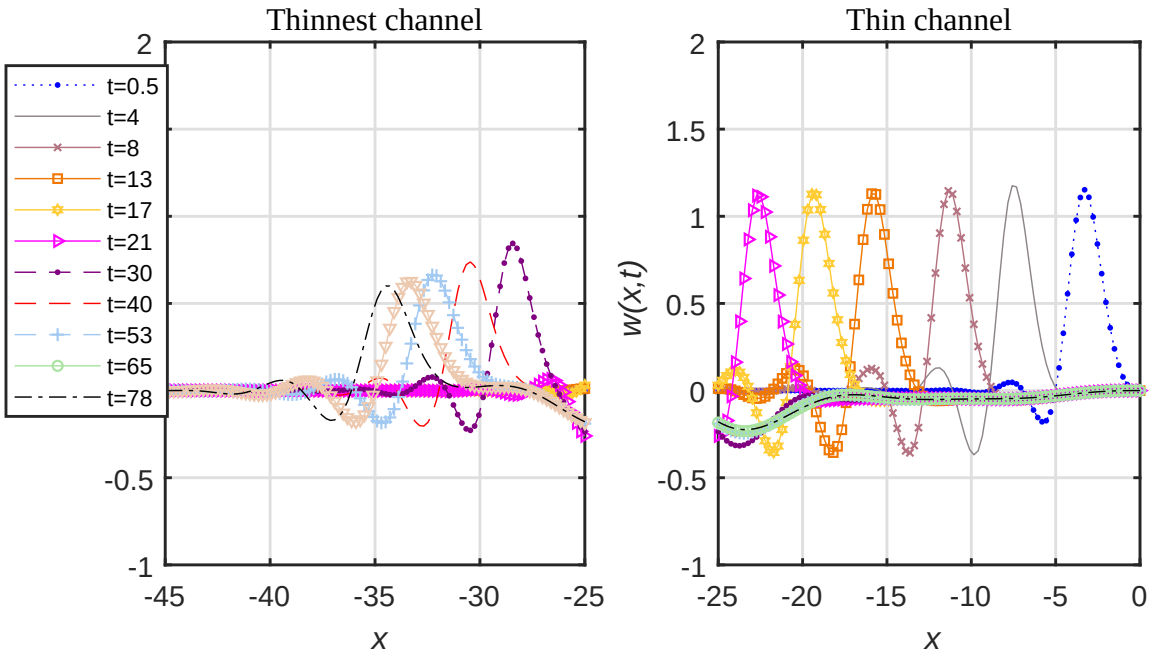

Figure 6.14: The experiment with $\alpha_3 = 4\,\alpha_2$; the time ranges from $t = 0.5$ to 78.

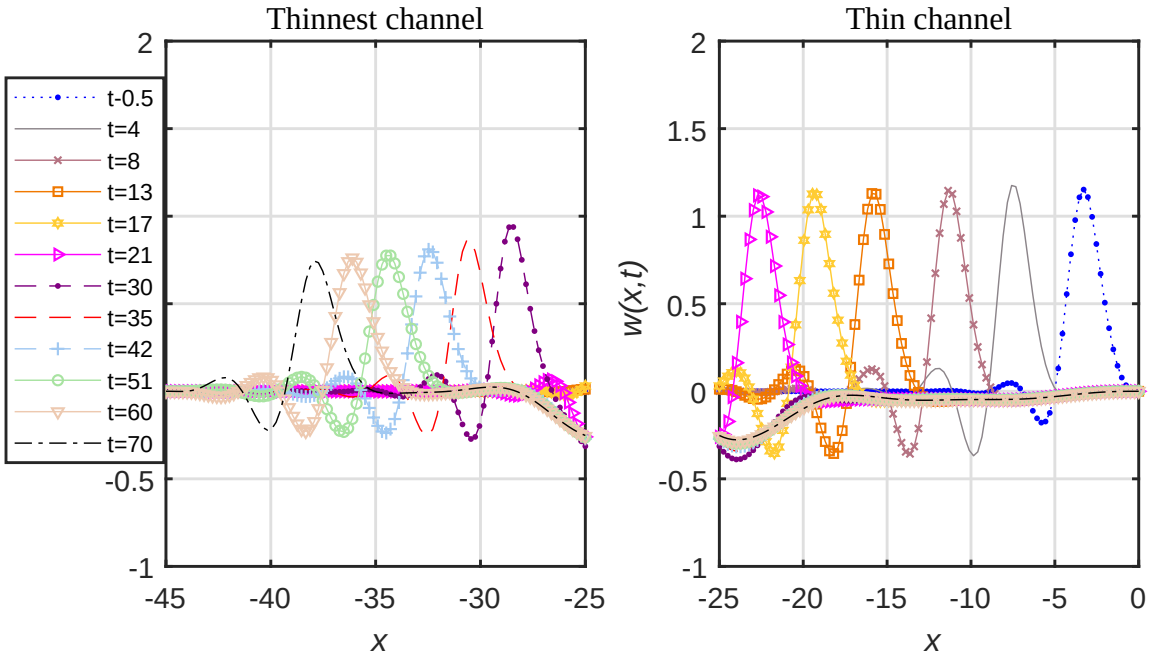

Figure 6.15: The experiment with $\alpha_3 = 4.5\,\alpha_2$; the time ranges from $t = 0.5$ to 70 .

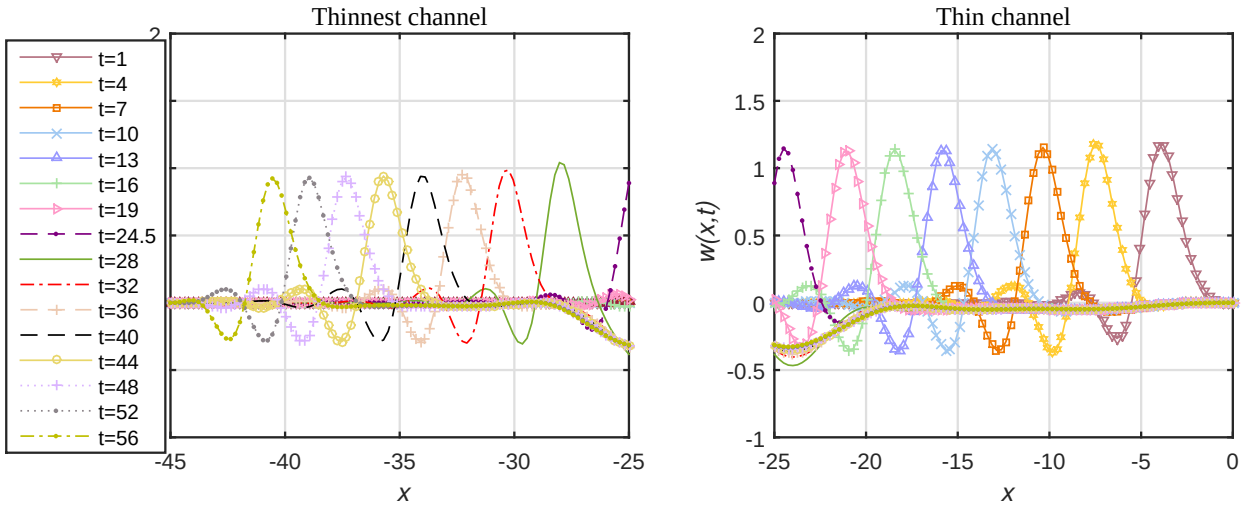

Figure 6.16: The experiment with $\alpha_3 = 4.9\,\alpha_2$; the time ranges from $t = 1$ to 56 .

Fig. 6.17 shows that the pulse decays after hitting the left boundary of the thinnest channel.

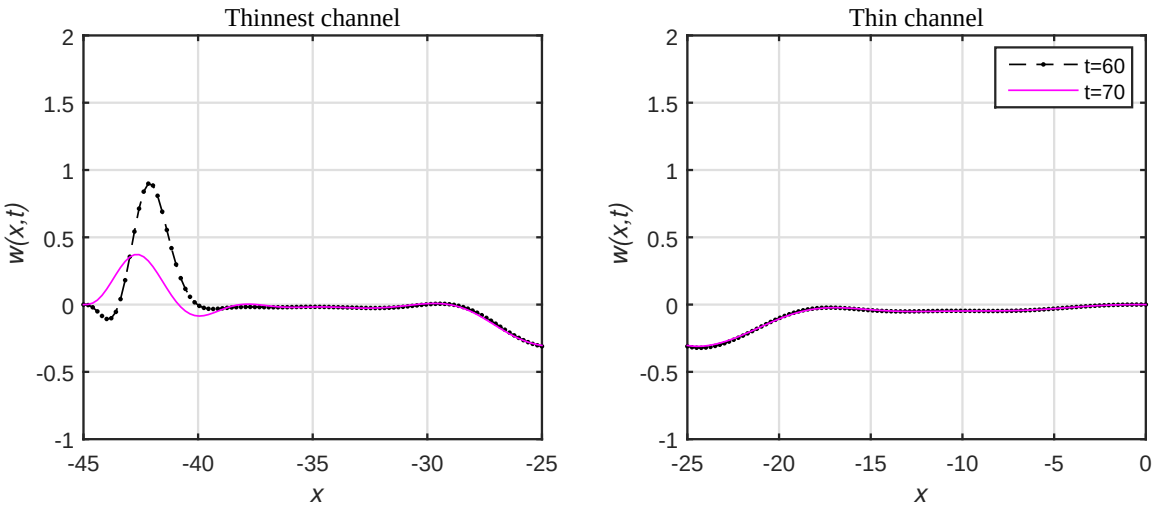

Figure 6.17: Continuation from Fig. 6.16. $t = 60, 70$.

We then determined that the critical value of the non-dimensional excitation coefficient in the thinnest channel is approximately 0.38 .

6.4 Conclusion

We applied the 1D-IRBF numerical method to solve the model of the flow between active walls adapted for a branching channel. We used homogeneous boundary conditions at the edges and continuity conditions at the branching (contact) point. We obtained and analysed solutions in the form of auto-pulses penetrating through the branching point from the thick channel into the thin channel. A series of experiments are conducted using the gradually increasing excitation coefficient α in the thin channel until the pulse survived. The numerical results indicated that the thinner the channel the larger the excitation coefficient α needs to be in order to guarantee the pulse propagation.

Chapter 7

The model with circular cross-section

7.1 Introduction

In this chapter we present the derivation of the autonomous model of fluid pulses between hypothetically active elastic walls when the channel has circular cross-section. As for the planar channel considered in the previous chapters, this model simulates an *artificial* artery. The geometry of the flow is an unbounded cylindrical channel. As before, the model is derived using the lubrication theory for the flow coupled with the theory of elasticity for the wall, and phenomenological arguments. The resulting nonlinear partial differential equation describes the displacement of the walls as a function of the distance along the flow and time. Based on the numerical experiments and using the values of mechanical parameters from literature, this chapter also presents the evaluation of the empirical parameters of the cylindrical-channel model.

7.2 Derivation of the model with circular cross-section

In this section, we present the derivation of the model with circular cross-section. We consider a long circular cylinder with cross-sectional area $A(x,t)$ of radius $R(x,t)$, as shown in Fig. 7.1.

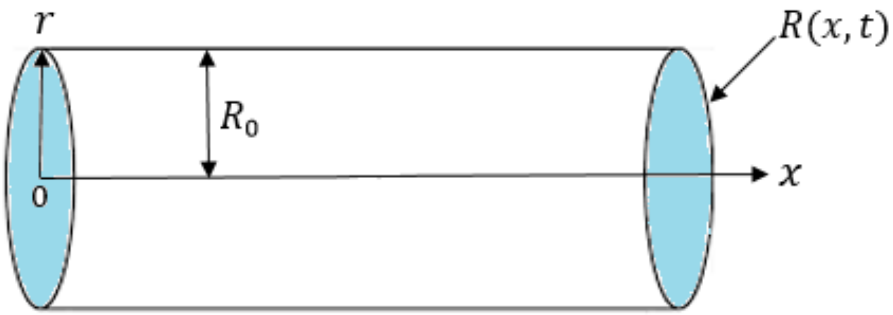

Figure 7.1: Flow through the circular channel.

It is convenient to use cylindrical coordinates (x, ϕ, r), with the centerline of the cylinder taken to be the x-axis. Assuming symmetry with respect to the x-axis of the cylinder, $r = 0$; there will be no ϕ-dependence in the model, including the radial size of the channel $R = R(x,t)$. The mean flow is assumed to be in the x-direction, driven by a pressure-gradient in that direction. As for the planar channel, we apply the lubrication theory (Huang and Suo, 2002), which equates the pressure gradient to the viscous force,

$$\frac{1}{r}\frac{\partial}{\partial r}\left(r\frac{\partial v}{\partial r}\right) = \frac{1}{\eta}\frac{\partial p}{\partial x}\,, \tag{7.1}$$

where $v(x,r,t)$ is the flow velocity in the x direction, $p(x,t)$ is the pressure, and η the viscosity. The pressure is assumed r-independent. Integrating (7.1) over the

cross-sectional area, we get

$$\frac{\pi}{\eta} r^2 \frac{\partial p}{\partial x} = 2\pi r \frac{\partial v}{\partial r} + C_1(x,t)\,. \tag{7.2}$$

Then integrating (7.2) on r, we obtain

$$v = \frac{1}{4\eta}\frac{\partial p}{\partial x} r^2 + C_1(x,t)\ln r + C_2(x,t)\,. \tag{7.3}$$

Assuming $C_1(x,t) = 0$, Eq. (7.3) becomes

$$v = \frac{1}{4\eta}\frac{\partial p}{\partial x} r^2 + C_2(x,t)\,. \tag{7.4}$$

Replacing $r = R$ and $v = v(x,R,t)$ in Eq. (7.4), we get

$$v(x,R,t) = \frac{1}{4\eta}\frac{\partial p}{\partial x} R^2 + C_2(x,t)\,. \tag{7.5}$$

Substituting (7.5) into (7.4), gives

$$v = \frac{1}{4\eta}\frac{\partial p}{\partial x}\left(r^2 - R^2\right) + v(x,R,t)\,. \tag{7.6}$$

The mass flux is

$$Q = \int_0^{2\pi}\int_0^R v\, r dr d\phi = -\frac{\pi R^4}{8\eta}\frac{\partial p}{\partial x} + v(x,R,t)\, R^2\pi\,. \tag{7.7}$$

We define the displacement, $w(x,t)$, of the wall in the r-direction from the neutral position, $R = R_0$, by

$$R(x,t) = R_0 + w\,. \tag{7.8}$$

Then the continuity equation is written as

$$\frac{\partial A}{\partial t} + \frac{\partial Q}{\partial x} = 0\,. \tag{7.9}$$

Substituting (7.7) into (7.9), one gets

$$2\pi R\frac{\partial R}{\partial t} = \frac{\partial}{\partial x}\left[\frac{\pi R^4}{8\eta}\frac{\partial p}{\partial x} - v(x,R,t)\,\pi R^2\right]\,. \tag{7.10}$$

Equation (7.10) links the displacement of the flow boundary, coinciding with the wall position, to the flow pressure. The elasticity theory (Landau and Lifshitz,

1959; Timoshenko and Woinowsky-Krieger, 1987) provides the reverse link from the pressure to the displacement

$$p = D\frac{\partial^4 w}{\partial x^4} - \frac{\partial}{\partial x}\left(N\frac{\partial w}{\partial x}\right), \tag{7.11}$$

where

$$N = \frac{Eh}{1-\nu^2}\left[\frac{\partial u}{\partial x} + \frac{1}{2}\left(\frac{\partial w}{\partial x}\right)^2\right]. \tag{7.12}$$

In Eqs. (7.11) and (7.12) $u(x,t)$ is the wall's displacement along the flow, D is the flexural rigidity of the wall, E is Young's modulus, h is the thickness of the wall, ν is Poisson's ratio, and N the force caused by the displacements. Substituting (7.12) and (7.11) into (7.10) and applying the no-slip boundary condition, $v(x,R,t) = \partial u/\partial t$, we get

$$\begin{aligned} 2\pi R\frac{\partial w}{\partial t} = {} & \frac{\pi D}{8\eta}\frac{\partial}{\partial x}\left(R^4\frac{\partial^5 w}{\partial x^5}\right) - \frac{\pi Eh}{16\eta(1-\nu^2)}\frac{\partial}{\partial x}\left[R^4\frac{\partial^2}{\partial x^2}\left(\frac{\partial w}{\partial x}\right)^3\right] \\ & - \frac{\pi Eh}{8\eta(1-\nu^2)}\frac{\partial}{\partial x}\left[R^4\frac{\partial^2}{\partial x^2}\left(\frac{\partial u}{\partial x}\frac{\partial w}{\partial x}\right)\right] - \pi\frac{\partial}{\partial x}\left(\frac{\partial u}{\partial t}R^2\right). \end{aligned} \tag{7.13}$$

The shear stress in the fluid is given by $T = \eta\,\partial v/\partial z$, therefore on the boundary, $r = R$, using (7.6),

$$T = \frac{\partial p}{\partial x}R\,. \tag{7.14}$$

This shear stress must be equal to the shear stress produced by the wall,

$$T = \frac{\partial N}{\partial x}\,. \tag{7.15}$$

Equating (7.14) and (7.15) with the use of (7.12), we have

$$\frac{E}{1-\nu^2}\left[\frac{\partial^2 u}{\partial x^2} + \frac{1}{2}\frac{\partial}{\partial x}\left(\frac{\partial w}{\partial x}\right)^2\right] = \frac{\partial p}{\partial x}R\,. \tag{7.16}$$

The three equations (7.13), (7.16) and (7.11) form a closed system with respect to the three functions of interest $w(x,t)$, $u(x,t)$ and $p(x,t)$. Now suppose that, when deflecting from the neutral position, the elastic walls exert extra pressure relative to (7.11),

$$p = D\frac{\partial^4 w}{\partial x^4} - \frac{\partial}{\partial x}\left(N\frac{\partial w}{\partial x}\right) + p_0 + p_1\,, \tag{7.17}$$

in which p_0 is a constant (reference pressure) and p_1 depends on w. We postulate that p_1 is proportional to the 4^{th} power of the vertical displacement plus the term representing the Hooke's law,

$$p_1 = -\alpha w^4 + \gamma w\,, \quad \alpha > 0\,,\, \gamma > 0\,, \tag{7.18}$$

where the last term expresses the passive effect of the increase of the radius if the pressure is increased. For the planar case analysed in Chapter 2, the two planes are not directly connected to each other, therefore this term was absent. Further, we suppose that the walls actively move along the flow, thereby producing an extra shear stress relative to (7.16). We postulate that the wall's motion along the flow, represented by the displacement u and velocity $\partial u/\partial t$, is coupled with w. Specifically, the R–weighted velocity along the flow, $R\partial u/\partial t$, combined with the other u–containing term in (7.13), depends on w as

$$-\frac{\pi E h}{8\eta(1-\nu^2)} R^4 \frac{\partial^2}{\partial x^2}\left(\frac{\partial u}{\partial x}\frac{\partial w}{\partial x}\right) - \frac{\partial u}{\partial t} R^2 = R^4 \beta w^5 - K\,, \quad \beta > 0\,, \tag{7.19}$$

where K is a constant. As for the planar-channel case, K is an eigenvalue of a settled pulse regime; it will be appropriately selected to ensure that the horizontal displacement of the wall after each pulse is zero. This relation implies that an extra (active) shear stress is applied by the wall; we denote it T_1. The total stress satisfies the continuity condition on the boundary

$$T_1 + \frac{E}{1-\nu^2}\left[\frac{\partial^2 u}{\partial x^2} + \frac{1}{2}\frac{\partial}{\partial x}\left(\frac{\partial w}{\partial x}\right)^2\right] = \frac{\partial p}{\partial x} R\,, \tag{7.20}$$

where the pressure p is represented by (7.17). Relations (7.18) and (7.19) state that the larger the deformation w the larger active response from the wall. Under the assumptions (7.17), (7.18) and (7.19), Eq. (7.13) governing the dynamics of the vertical displacement becomes u-independent:

$$\begin{aligned}\frac{\partial w}{\partial t} = {} & \frac{D}{16\eta R}\frac{\partial}{\partial x}\left[R^4 \frac{\partial^5 w}{\partial x^5}\right] - \frac{Eh}{32\eta(1-\nu^2)R}\frac{\partial}{\partial x}\left[R^4 \frac{\partial^2}{\partial x^2}\left(\frac{\partial w}{\partial x}\right)^3\right] \\ & - \frac{\alpha}{16\eta R}\frac{\partial}{\partial x}\left[R^4 \frac{\partial}{\partial x}\left(w^4\right)\right] + \frac{\gamma}{16\eta R}\frac{\partial}{\partial x}\left[R^4 \frac{\partial w}{\partial x}\right] + \frac{\beta}{2R}\frac{\partial}{\partial x}\left(R^4 w^5\right)\,. \end{aligned} \tag{7.21}$$

It is important to require that the overall displacement of the wall over one period, T, is zero,

$$\int_T \frac{\partial u}{\partial t}\, dt = 0\,, \quad \int_T \frac{\partial w}{\partial t}\, dt = 0\,. \tag{7.22}$$

The second condition in (7.22) is guaranteed provided the boundary conditions are periodic. Indeed, each term in the equation's right-hand side is a derivative and the expression under differentiation is periodic. The first condition of (7.22) can be transformed using (7.19) to the form

$$\int_T \left[-\frac{\pi E h}{8\eta(1-\nu^2)} R^2 \frac{\partial^2}{\partial x^2}\left(\frac{\partial u}{\partial x}\frac{\partial w}{\partial x}\right) - \beta R^2 w^5 + \frac{K}{R^2}\right] dt = 0\,, \tag{7.23}$$

which can be met by selecting K. The procedure of finding solution is as follows. The function $w(x,t)$ is obtained from (7.21) under, say, periodic boundary conditions. Then $u(x,t)$ and K are found from (7.19), (7.23) for the settled pulse regime. Lastly, the pressure is obtained from (7.17), (7.18), and the extra shear stress $T_1(x,t)$ and total stress from (7.20).

As in the planar-channel model, the E-containing terms will not participate in the dynamical balance supporting pulses. As before, we assume that E is sufficiently small and the E-containing terms can be neglected. In this case the main equation (7.21) takes the simpler form

$$\begin{aligned}\frac{\partial w}{\partial t} = {} & \frac{D}{16\eta R}\frac{\partial}{\partial x}\left[R^4 \frac{\partial^5 w}{\partial x^5}\right] - \frac{\alpha}{16\eta R}\frac{\partial}{\partial x}\left[R^4 \frac{\partial}{\partial x}\left(w^4\right)\right] + \frac{\gamma}{16\eta R}\frac{\partial}{\partial x}\left[R^4 \frac{\partial w}{\partial x}\right] \\ & + \frac{\beta}{2R}\frac{\partial}{\partial x}\left(R^4 w^5\right)\,,\end{aligned} \tag{7.24}$$

and the condition (7.23) becomes

$$\int_T \left[-\beta R^2 w^5 + \frac{K}{R^2}\right] dt = 0\,. \tag{7.25}$$

In order to simplify the model further, assume

$$w << R_0\,.$$

Then we can replace R by $R = R_0 + w \approx R_0$ in Eq. (7.24) to get

$$\frac{\partial w}{\partial t} = \frac{D R_0^3}{16\eta}\frac{\partial^6 w}{\partial x^6} - \frac{R_0^3 \alpha}{16\eta}\frac{\partial^2}{\partial x^2}\left(w^4\right) + \frac{R_0^3 \gamma}{16\eta}\frac{\partial^2 w}{\partial x^2} + \frac{R_0^3 \beta}{2}\frac{\partial}{\partial x}\left(w^5\right)\,. \tag{7.26}$$

Relative to the planar case, Eq. (7.26) also has the 2nd-order dissipative term $\sim w''$ (the dash stands for $\partial/\partial x$). It may slightly affect the pulse characteristics, such as hight and speed, but will not change the pulse-generating dynamical balance. Thus we ignore the 2nd-order dissipative term, w'' and transform the main equation (7.26) to the simpler form

$$\frac{\partial w}{\partial t} = \frac{DR_0^3}{16\eta}\frac{\partial^6 w}{\partial x^6} - \frac{R_0^3\alpha}{16\eta}\frac{\partial^2}{\partial x^2}\left(w^4\right) + \frac{R_0^3\beta}{2}\frac{\partial}{\partial x}\left(w^5\right) . \tag{7.27}$$

An individual pulse is formed by the dynamical balance between the three terms in the right-hand side of (7.27),

$$R_0^3\frac{D}{16\eta}w^{VI} \sim -R_0^3\frac{\alpha}{16\eta}(w^4)'' \sim R_0^3\frac{\beta}{2}(w^5)' . \tag{7.28}$$

This relationship determines the characteristic scales for the height, Δw, and width, Δx, of an individual pulse. They will be independent of R_0 since R_0^3 can be cancelled out in (7.28).

7.3 Evaluation of the coefficients of the cylindrical-channel model

In this section, we evaluate the coefficients α and β of the cylindrical model (7.27). As in Section 5.3, we re-scale the dimensional equation (7.27) in two steps. In step one, we non-dimensionalize the equation using R_0 as the spatial scale and η/E as the time scale. Then, in step two, we re-scale w, t and x using the yet-to-be-determined non-dimensional scaling factors W_*, T_* and X_*, respectively. Thus,

$$w = R_0 w_{1c} , \quad w_{1c} = W_* w_{2c} ,$$

$$x = R_0 x_{1c} , \quad x_{1c} = X_* x_{2c} ,$$

$$t = \eta t_{1c}/E , \quad t_{1c} = T_* t_{2c} .$$

The resulting non-dimensional equation is

$$\frac{\partial w_{2c}}{\partial t_{2c}} = A_* \frac{\partial^6 w_{2c}}{\partial x_{2c}^6} - B_* \frac{\partial^2}{\partial x_{2c}^2}\left(w_{2c}^4\right) + C_* \frac{\partial}{\partial x_{2c}}\left(w_{2c}^5\right) , \tag{7.29}$$

where

$$A_* = \frac{DT_*}{16ER_0^3X_*^6} , \quad B_* = \frac{\alpha R_0^4 T_* W_*^3}{16EX_*^2} , \quad C_* = \frac{\beta\eta R_0^6 T W_*^4}{2EX_*} . \tag{7.30}$$

Eq. (7.29) is the non-dimensional equation of (7.27). We repeat the non-dimensional equation of Eq. (4.2) for convenience,

$$\frac{\partial w_{2p}}{\partial t_{2p}} = A \frac{\partial^6 w_{2p}}{\partial x_{2p}^6} - B \frac{\partial^2}{\partial x_{2p}^2}\left(w_{2p}^4\right) + C \frac{\partial}{\partial x_{2p}}\left(w_{2p}^5\right) , \tag{7.31}$$

where

$$A = \frac{DT}{3EH_0^3X^6} , \quad B = \frac{\alpha H_0^4 T W^3}{3EX^2} , \quad C = \frac{\beta\eta H_0^6 T W^4}{EX} . \tag{7.32}$$

The difference between the planar model (7.31) and cylindrical model (7.29) can be seen from (7.29) re-written as

$$\frac{\partial w_{2c}}{\partial t_{2c}} = \frac{3A}{16} \frac{\partial^6 w_{2c}}{\partial x_{2c}^6} - \frac{3B}{16} \frac{\partial^2}{\partial x_{2c}^2}\left(w_{2c}^4\right) + \frac{C}{2} \frac{\partial}{\partial x_{2c}}\left(w_{2c}^5\right) . \tag{7.33}$$

Thus, the coefficients A_*, B_* and C_* for the cylindrical model are connected to the coefficients of the planar model as

$$A_* = \frac{3}{16}A , \quad B_* = \frac{3}{16}B , \quad C_* = \frac{1}{2}C . \tag{7.34}$$

The results of the numerical experiments for the planar model were obtained with $A = 1 , B = 1 , C = 1$, so that the cylindrical model is

$$\frac{\partial w_{2c}}{\partial t_{2c}} = \frac{3}{16} \frac{\partial^6 w_{2c}}{\partial x_{2c}^6} - \frac{3}{16} \frac{\partial^2}{\partial x_{2c}^2}\left(w_{2c}^4\right) + \frac{1}{2} \frac{\partial}{\partial x_{2c}}\left(w_{2c}^5\right) . \tag{7.35}$$

Rather than conducting a new series of experiments for the model (7.35) we will re-scale the planar model variables w_{2p}, x_{2p} and t_{2p} so that governing equation takes the form (7.35). Then the solution $w_{2c}(x_{2c}, t_{2c})$ will obtain simply by re-scaling $w_{2p}(x_{2p}, t_{2p})$. As we mentioned before, in the planar-channel model, the non-dimensional amplitude of the pulse $\Delta w_{2p} = 2.1$ and the non-dimensional pulse speed $\Delta x_{2p}/\Delta t_{2p} =$

2.53 are measured from the numerical experiments of the single-pulse solution (Fig. 4.12 in Chapter 4). To measure the non-dimensional amplitude of the pulse Δw_{2c} and the non-dimensional pulse speed $\Delta x_{2c}/\Delta t_{2c}$ for the cylindrical-channel model, we assume

$$w_{2p} = W_* w_{2c}\,, \quad x_{2p} = X_* x_{2c} \quad \text{and} \quad t_{2p} = T_* t_{2c}\,.$$

Substituting these into (7.31) gives

$$\frac{\partial w_{2c}}{\partial t_{2c}} = \frac{T_*}{X_*^6}\frac{\partial^6 w_{2c}}{\partial x_{2c}^6} - \frac{T_* W_*^3}{X_*^2}\frac{\partial^2}{\partial x_{2c}^2}\left(w_{2c}^4\right) + \frac{T_* W_*^4}{X_*}\frac{\partial}{\partial x_{2c}}\left(w_{2c}^5\right)\,. \tag{7.36}$$

Equating the coefficients of (7.36) to (7.35) respectively we get

$$W_* = 53.3\,, \quad X_* = 0.05 \quad \text{and} \quad T_* = 2.9 \times 10^{-9}\,.$$

So, the non-dimensional amplitude of the pulse is

$$\Delta w_{2c} = \frac{\Delta w_{2p}}{W_*} = 0.04 \tag{7.37}$$

and the non-dimensional pulse speed

$$\frac{\Delta x_{2c}}{\Delta t_{2c}} = \frac{T_*}{X_*}\frac{\Delta x_{2p}}{\Delta t_{2p}} = 1.5 \times 10^{-7}\,. \tag{7.38}$$

Returning to the dimensional quantities, we have, for the dimensional pulse amplitude,

$$\Delta w = R_0 W_* \Delta w_{2c} \tag{7.39}$$

and, for the dimensional pulse speed,

$$v = \frac{\Delta x}{\Delta t} = \frac{R_0 X_* E}{\eta T_*}\frac{\Delta x_{2c}}{\Delta t_{2c}}\,. \tag{7.40}$$

We require that the coefficients α and β lead to realistic orders of magnitude for Δw and v in (7.39)–(7.40). From the literature, by the order of magnitude, $v = 4\,\mathrm{m/s}$ (London and Pannier, 2010; Lehmann, 1999), and $\Delta w = 0.001\,\mathrm{m}$. The three equations (7.34) with $A = B = C = 1$ (where A_*, B_* and C_* are given by (7.30))

and equations (7.39) and (7.40) form a system of five equations with respect to the five parameters W_*, X_*, T_*, α and β that are to be determined. We find

$$W_* = \left(\frac{\Delta w}{\Delta w_{2c}}\right) R_0^{-1}\,,$$

$$X_* = D^{1/5}(3\eta)^{-1/5}\, v^{-1/5} R_0^{-2/5} \left(\frac{\Delta x_{2c}}{\Delta t_{2c}}\right)^{1/5},$$

$$T_* = E D^{1/5} R_0^{3/5}\,(3)^{-1/5}\,(v\eta)^{-6/5} \left(\frac{\Delta x_{2c}}{\Delta t_{2c}}\right)^{6/5},$$

$$\alpha = R_0^{-12/5} \left(\frac{\Delta x_{2c}}{\Delta t_{2c}}\right)^{-4/5} D^{1/5}(3\eta)^{4/5} \left(\frac{\Delta w_{2c}}{\Delta w}\right)^{3} v^{4/5}\,,$$

$$\beta = \left(\frac{\Delta x_{2c}}{\Delta t_{2c}}\right)^{-1} \left(\frac{\Delta w_{2c}}{\Delta w}\right)^{4} v\, R_0^{-3}\,.$$

As we mentioned before, the other parameters have the following approximate values: $R_0 = 0.005\,\mathrm{m}$, the Young's modulus $E = 3 \times 10^5\,\mathrm{Pa}$ (Zhang et al., 2005), the Poisson ratio $\nu = 0.5$ (Olufsen et al., 2000; Matthys et al., 2007; Surovtsova, 2005; Avolio, 1980; Kalita, 2004; Quarteroni et al., 2000), the blood viscosity $\eta = 0.004\,\mathrm{Pa}\cdot\mathrm{s}$ (Avolio, 1980) and the wall thickness $h = 0.001\,\mathrm{m}$ (Quarteroni et al., 2000) . Therefore, the flexural rigidity $D = Eh^3/[12(1-\nu^2)] = 3.3 \times 10^{-5}\,\mathrm{Pa}\cdot\mathrm{m}^3$. Based on these figures, we have, by the order of magnitude,

$$\alpha = 1.3 \times 10^{13}\,\mathrm{Pa}\cdot\mathrm{m}^{-4}$$

and

$$\beta = 6.8 \times 10^{19}\,\mathrm{m}^{-6}\cdot\mathrm{s}^{-1}\,.$$

In the final analysis the difference in the values for α and β for the cylindrical and plane channels results from the fundamental difference between the cylinder and plane as geometric objects. Mathematically this difference appears for the first time in Eq. (7.2) which is obtain by integrating the equation of motion (7.1) over the cross-sectional area of the cylinder.

7.4 Conclusion

We derived and analysed the model for the flow between active elastic walls when the cross-sectional area of the flow is circular. Based on the numerical results, we then evaluated the empirical parameters α and β responsible for the active component of the wall dynamics.

Chapter 8

Auto-pulses in a single-channel flow with non-constant cross-section

8.1 Introduction

In this chapter we present the numerical solutions of the model of self-propagating fluid pulses through the single channel with *non-constant* cross-section. The model has the non-dimensional form similar to (4.3) but with $H = H(x)$ remaining under differentiation operators,

$$\frac{\partial w}{\partial t} = A_0 \frac{\partial}{\partial x}\left[H^3 \frac{\partial^5 w}{\partial x^5}\right] - B_0 \frac{\partial}{\partial x}\left[H^3 \frac{\partial}{\partial x}\left(w^4\right)\right] + C_0 \frac{\partial}{\partial x}\left(H^3 w^5\right) . \tag{8.1}$$

In (8.1) the width H is now non-dimensional.

Again for solving Eq. (8.1) we use the One-dimensional Integrated Radial Basis Function Network (1D-IRBFN) method in conjunction with one-step Picard iteration (PI1) scheme (Ahmed et al., 2016). In the previous chapters, we solved Eq. (8.1) numerically assuming the channel width, H_0, constant. In this chapter we solve

Eq. (8.1) numerically for the background width, H_0, varying along the flow, $H(x,t) = H_0(x) + w(x,t)$. We will consider two cases: (1) when $H_0(x)$ has constant gradient (Fig. 8.1), and (2) when $H_0(x)$ represents local narrowing of the channel (Fig. 8.2).

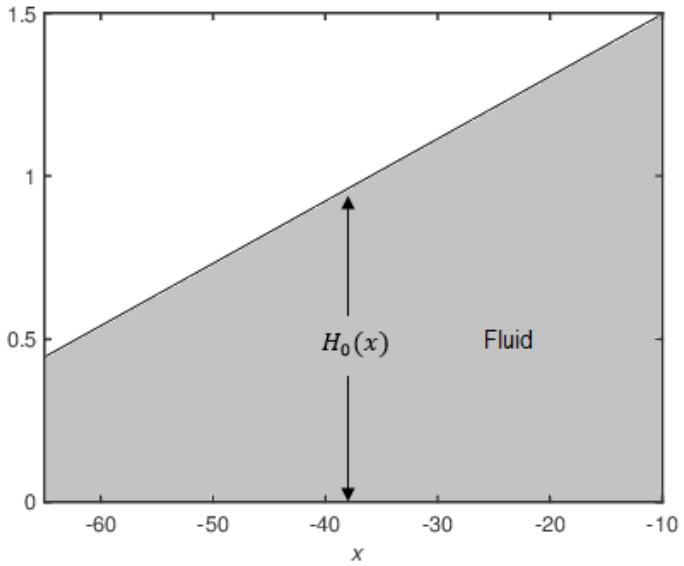

Figure 8.1: The gradually narrowing channel with constant gradient of $H_0(x)$.

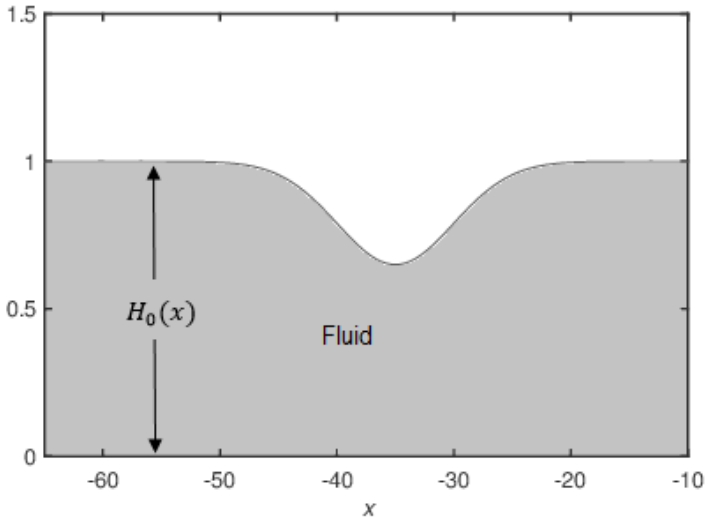

Figure 8.2: The local narrowing of the channel: $H_0(x) = H_1 - H_2 \exp[-((x-x_0)/L)^2]$ when $H_1 = 1$, $H_2 = 0.35$, $L = 7$ and $x_0 = -35$.

The chapter is organised as follows. Section 8.2 presents the numerical solution of the model. Then, Section 8.3 summarizes the chapter.

8.2 Numerical experiments

8.2.1 Single-pulse regimes for non-constant width under homogeneous boundary conditions

In these numerical experiments we set homogeneous boundary conditions on the left and on the right edges,

$$w^{(k)}(x_0) = 0\,, \quad w^{(k)}(x_0 + L) = 0\,, \quad k = 0, 1, 2\,.$$

The equation coefficients are chosen to be $A_0 = 1$, $B_0 = 1$ and $C_0 = 1$. As in Chapter 4, for solving Eq. (8.1), we use the temporal discretization by a time-stepping scheme, followed by the spatial discretization based on the 1D-IRBFN method. The standard time-stepping θ-scheme (Quarteroni and Valli, 2008), $0 \leq \theta \leq 1$ is used in this work.

Experiment 1. The channel with constant gradient.

In the first experiment, we present the numerical solutions of Eq. (8.1) for the gradually narrowing channel with constant gradient of H_0. Eq. (8.1) transforms into the form

$$\begin{aligned}\frac{\partial w}{\partial t} &= A_0 H^3 \frac{\partial^6 w}{\partial x^6} + 3A_0 H^2 \frac{\partial H}{\partial x}\frac{\partial^5 w}{\partial x^5} - B_0 H^3 \left(12w^2 \left(\frac{\partial w}{\partial x}\right)^2 + 4w^3 \frac{\partial^2 w}{\partial x^2}\right) \\ &\quad - 3B_0 H^2 \frac{\partial H}{\partial x}\left(4w^3 \frac{\partial w}{\partial x}\right) + 5C_0 H^3 w^4 \frac{\partial w}{\partial x} + 3C_0 H^2 \frac{\partial H}{\partial x} w^5\,.\end{aligned} \tag{8.2}$$

The narrowing channel is modelled by the linear function $H_0(x) = Mx + N$ with M and N being constants. In (8.2) we simplify the combination

$$3H^2\partial_x H = 3\left(Mx + N + w\right)^2 M \approx 3N^2 M$$

upon neglecting Mx and w compared to N. We denote

$$3\,N^2 M = \sigma\,.$$

Further, in (8.2) we replace H^3 by $H^3 = (H_0 + w)^3 \approx H_0^3$. In the experiments we put $H_0 = 1$. The number of nodes is 120, and the time step 0.001 .

The initial condition is chosen to be

$$w(x,0) = 2.8\,\exp[-0.95(x+12.5)^2] \tag{8.3}$$

see Fig. 8.3 .

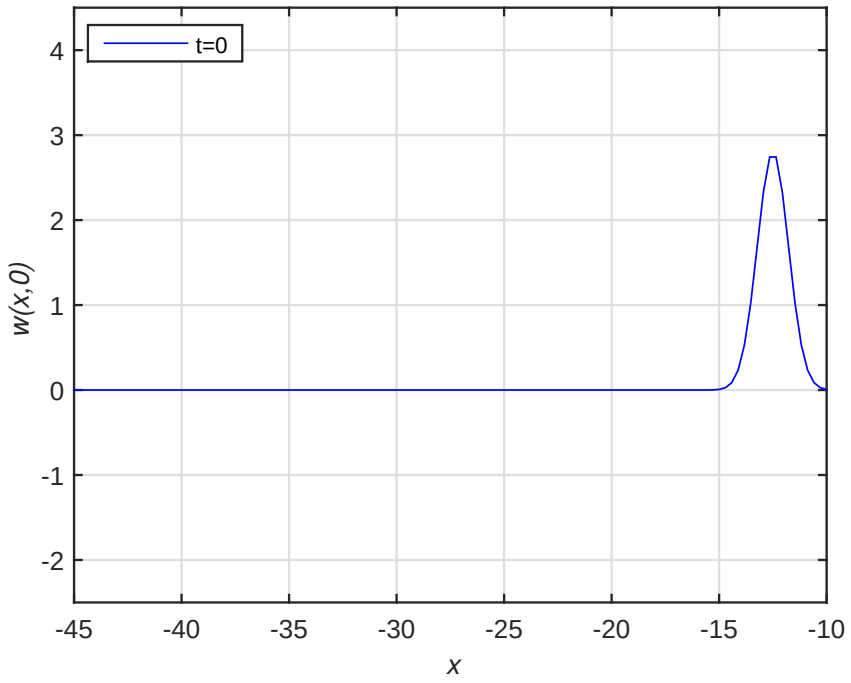

Figure 8.3: The initial condition (8.3) .

We conducted a series of experiments with different values of σ. In the first run we used $\sigma = 0.1$, and observed that the pulse propagates with constant speed and amplitude as illustrated in Figs. 8.4-8.5; this is due to the fact that Eq. (8.2) does not contain explicit functions of x; thus the equation controlling the pulse has the same form no matter where the pulse is at any given moment.

It is important to note that the displacement of the wall, w, in the model (8.2) is counted from the sloping level which is controlled by σ. We increased σ by increments from experiment to experiment. We managed to obtain pulse solutions up to $\sigma = 0.6$. For larger values of σ the code did not produce numerically stable solutions, therefore we only report the results for $0 \leq \sigma \leq 0.6$. They are presented in Figs. 8.4-8.5.

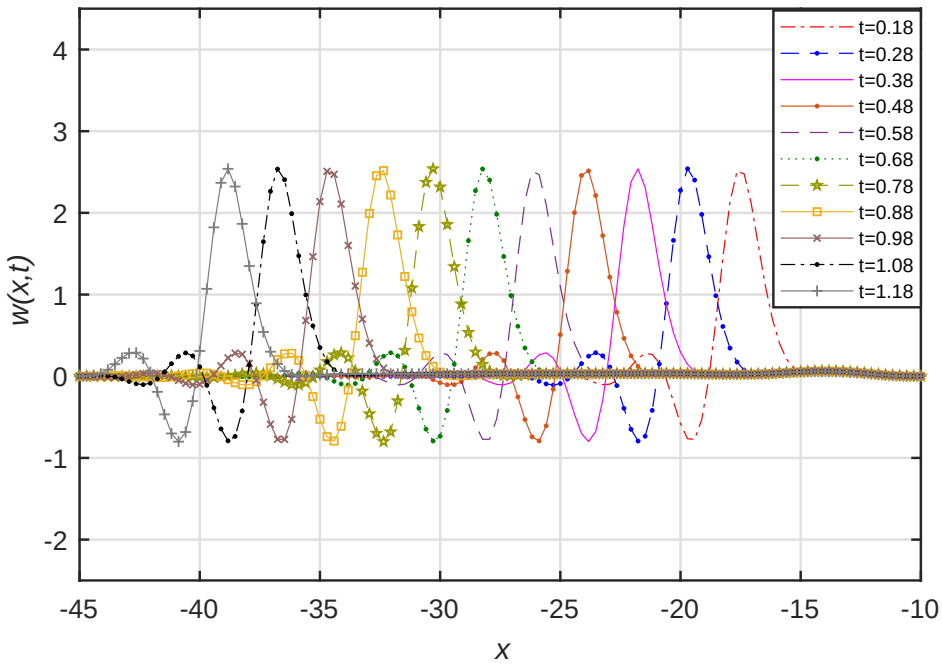

Figure 8.4: The solutions at different moments ($t = 0.18$ to 1.18) for the experiment when $\sigma = 0.1$.

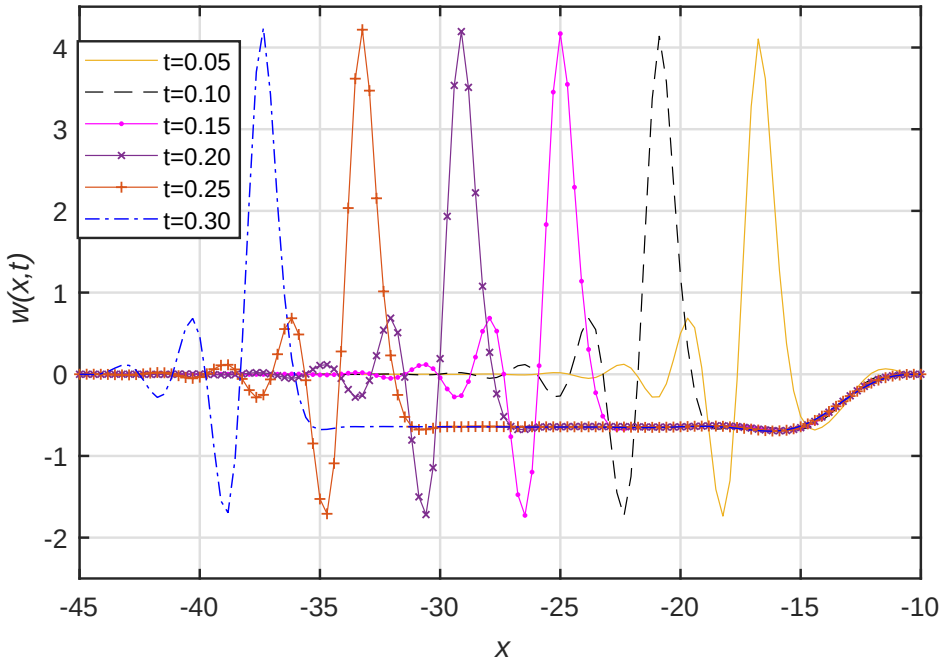

Figure 8.5: The snapshots at different moments ($t = 0.05$ to 0.30) for the experiment when $\sigma = 0.6$.

It is clear from Figs. 8.6 and 8.7 that the amplitude and velocity of the pulse increase with the increasing σ.

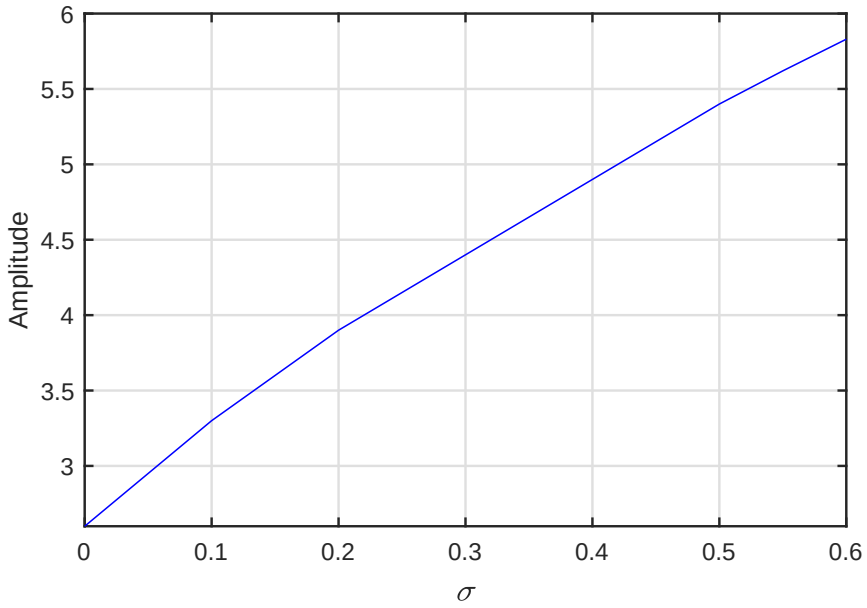

Figure 8.6: The relation between the pulse amplitude and σ.

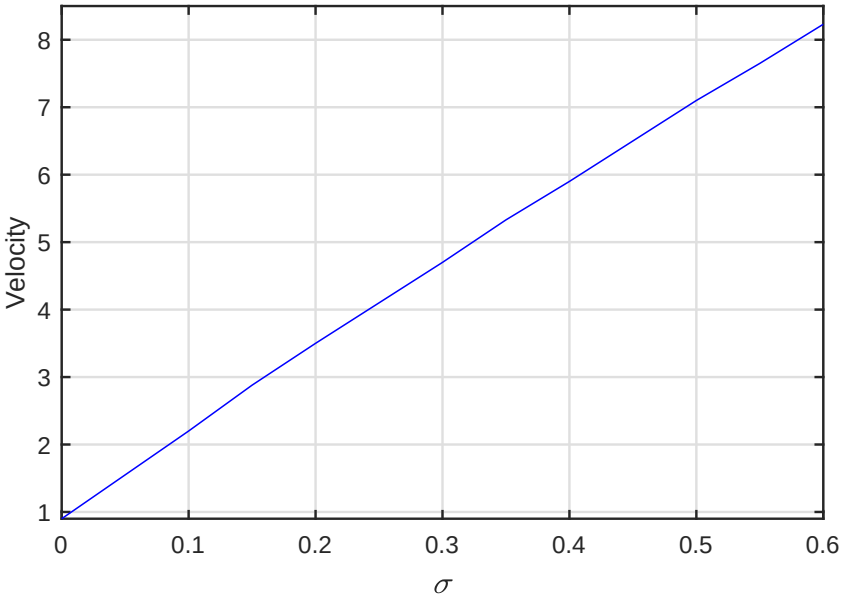

Figure 8.7: The relation between the pulse velocity and σ.

Experiment 2. The channel with local narrowing.

In this experiment, we present the numerical solutions of Eq. (8.1) for the case when the channel has local narrowing modeled by $H_0(x) = H_1 - H_2 \exp[-((x - x_0)/L)^2]$, where the parameter $H_2 > 0$ controls the depth of the narrowing and L controls the width of the narrowing. We set $H_1 = 1$, $H_2 = 0.3$, $L = 7$ and $x_0 = -27$. The number of nodes is 120, and the time step 0.01 .

The initial condition is chosen to be,

$$w(x, 0) = 1.4 \exp[-0.45(x + 12.5)^2] \tag{8.4}$$

see Fig. 8.8 .

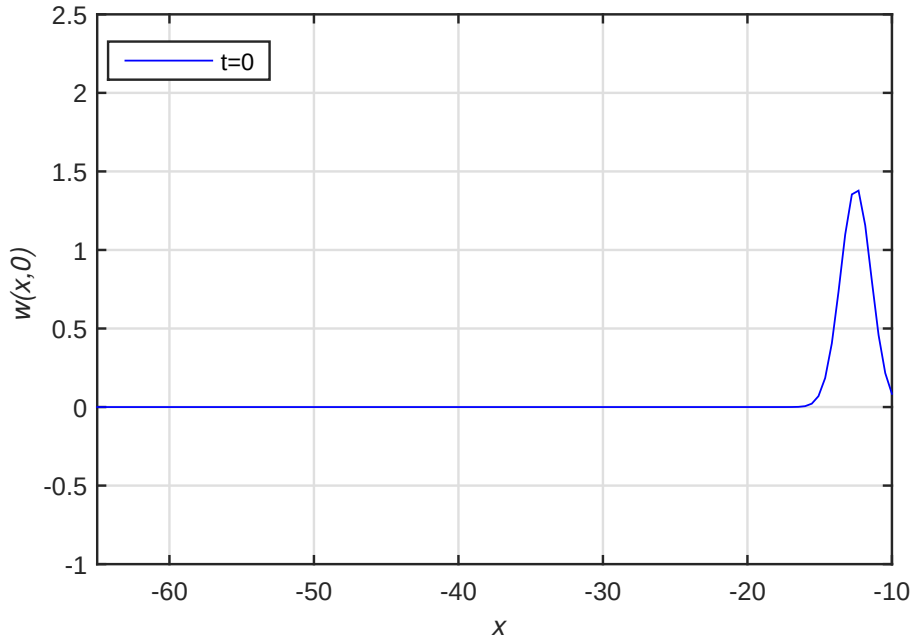

Figure 8.8: The initial condition (8.4) .

Fig. 8.9 shows the evolution of the pulse. Where pulse passes over the narrowing region, the amplitude increases, however after this region the amplitude decreases and then settles at constant level.

Eventually, the pulse decays after hitting the boundary as shown in Fig. 8.10 .

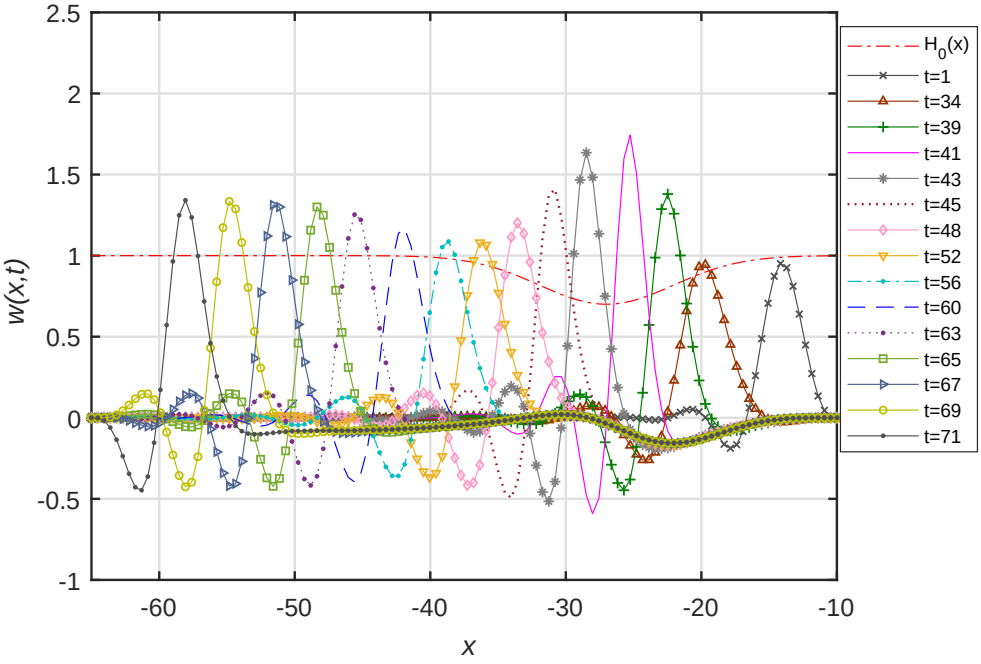

Figure 8.9: The solutions at different moments ($t = 1$ to 71) .

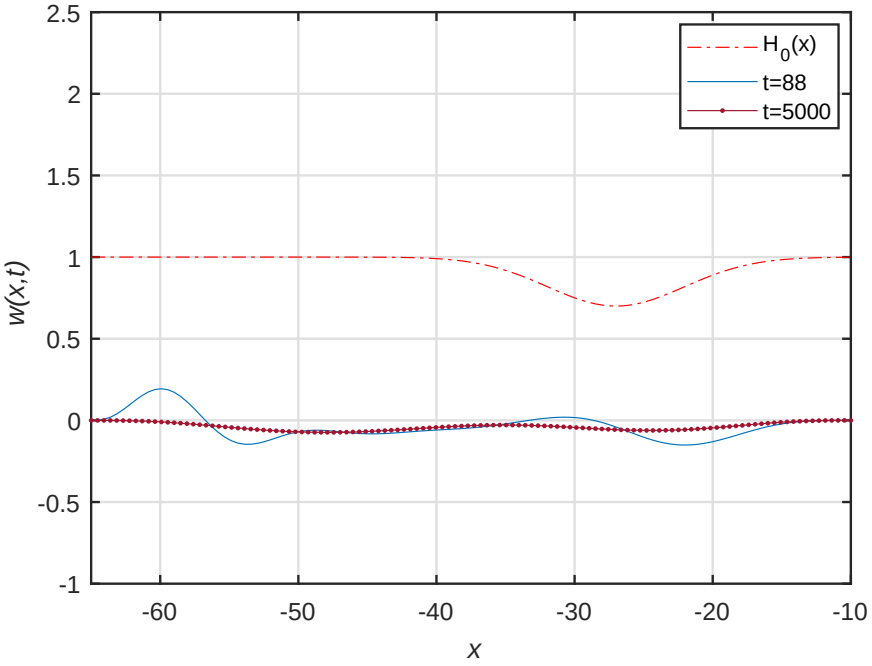

Figure 8.10: Continuation from Fig. 8.9, $t = 88$ and 5000 .

8.3 Conclusion

We presented numerical solutions of the model describing auto-pulses in a single channel with non-constant width simulating an artificial artery with active elastic walls. For the case when the wall has a constant slope, we conducted a series of experiments with zero boundary conditions using the gradually increasing sloping parameter σ. Our code produced the pulse solutions for $0 \leq \sigma \leq 0.6$, before showing numerical instability. We observed that the amplitude and velocity of the pulse increased with the increasing σ. For the case when the channel has local narrowing, the numerical experiment with zero boundary conditions showed that the amplitude of the pulse increased as the pulse was passing through the narrowing region. After this region the amplitude decreased and then settled at constant level until the presence of the boundary was felt.

Chapter 9

Conclusions

9.1 Significance

In this dissertation, we adapted the 1D-IRBFN method presented in (Mai-Duy and Tanner, 2007; Mai-Duy and Tran-Cong, 2001*a*) to solve the model of self-propagating fluid pulses (auto-pulses) through the channel simulating an artificial artery. The model has the form of the 6th-order nonlinear differential equation. Our numerical experiments using the method provided the important knowledge about the dynamics of the auto-pulses, their characteristics and interaction. We anticipate that this knowledge will have practical and theoretical importance in terms of understanding general qualitative properties of the propagating pulses in excitable media, including combustion fronts and reaction-diffusion systems.

9.2 Conclusions

The focus of this thesis is on the the adaptation and application of the numerical code based on the One-dimensional Integrated Radial Basis Function Network (1D-

IRBFN) method to solve the model of self-propagating fluid pulses (auto-pulses) through the channel simulating an artificial artery with *active* elastic walls (Strunin, 2009*a*). The RBFNs have the advantage of using integration instead of traditional differentiation to construct the RBF approximations to improve the stability and accuracy of the numerical solution and to ensure high convergence rate (Mai-Duy and Tran-Cong, 2006). The main results of the application of the method are presented in chapters 3–8.

Chapter 3 demonstrated the accuracy of 1D-IRBFN method in conjunction with the Picard iteration (PI) and one-step Picard iteration (PI1) schemes through two different exact solutions of the Burgers equation. We showed that the present method outperforms the finite difference method with a central difference scheme in conjunction with the forward Euler scheme.

Chapter 4 demonstrated the process of formation of a pulse from an arbitrary initial condition. Subject to spatially periodic boundary conditions, the system generates regimes with one, two or more pulses within one spatial period. We investigated time-dependence of the distance between adjacent pulses in a two-pulse regime and detected small sustained fluctuations. Three-pulse regimes are also explored. The numerical experiments show slight non-uniformity of the average pulse separation and the presence of relatively small fluctuations.

In Chapter 5, the fluid mass flux due to the pulses is calculated. The empirical coefficients α and β of the model responsible for the active motion of the walls are evaluated.

In Chapter 6, the model and the numerical scheme are modified for branching channel. Using homogeneous boundary conditions on the edges of space domain and continuity condition at the branching point, we obtained and analysed solutions in the form of auto-pulses penetrating through the branching point from the thick channel into the thin channels. A series of experiments were conducted using the gradually increasing excitation coefficient α in the thin channel until the pulse "sur-

vived". The numerical results indicated that the thinner the channel the larger the excitation coefficient α needs to be in order to guarantee the pulse "survival".

Chapter 7 presented the derivation of the model with circular cross-section. The chapter also presented the evaluation of the coefficients α and β for the cylindrical model.

Chapter 8 presented the numerical solutions for the channel with pre-existent non-constant width.

In this thesis, we explored the branching configuration with only two branching points as maximum. In the future, it would be interesting to study a system of multiple vessels with three or more branching points.

References

Abraham, R. and Marsden, J. E. (2008), Foundations of mechanics, AMS.

Ahmed, F., Strunin, D., Mohammed, M. and Bhanot, R. (2016), 'Numerical solution for the fluid flow between active elastic walls', *Australian and New Zealand Industrial and Applied Mathematics (ANZIAM) Journal* **57**, C221–C234.

Ahmed, F. Z., Mohammed, M. G., Strunin, D. V. and Ngo-Cong, D. (2018), 'Simulations of autonomous fluid pulses between active elastic walls using the 1d-irbfn method', *Mathematical Modelling of Natural Phenomena* **13**(5), 47.

Alastruey Arimon, J. (2006), Numerical modelling of pulse wave propagation in the cardiovascular system: development, validation and clinical applications, PhD thesis, Imperial College London (University of London).

Alastruey, J., Parker, K. H., Sherwin, S. J. et al. (2012), Arterial pulse wave haemodynamics, *in* '11th International Conference on Pressure Surges', Virtual PiE Led t/a BHR Group: Lisbon, Portugal, pp. 401–442.

Alligood, K. T., Sauer, T. D. and Yorke, J. A. (1997), 'Chaos, textbooks in mathematical sciences'.

Aranson, I. S. and Kramer, L. (2002), 'The world of the complex ginzburg-landau equation', *Reviews of Modern Physics* **74**(1), 99.

Armaou, A. and Christofides, P. D. (2000), 'Feedback control of the kuramoto–sivashinsky equation', *Physica D: Nonlinear Phenomena* **137**(1-2), 49–61.

Arnol'd, V. I. (2013), *Mathematical methods of classical mechanics*, Vol. 60, Springer Science & Business Media.

Avolio, A. (1980), 'Multi-branched model of the human arterial system', *Medical and Biological Engineering and Computing* **18**(6), 709–718.

Balanov, A., Janson, N., Postnov, D. and Sosnovtseva, O. (2008), *Synchronization: from simple to complex*, Springer Science & Business Media.

Beek, P. J., Turvey, M. T. and Schmidt, R. C. (1992), 'Autonomous and nonautonomous dynamics of coordinated rhythmic movements', *Ecological Psychology* **4**(2), 65–95.

Bessonov, N., Sequeira, A., Simakov, S., Vassilevskii, Y. and Volpert, V. (2016), 'Methods of blood flow modelling', *Mathematical modelling of natural phenomena* **11**(1), 1–25.

Bhushan, B. (2000), *Modern tribology handbook, two volume set*, CRC press.

Bowman, C. and Newell, A. (1998), 'Natural patterns and wavelets', *Reviews of Modern Physics* **70**(1), 289.

Causon, D. and Mingham, C. (2010), *Introductory finite difference methods for PDEs*, Bookboon.

Dehghan, M. and Shokri, A. (2007), 'A numerical method for kdv equation using collocation and radial basis functions', *Nonlinear Dynamics* **50**(1-2), 111–120.

Dhawan, S., Kapoor, S., Kumar, S. and Rawat, S. (2012), 'Contemporary review of techniques for the solution of nonlinear burgers equation', *Journal of Computational Science* **3**(5), 405–419.

Ermentrout, G. B. (1981), 'Stable small-amplitude solutions in reaction-diffusion systems', *Quarterly of Applied Mathematics* **39**(1), 61–86.

Fasshauer, G. E. (1997), Solving partial differential equations by collocation with radial basis functions, *in* 'In: Surface Fitting and Multiresolution Methods A. Le M'ehaut'e, C. Rabut and LL Schumaker (eds.), Vanderbilt', Citeseer.

Fedoseyev, A., Friedman, M. and Kansa, E. (2002), 'Improved multiquadric method for elliptic partial differential equations via pde collocation on the boundary', *Computers & Mathematics with Applications* **43**(3-5), 439–455.

Franke, R. (1982), 'Scattered data interpolation: tests of some methods', *Mathematics of computation* **38**(157), 181–200.

Fujisaka, H., Honkawa, T. and Yamada, T. (2003), 'Amplitude equation of higher-dimensional nikolaevskii turbulence', *Progress of theoretical physics* **109**(6), 911–918.

García-Morales, V. and Krischer, K. (2012), 'The complex ginzburg–landau equation: an introduction', *Contemporary Physics* **53**(2), 79–95.

Gorgulu, M. Z., Dag, I. and Irk, D. (2016), Wave propagation by way of exponential b-spline galerkin method, *in* 'Journal of Physics: Conference Series', Vol. 766, IOP Publishing, p. 012031.

Graham, R. and Riste, T. (1975), 'Fluctuations, instabilities and phase transitions', *Springer, Berlin* .

Haff, G. G. and Triplett, N. T. (2015), *Essentials of Strength Training and Conditioning 4th Edition*, Human kinetics.

Haken, H. (1983), Synopsis and introduction, *in* 'Synergetics of the Brain', Springer, Berlin, pp. 3–25.

Haq, S., Bibi, N., Tirmizi, S. I. A. and Usman, M. (2010), 'Meshless method of lines for the numerical solution of generalized kuramoto-sivashinsky equation', *Applied Mathematics and Computation* **217**(6), 2404–2413.

Harkness, G., Firth, W. J., Geddes, J. B., Moloney, J. and Wright, E. (1994), 'Boundary effects in large-aspect-ratio lasers', *Physical Review A* **50**(5), 4310.

Haykin, S. (1999), 'Neural networks, a comprehensive foundation'.

Hidaka, Y., Tamura, K. and Kai, S. (2006), 'Soft-mode turbulence in electroconvection of nematics', *Progress of Theoretical Physics Supplement* **161**, 1–11.

Hirsch, C. (2007), *Numerical computation of internal and external flows: The fundamentals of computational fluid dynamics*, Butterworth-Heinemann.

Ho-Minh, D., Mai-Duy, N. and Tran-Cong, T. (2012), 'Simulation of viscous and viscoelastic flows using a rbf-galerkin approach', *Australian Journal of Mechanical Engineering* **9**(2), 101–112.

Hosseini, B. and Hashemi, R. (2011), 'Solution of burgers equation using a local-rbf meshless method', *International Journal for Computational Methods in Engineering Science and Mechanics* **12**(1), 44–58.

Huang, R. and Suo, Z. (2002), 'Wrinkling of a compressed elastic film on a viscous layer', *Journal of Applied Physics* **91**(3), 1135–1142.

Islam, M. S., Paniconi, C. and Putti, M. (2017), 'Numerical tests of the lookup table method in solving richards equation for infiltration and drainage in heterogeneous soils', *Hydrology* **4**(3), 33.

Jakobsen, P., Moloney, J., Newell, A. and Indik, R. (1992), 'Space-time dynamics of wide-gain-section lasers', *Physical Review A* **45**(11), 8129.

Jameson, A. (1991), 'Time dependent calculations using multigrid, with applications to unsteady flows past airfoils and wings', *AIAA paper* **1596**, 1991.

Kalita, P. (2004), 'Shell models of the artery wall', *Schedae Informaticae* **13**.

Kansa, E. and Hon, Y. (2000), 'Circumventing the ill-conditioning problem with multiquadric radial basis functions: applications to elliptic partial differential equations', *Computers & Mathematics with applications* **39**(7-8), 123–137.

Kansa, E. J. (1990*a*), 'Multiquadricsa scattered data approximation scheme with applications to computational fluid-dynamicsi surface approximations and partial derivative estimates', *Computers & Mathematics with applications* **19**(8-9), 127–145.

Kansa, E. J. (1990*b*), 'Multiquadricsa scattered data approximation scheme with applications to computational fluid-dynamicsii solutions to parabolic, hyperbolic and elliptic partial differential equations', *Computers & mathematics with applications* **19**(8), 147–161.

Katok, A. and Hasselblatt, B. (1997), *Introduction to the modern theory of dynamical systems*, Vol. 54, Cambridge university press.

Kleinstreuer, C. (2006), *Biofluid dynamics: Principles and selected applications*, CRC Press.

Kolodner, P. (1991), 'Drift, shape, and intrinsic destabilization of pulses of traveling-wave convection', *Physical Review A* **44**(10), 6448.

Kolodner, P., Bensimon, D. and Surko, C. (1988), 'Traveling-wave convection in an annulus', *Physical Review Letters* **60**(17), 1723.

Ku, D. N. (1997), 'Blood flow in arteries', *Annual review of fluid mechanics* **29**(1), 399–434.

Kudryashov, N. (1990), 'Exact solutions of the generalized kuramoto-sivashinsky equation', *Physics Letters A* **147**(5-6), 287–291.

Kuramoto, Y. (1984*a*), 'Chemical oscillations, waves, and turbulence', *Springer Series in Synergetics* **19**.

Kuramoto, Y. (1984*b*), 'Phase dynamics of weakly unstable periodic structures', *Progress of theoretical physics* **71**(6), 1182–1196.

Kuramoto, Y. and Tsuzuki, T. (1976), 'Persistent propagation of concentration waves in dissipative media far from thermal equilibrium', *Progress of theoretical physics* **55**(2), 356–369.

Lakshmanan, M. and Rajaseekar, S. (2012), *Nonlinear dynamics: integrability, chaos and patterns*, Springer Science & Business Media.

Lam, L. (2003), *Introduction to nonlinear physics*, Springer Science & Business Media.

Landa, P. S. (2013), *Nonlinear oscillations and waves in dynamical systems*, Vol. 360, Springer Science & Business Media.

Landau, L. D. and Lifshitz, E. M. (1959), *Course of Theoretical Physics Vol 7: Theory and Elasticity*, Pergamon Press.

Larsson, E. and Fornberg, B. (2003), 'A numerical study of some radial basis function based solution methods for elliptic pdes', *Computers & Mathematics with Applications* **46**(5), 891–902.

Layek, G. (2015), *An Introduction to Dynamical Systems and Chaos*, Springer.

Lehmann, E. D. (1999), 'Clinical value of aortic pulse-wave velocity measurement', *The Lancet* **354**(9178), 528–529.

Li, S., Vogt, D. M., Rus, D. and Wood, R. J. (2017), 'Fluid-driven origami-inspired artificial muscles', *Proceedings of the National Academy of Sciences* p. 201713450.

London, G. M. and Pannier, B. (2010), 'Arterial functions: how to interpret the complex physiology.', *Nephrology Dialysis Transplantation* **25**(12).

Madych, W. and Nelson, S. (1992), 'Bounds on multivariate polynomials and exponential error estimates for multiquadric interpolation', *Journal of Approximation Theory* **70**(1), 94–114.

Mai-Duy, N. and Tanner, R. (2007), 'A collocation method based on one-dimensional rbf interpolation scheme for solving pdes', *International Journal of Numerical Methods for Heat & Fluid Flow* **17**(2), 165–186.

Mai-Duy, N. and Tran-Cong, T. (2001*a*), 'Numerical solution of differential equations using multiquadric radial basis function networks', *Neural Networks* **14**(2), 185–199.

Mai-Duy, N. and Tran-Cong, T. (2001*b*), 'Numerical solution of navier–stokes equations using multiquadric radial basis function networks', *International journal for numerical methods in fluids* **37**(1), 65–86.

Mai-Duy, N. and Tran-Cong, T. (2003), 'Approximation of function and its derivatives using radial basis function networks', *Applied Mathematical Modelling* **27**(3), 197–220.

Mai-Duy, N. and Tran-Cong, T. (2006), 'Solving biharmonic problems with scattered-point discretization using indirect radial-basis-function networks', *Engineering Analysis with Boundary Elements* **30**(2), 77–87.

Manneville, P. (1990), 'Dissipative structures and weak turbulence', *San Diego, CA, Academic Press, Inc., 1990, 500 p.* .

Matthys, K. S., Alastruey, J., Peiró, J., Khir, A. W., Segers, P., Verdonck, P. R., Parker, K. H. and Sherwin, S. J. (2007), 'Pulse wave propagation in a model

human arterial network: assessment of 1-d numerical simulations against in vitro measurements', *Journal of biomechanics* **40**(15), 3476–3486.

Mohammed, F., Ngo-Cong, D., Strunin, D., Mai-Duy, N. and Tran-Cong, T. (2014), 'Modelling dispersion in laminar and turbulent flows in an open channel based on centre manifolds using 1d-irbfn method', *Applied Mathematical Modelling* **38**(14), 3672–3691.

Mukherjee, N. and Poria, S. (2012), 'Preliminary concepts of dynamical systems', *International Journal of Applied Mathematical Research* **1**(4), 751–770.

Nakayama, Y. (2018), *Introduction to fluid mechanics*, Butterworth-Heinemann.

Newell, A. C. and Whitehead, J. A. (1969), 'Finite bandwidth, finite amplitude convection', *Journal of Fluid Mechanics* **38**(2), 279–303.

Ngo-Cong, D., Mai-Duy, N., Karunasena, W. and Tran-Cong, T. (2011), 'Free vibration analysis of laminated composite plates based on fsdt using one-dimensional irbfn method', *Computers & structures* **89**(1), 1–13.

Ngo-Cong, D., Mai-Duy, N., Karunasena, W. and Tran-Cong, T. (2012*a*), 'Local moving least square-one-dimensional integrated radial basis function networks technique for incompressible viscous flows', *International Journal for Numerical Methods in Fluids* **70**(11), 1443–1474.

Ngo-Cong, D., Mai-Duy, N., Karunasena, W. and Tran-Cong, T. (2012*b*), 'A numerical procedure based on 1d-irbfn and local mls-1d-irbfn methods for fluid-structure interaction analysis', *CMES: Computer Modeling in Engineering and Sciences* **83**(5), 459–498.

Ngo-Cong, D., Mohammed, F., Strunin, D., Skvortsov, A., Mai-Duy, N. and Tran-Cong, T. (2015), 'Higher-order approximation of contaminant transport equation

for turbulent channel flows based on centre manifolds and its numerical solution', *Journal of Hydrology* **525**, 87–101.

Olufsen, M. S., Peskin, C. S., Kim, W. Y., Pedersen, E. M., Nadim, A. and Larsen, J. (2000), 'Numerical simulation and experimental validation of blood flow in arteries with structured-tree outflow conditions', *Annals of biomedical engineering* **28**(11), 1281–1299.

Ott, E. (2002), *Chaos in dynamical systems*, Cambridge university press.

Paniconi, C. and Putti, M. (1994), 'A comparison of picard and newton iteration in the numerical solution of multidimensional variably saturated flow problems', *Water Resources Research* **30**(12), 3357–3374.

Power, H. and Barraco, V. (2002), 'A comparison analysis between unsymmetric and symmetric radial basis function collocation methods for the numerical solution of partial differential equations', *Computers & Mathematics with Applications* **43**(3-5), 551–583.

Quarteroni, A. M. and Valli, A. (2008), 'Numerical approximation of partial differential equations'.

Quarteroni, A., Tuveri, M. and Veneziani, A. (2000), 'Computational vascular fluid dynamics: problems, models and methods', *Computing and Visualization in Science* **2**(4), 163–197.

Quarteroni, A., Veneziani, A. and Zunino, P. (2002), 'Mathematical and numerical modeling of solute dynamics in blood flow and arterial walls', *SIAM Journal on Numerical Analysis* **39**(5), 1488–1511.

Rabinovich, M. I., Ezersky, A. B. and Weidman, P. D. (2000), *The dynamics of patterns*, World Scientific.

Roberts, A. J. (1994), *A one-dimensional introduction to continuum mechanics*, World Scientific.

Robertson, A. M., Sequeira, A. and Kameneva, M. V. (2008), Hemorheology, *in* 'Hemodynamical flows', Springer, pp. 63–120.

Robertson, A. M., Sequeira, A. and Owens, R. G. (2009), Rheological models for blood, *in* 'Cardiovascular mathematics', Springer, pp. 211–241.

Saarloos, W. v., Cladis, P., Palffy-Muhoray, P. et al. (1994), 'The complex ginzburg-landau equation for beginners'.

Šarler, B., Perko, J. and Chen, C.-S. (2004), 'Radial basis function collocation method solution of natural convection in porous media', *International Journal of Numerical Methods for Heat & Fluid Flow* **14**(2), 187–212.

Sarra, S. A. (2006), 'Integrated multiquadric radial basis function approximation methods', *Computers & Mathematics with Applications* **51**(8), 1283–1296.

Sherwin, S., Formaggia, L., Peiro, J. and Franke, V. (2003), 'Computational modelling of 1d blood flow with variable mechanical properties and its application to the simulation of wave propagation in the human arterial system', *International Journal for Numerical Methods in Fluids* **43**(6-7), 673–700.

Sivashinsky, G. (1977), 'Nonlinear analysis of hydrodynamic instability in laminar flames—i. derivation of basic equations', *Acta Astronautica* **4**, 1177–1206.

Stewartson, K. and Stuart, J. (1971), 'A non-linear instability theory for a wave system in plane poiseuille flow', *Journal of Fluid Mechanics* **48**(3), 529–545.

Strogatz, S. H. (2014), *Nonlinear dynamics and chaos: with applications to physics, biology, chemistry, and engineering*, Hachette UK.

Strunin, D. (1999), 'Autosoliton model of the spinning fronts of reaction', *IMA journal of applied mathematics* **63**(2), 163–177.

Strunin, D. (2003), 'Nonlinear instability in generalized nonlinear phase diffusion equation', *Progress of Theoretical Physics Supplement* **150**, 444–448.

Strunin, D. (2009*a*), 'Fluid flow between active elastic plates', *ANZIAM Journal* **50**, 871–883.

Strunin, D. (2009*b*), 'Phase equation with nonlinear excitation for nonlocally coupled oscillators', *Physica D: Nonlinear Phenomena* **238**(18), 1909–1916.

Strunin, D. and Ahmed, F. (2019), 'Parameters and branching auto-pulses in a fluid channel with active walls', *Fluids* **4**(3), 160.

Strunin, D. and Mohammed, M. (2015), 'Range of validity and intermittent dynamics of the phase of oscillators with nonlinear self-excitation', *Communications in Nonlinear Science and Numerical Simulation* **29**(1), 128–147.

Surovtsova, I. (2005), 'Effects of compliance mismatch on blood flow in an artery with endovascular prosthesis', *Journal of biomechanics* **38**(10), 2078–2086.

Szeri, A. Z. (2010), *Fluid film lubrication*, Cambridge university press.

Tanaka, D. (2005), 'Critical exponents of nikolaevskii turbulence', *Physical Review E* **71**(2), 025203.

Tanaka, D. and Kuramoto, Y. (2003), 'Complex ginzburg-landau equation with nonlocal coupling', *Physical Review E* **68**(2), 026219.

Tien, C., Thai-Quang, N., Mai-Duy, N., Tran, C. and Tran-Cong, T. (2015*a*), 'High-order fully coupled scheme based on compact integrated rbf approximation for viscous flows in regular and irregular domains', *CMES: Computer Modeling in Engineering and Sciences* **105**(4), 301–340.

Tien, C., Thai-Quang, N., Mai-Duy, N., Tran, C. and Tran-Cong, T. (2015*b*), 'A three-point coupled compact integrated rbf scheme for second-order differential

problems', *CMES: Computer Modeling in Engineering and Sciences* **104**(6), 425–469.

Timoshenko, S. P. and Woinowsky-Krieger, S. (1987), *Theory of plates and shells*, McGraw-hill.

Tran, C.-D., Mai-Duy, N., Le-Cao, K. and Tran-Cong, T. (2012), 'A continuum-microscopic method based on irbfs and control volume scheme for viscoelastic fluid flows', *CMES: Computer Modeling in Engineering and Sciences* **85**(6), 499–519.

Uddin, M., Haq, S. et al. (2009), 'A mesh-free numerical method for solution of the family of kuramoto–sivashinsky equations', *Applied Mathematics and Computation* **212**(2), 458–469.

Vlachopoulos, C., O'Rourke, M. and Nichols, W. W. (2011), *McDonald's blood flow in arteries: theoretical, experimental and clinical principles*, CRC press.

Walgraef, D. (2012), *Spatio-temporal pattern formation: with examples from physics, chemistry, and materials science*, Springer Science and Business Media.

Xu, M., Wang, R.-H., Zhang, J.-H. and Fang, Q. (2011), 'A novel numerical scheme for solving burgers equation', *Applied mathematics and computation* **217**(9), 4473–4482.

Zerroukat, M., Power, H. and Chen, C. (1998), 'A numerical method for heat transfer problems using collocation and radial basis functions', *International Journal for Numerical Methods in Engineering* **42**(7), 1263–1278.

Zhang, X., Kinnick, R. R., Fatemi, M. and Greenleaf, J. F. (2005), 'Noninvasive method for estimation of complex elastic modulus of arterial vessels', *IEEE transactions on ultrasonics, ferroelectrics, and frequency control* **52**(4), 642–652.

Appendix A

Second-order integrated radial basis function networks

Second-order 1D-IRBFN (1D-IRBFN-2) presented by (Mai-Duy and Tanner, 2007) are briefly described here. In this appendix, we use the following notations: $\widehat{[\,]}$ for a vector/matrix $[\,]$ that is associated with a grid line, and $[\,]_{(n)}$ to denote selected components of the vector $[\,]$. Along an x-grid line (see Fig. A.1), the variation of the function u is represented in the IRBF form.

Figure A.1: 1-D grid line with N number of nodes.

For the solving second-order differential equations (DEs), we first starts from the decomposition of second-order derivative of u into RBFs; the expressions for the first-order derivative of u and the function u itself are then obtained through the

integration of RBF network

$$\frac{\partial^2 u(x)}{\partial x^2} = \sum_{i=1}^{N} w_i G_i(x) = \sum_{i=1}^{N} w_i H_2^{(i)}(x)\,, \tag{A.1}$$

$$\frac{\partial u(x)}{\partial x} = \sum_{i=1}^{N} w_i H_1^{(i)}(x) + c_1\,, \tag{A.2}$$

$$u(x) = \sum_{i=1}^{N} w_i H_0^{(i)}(x) + c_1 x + c_2\,, \tag{A.3}$$

where N represents the number of nodes on the x-grid line; $\{w_i\}_{i=1}^{N}$ represent RBF weights to be determined; $\{G_i(x)\}_{i=1}^{N} = \{H_2^{(i)}(x)\}_{i=1}^{N}$ represent RBFs, and for the case of multiquadrics (MQ) is defined as $G_i(x) = \sqrt{(x-c_i)^2 + {a_i}^2}$, where c_i and a_i are the centre and width of the i^{th} MQ-RBF, respectively. The set of centres is taken to be the same as the set of collocation points. The RBF width is defined as $a_i = bd_i$, $b > 0$ is a factor (presently $b = 1$), and d_i is the distance between the i-th centre and its closest grid point; $H_1^{(i)}(x) = \int H_2^{(i)}(x)dx$; $H_0^{(i)}(x) = \int H_1^{(i)}(x)dx$; and c_1 and c_2 are the constants of integration which are also unknown. The new basis functions $H_1^{(i)}(x)$ and $H_0^{(i)}(x)$ are obtained through the integration of MQ,

$$H_1^{(i)}(x) = \frac{r}{2}\sqrt{r^2 + {a_i}^2} + \frac{{a_i}^2}{2}\ln\left|r + \sqrt{r^2 + {a_i}^2}\right|\,,$$
$$H_0^{(i)}(x) = \left(\frac{r^2}{6} - \frac{{a_i}^2}{3}\right)\sqrt{r^2 + {a_i}^2} + \frac{{a_i}^2 r}{2}\ln\left|r + \sqrt{r^2 + {a_i}^2}\right|\,,$$

where $r = x - c_i$. Re-writing Eq. (A.3) in a compact form as

$$\hat{u} = \hat{H}\hat{\alpha}\,, \quad \hat{\alpha} = [\hat{w}\hat{c}]^T \tag{A.4}$$

in which $\widehat{H}$ represents an $N \times (N+2)$ matrix and defined by

$$\widehat{H} = \begin{bmatrix} H_0^{(1)}(x_1) & H_0^{(2)}(x_1) & \cdots & H_0^{(N)}(x_1) & x_1 & 1 \\ H_0^{(1)}(x_2) & H_0^{(2)}(x_2) & \cdots & H_0^{(N)}(x_2) & x_2 & 1 \\ \vdots & \vdots & \ddots & \vdots & \vdots & \vdots \\ H_0^{(1)}(x_N) & H_0^{(2)}(x_N) & \cdots & H_0^{(N)}(x_N) & x_N & 1 \end{bmatrix}, \tag{A.5}$$

where$\{x_i\}_{i=1}^{N}$ is the set of nodal points, $\widehat{u} = (u_1, u_2, u_3, ..., u_N)^T$, $\widehat{w} = (w_1, w_2, w_3, ..., w_N)^T$ and $\widehat{c} = (c_1, c_2)^T$. We denote $\widehat{\alpha} = (w_1, w_2, w_3, ..., w_N, c_1, c_2)^T$.

Appendix B

Solving ordinary differential equation (ODE) using 1D-IRBFN method

Example

Consider the following ordinary differential equation

$$\frac{d^2u}{dx^2} = -16\pi^2 \sin(4\pi x)\,, \tag{B.1}$$

on the interval $0 \leq x \leq 1$. The exact solution of (B.1) has the following form

$$u_e(x) = 2 + \sin(4\pi x)\,. \tag{B.2}$$

The Dirichlet boundary conditions are $u = 2$ at $x = 0$ and $x = 1$. Fig. B.1 shows an excellent agreement between the exact solution and 1D-IRBFN results using a grid of 100.

Table B.1 and Fig. B.2 describe the relative error norms (Ne(u)) for the 1D-IRBFN method and finite difference (FD) method with a central difference scheme.

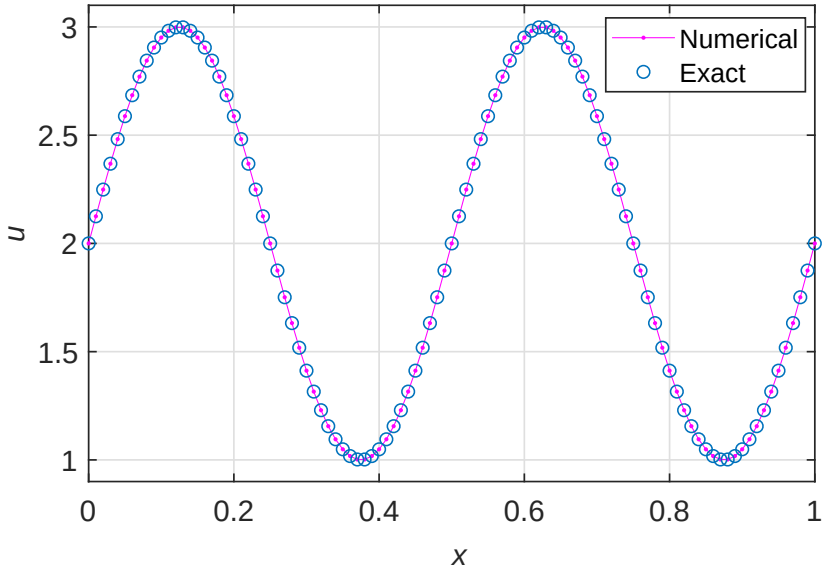

Figure B.1: Comparison between the exact solution (B.2) and 1D-IRBFN result using a grid of 100 .

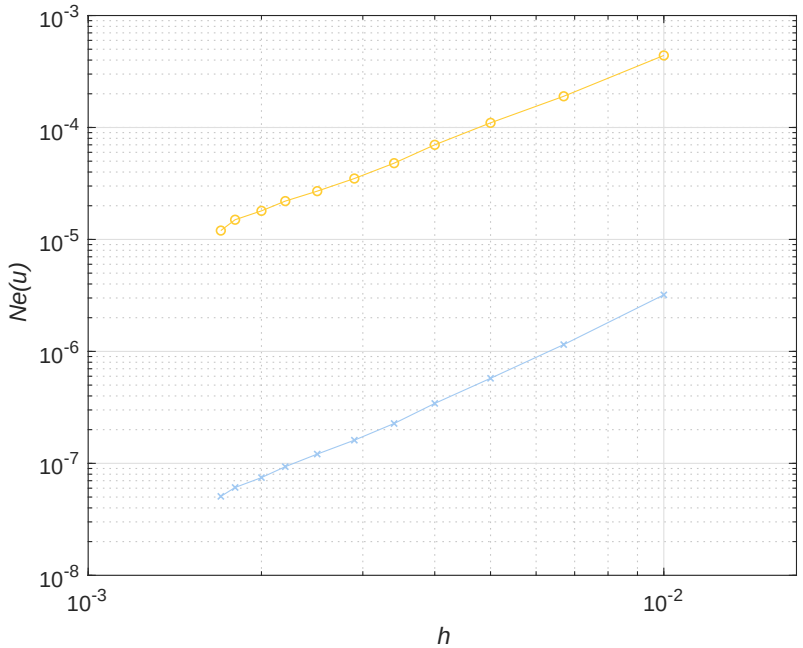

Figure B.2: Convergence study for the 1D-IRBFN and FDM (central difference) of Eq. (B.1) .

The error norms are slightly reduced with the increasing in the grid number. The convergence behaviour of the FDM and 1D-IRBFN are $O(h^{2.00})$ and $O(h^{2.30})$ respectively. Numerical results show that the 1D-IRBFN method is much more accurate than the FDM and converges faster. At a grid of 601, the error norm (Ne(u)) is 5.07×10^{-8} for the 1D-IRBFN and 1.22×10^{-5} for the FDM.

Table B.1: Comparison of relative error norm (Ne(u)) between two methods for several numbers of grids and h is the grid size (distance between consecutive grid nodes).

Grid	h	Ne(u)	
		1D-IRBFN	FDM
101	0.0100	3.20E-06	4.37E-04
151	0.0067	1.15E-06	1.94E-04
201	0.0050	5.75E-07	1.10E-04
251	0.0040	3.43E-07	7.00E-05
301	0.0034	2.27E-07	4.87E-05
351	0.0029	1.61E-07	3.58E-05
401	0.0025	1.21E-07	2.74E-05
451	0.0022	9.34E-08	2.16E-05
501	0.0020	7.46E-08	1.75E-05
551	0.0018	6.09E-08	1.45E-05
601	0.0017	5.07E-08	1.22E-05

Appendix C

Finite difference method

Finite difference method (FDM) is perhaps one of the simplest and the most commonly method for solving differential equations (DEs) numerically (Hirsch, 2007), in which the discretisation of spatial derivatives is derived using the Taylor series expansion. Taylors theorem states (Causon and Mingham, 2010): Let a function $g(x) : R \to R$ be n times differentiable over the interval $I = (a, b)$. For $a < x_0$, $x_0 + h < b$, the function evaluated at $x = x_0 + h$ has a value

$$g(x_0+h) = g(x_0)+\frac{h}{1!}g'(x_0)+\frac{h^2}{2!}g''(x_0)+\frac{h^3}{3!}g'''(x_0)+\cdots+\frac{h^n}{n!}g^n(x_0)+O(h^n)\,, \quad \text{(C.1)}$$

where $g^n(x_0)$ is the nth derivative of g with respect to x evaluated at $x = x_0$ and $O(h^n)$ represents the local truncation error which is proportional to h^n. By solving the equation (C.1) for the first derivative, we get the first order forward-difference scheme

$$g'(x_0) = \frac{g(x_0 + h) - g(x_0)}{h} + O(h) \approx \frac{g(x_0 + h) - g(x_0)}{h}\,, \quad \text{(C.2)}$$

in which the derivative of g at the point x_0 is approximated by the value at the grid point x_0 and the forward grid point $x_0 + h$ as illustrated in Fig. C.1. The first-order backward-difference scheme is derived using the information at x_0 and $x_0 - h$ to

approximate the derivative of g as follows:

$$g'(x_0) = \frac{g(x_0) - g(x_0 - h)}{h} + O(h) \approx \frac{g(x_0) - g(x_0 - h)}{h}\,. \tag{C.3}$$

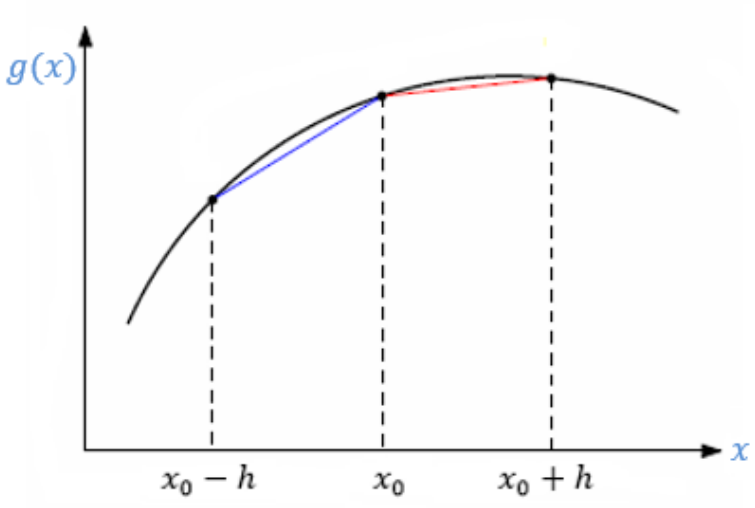

Figure C.1: The derivatives of g at x_0 can be approximated at the forward or backward grid point.

By adding the above forward and backward difference schemes one can obtain the second order difference scheme

$$g'(x_0) = \frac{g(x_0 + h) - g(x_0 - h)}{2h} + O(h^2) \approx \frac{g(x_0 + h) - g(x_0 - h)}{2h}\,. \tag{C.4}$$

This formula (C.4) is called the central difference scheme which is more accurate than either the forward or backward formulas.

By using the Taylor series expansion we can also derive the central difference formula for second derivatives as follows:

$$g(x_0 + h) = g(x_0) + \frac{h}{1!}g'(x_0) + \frac{h^2}{2!}g''(x_0) + \frac{h^3}{3!}g'''(x_0) + O(h^4)\,. \tag{C.5}$$

Similarly, by replacing h by $-h$,

$$g(x_0 - h) = g(x_0) - \frac{h}{1!}g'(x_0) + \frac{h^2}{2!}g''(x_0) - \frac{h^3}{3!}g'''(x_0) + O(h^4)\,. \tag{C.6}$$

Adding these two equations gives us

$$g(x_0 + h) + g(x_0 - h) = 2g(x_0) + h^2 g''(x_0) + O(h^4) \tag{C.7}$$

or

$$g''(x_0) = \frac{g(x_0 + h) - 2g(x_0) + g(x_0 - h)}{h^2} + O(h^2)\,, \tag{C.8}$$

which is second-order accurate.

Appendix D

Example

We apply formula (5.3) to an approximate step-like configuration of the pulse as shown in Fig. D.1. We have

$$\frac{\lambda}{H_0^2\beta}\int_L Q\,dt = -\int_L w^6\,dx + \frac{1}{L}\left(\int_L w^5\,dx\right)\cdot\left(\int_L w\,dx\right)$$

$$= -w_0^6\delta - w_1^6(L-\delta) + \frac{1}{L}\left[w_0^5\delta - w_1^5\,(L-\delta)\right]\cdot\left[w_0\delta - w_1\,(L-\delta)\right]$$

$$= \frac{\delta\,(L-\delta)}{L}\left[-w_0^6 - w_1^6 - w_0^5 w_1 - w_0 w_1^5\right] < 0$$

for any $w_0 > 0$, $w_1 > 0$ and $L > \delta$.

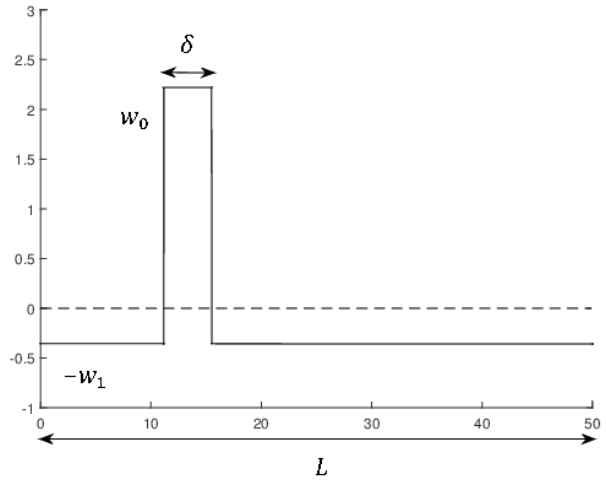

Figure D.1: A primitive configuration of the pulse.